

ATTENUATION CORRECTION IN POSITRON TOMOGRAPHY

by:

SIU KI YU, M.Sc., B.Sc.

A Thesis

Submitted to the School of Graduate Studies

in Partial Fulfilment of the Requirements

for the Degree

Doctor of Philosophy

McMaster University

© Copyright by Siu Ki Yu, 1996

DOCTOR OF PHILOSOPHY (1996) McMASTER UNIVERSITY
(Medical Physics) Hamilton, Ontario

TITLE: Attenuation Correction in Positron Tomography

AUTHOR: Siu Ki Yu, M.Sc., B.Sc. (McMaster University)

SUPERVISOR: Dr. C. Nahmias

NUMBER OF PAGES: xv, 131

ATTENUATION CORRECTION IN POSITRON TOMOGRAPHY

ABSTRACT

Accurate attenuation correction is a prerequisite for the determination of precise regional radioactivity concentrations in positron tomography. Attenuation correction can be performed using an external source of radiation and two measurements: a blank scan performed with no subject in the tomograph, and a transmission scan performed with the subject in the field of view. The ratio of blank to transmission counts gives the appropriate attenuation correction factor for each line of response. In theory, this provides a perfect correction for photon attenuation, but in practice the technique is limited by noise due to limited counting statistics and scattered radiation in the measured transmission data.

In the present work, ^{137}Cs is proposed as a suitable radiation source for transmission measurements in 'singles' mode, a technique that substantially increases the statistical accuracy of the transmission data. ^{137}Cs can be used without any recalibration of the tomograph, and the spatial resolution is comparable to that obtained using ^{68}Ge . Since ^{137}Cs emits a monoenergetic gamma ray at 662 keV, and emission data are acquired by detecting annihilation photons of energy 511 keV, a simple extrapolation method is developed to extrapolate the attenuation coefficients measured at 662 keV to 511 keV. To eliminate scatter contamination in the transmission data, a dual-energy-window scatter correction technique is developed whereby correction can be made on-the-fly during data acquisition. Using the developed extrapolation method and dual energy scatter correction method, the linear attenuation coefficients measured in 'singles' mode using ^{137}Cs agree well with the expected values.

To achieve further suppression of noise in the transmission data, a segmented attenuation correction technique is also developed in this work. The technique uses artificial neural networks for processing the count-limited transmission data. The technique has been validated in phantoms and verified in human studies. The results indicate that attenuation coefficients measured in the segmented transmission images are accurate and reproducible. Activity concentrations measured in the reconstructed emission image can also be recovered accurately with this technique. The accuracy of the technique is subject independent and insensitive to scatter contamination in the transmission data. It can predict accurately the value of the attenuation coefficient for any material in the range from air to water. Satisfactory results are obtained if the transmission data contains as few as 400,000 true counts per plane. Thus, accurate attenuation data can be obtained by acquiring a short transmission scan using the 'singles' method, and then processing these data using the artificial neural network technique.

ACKNOWLEDGEMENTS

I would like to express my gratitude to my supervisor, Claude Nahmias, for his invaluable guidance and support along the way. I am very thankful for the assistance from all my friends in the department of Nuclear Medicine. Thanks also to my committee: Dr. Colin Webber, and Dr. Douglas Wyman for their helpful suggestions. Particular thanks are extended to Dr. Colin Webber for allowing me to use his famous blocks of wood.

To my family and my girl friend (Chor-Yi), thank you for the support and encouragement.



TABLE OF CONTENTS

	Page
ABSTRACT	iii
ACKNOWLEDGEMENTS	v
TABLE OF CONTENTS	vii
LIST OF TABLES	xi
LIST OF FIGURES	xiii
INTRODUCTION	1
CHAPTER 1. POSITRON TOMOGRAPHY	3
1.1 PHYSICAL PRINCIPLES OF PET	4
1.2 IMAGE FORMATION	8
1.2.1 PET Scanner	8
1.2.2 Sinogram	10
1.2.3 Normalization	12
1.3 LIMITATION OF QUANTITATION IN PET	12
1.3.1 Spatial Resolution	12
1.3.2 Random and Multiple Coincidences	14
1.3.3 Attenuation	15
1.3.4 Scatter	17
REFERENCES	20
CHAPTER 2. ATTENUATION CORRECTION TECHNIQUES	23
2.1 CALCULATED ATTENUATION CORRECTION	24
2.1.1 Geometric Outline	24
2.1.2 Fitted Outline	25

2.2	MEASURED ATTENUATION CORRECTION	27
2.2.1	Noise Reduction Techniques for Measured Attenuation Correction	29
2.2.1.1	sinogram smoothing	29
2.2.1.2	random sinogram processing	29
2.2.1.3	reconstruction-reprojection	30
2.2.1.4	sinogram windowing	30
2.2.1.5	single photon transmission measurement	31
2.2.1.6	scatter correction for transmission measurement ...	32
2.3	HYBRID ATTENUATION CORRECTION	33
2.3.1	Discrete Segmentation Method	34
2.3.2	Continuous Segmentation Method	37
	REFERENCES	38

CHAPTER 3. SINGLE-PHOTON TRANSMISSION

	MEASUREMENTS USING ^{137}Cs	43
3.1	INTRODUCTION	44
3.2	SUITABLE RADIOISOTOPES FOR SINGLE- TRANSMISSION MEASUREMENTS IN PET	45
3.3	^{137}Cs AS A TRANSMISSION SOURCE IN PET	47
3.4	EXTRAPOLATION OF ATTENUATION CORRECTION FACTORS	51
3.5	SCATTER CORRECTION OF THE TRANSMISSION DATA	56
3.6	DISCUSSION	58
	REFERENCES	60

CHAPTER 4. SEGMENTED ATTENUATION CORRECTION USING ARTIFICIAL NEURAL NETWORKS IN PET	63
4.1 INTRODUCTION	64
4.2 TRANSMISSION MEASUREMENTS	65
4.3 ARTIFICIAL NEURAL NETWORK (ANN)	66
4.4 MAPPING OUTPUTS FROM ANN TO NEW ATTENUATION COEFFICIENT	72
4.5 VERIFICATION OF THE CALIBRATION	75
4.6 VERIFICATION OF THE ANN TECHNIQUE	76
4.6.1 Counting Statistics Requirement and Subject Dependence of the ANN Technique	76
4.6.2 Reproducibility of the ANN Technique	79
4.6.3 Recovery of Activity Concentration in Emission Measurements	80
4.6.4 Human Studies	81
4.7 DISCUSSION	84
REFERENCES	87
 CHAPTER 5. CONCLUSION AND FUTURE WORK	 91
5.1 CONCLUSION	91
5.2 FUTURE WORK	92
5.2.1 Application of the ANN Technique for Attenuation Correction in PET/CT System	98
5.2.2 Application of the ANN Technique for Assaying Heterogeneous Radioactive Wastes	98
5.2.3 Evaluation of the Diagnostic Performance of the ANN Technique	99

REFERENCES 99

GLOSSARY 101

APPENDIX A HUMAN STUDIES 105

APPENDIX B PROGRAM LISTING 113

LIST OF TABLES

Table		Page
1.1	Properties of commonly used radioisotopes in PET (from Bacharach <i>et al</i> 1992, Lederer <i>et al</i> 1968).	4
3.1	List of monoenergetic gamma ray emitters with $T_{1/2} > 30$ days. gamma ray energies from 400 keV to 700 keV (from Lederer <i>et al</i> 1968).	46
3.2	The ratio of mean light output from an irradiated row(r) or column (c) to that of the adjacent unirradiated rows or columns in an eight detector block.	48
3.3	Linear attenuation coefficients measured using ^{68}Ge and ^{137}Cs in single mode without interplane septa.	54
3.4	Linear attenuation coefficients measured using ^{68}Ge and ^{137}Cs in single mode without interplane septa after scatter correction.	58
4.1	Weight fractions, density and the theoretical attenuation coefficients of 4 different kinds of wood (from Webber 1981).	73
4.2	Attenuation coefficients obtained from the ANN technique with and without scatter correction of the transmission data.	76
4.3	Variation of segmented attenuation coefficient between and within subjects.	77
4.4	Average segmented attenuation coefficients over 8 trials and their standard deviation between trials. Theoretical attenuation coefficients are also given for comparison to the average segmented μ .	79
4.5	Recovered activity concentrations in emission measurement for no, measured and segmented attenuation correction with 10 and 60 million measured counts in transmission measurement compared to the actual activity concentrations in each insert.	81

5.1	Theoretical linear attenuation coefficient and segmented linear attenuation coefficient of the inserts	94
A.1	The required net trues in plane #20 for 5 minute and 25 minute transmission scans for each patient.	105

LIST OF FIGURES

Figure		Page
1.1(a)	A block of 8x8 BGO detectors coupled to 4 PMTs.	8
1.1(b)	Two buckets mounted side by side, each bucket contains 4 blocks of detectors.	8
1.1(c)	ECAT 953/31 scanner has 16 arrays of BGO detectors encircling the field of view. Each ring of detector blocks contains 12 buckets of detectors.	9
1.2	The interplane septa and the lead collimators are used to attenuate non-transaxial coincident events.	9
1.3	Line of response definition.	11
1.4	2D acquisition and 3D acquisition.	11
1.5	All possible sampling of LOR in a circular PET system. The system on the right side has detectors with half of the size of those in the system on the left.	13
1.6	Random coincidence occurs when a pair of uncorrelated photons strikes the detectors within the timing coincidence window.	14
1.7	Annihilation photons must travel through a distance a to reach detector 1 and distance b to reach detector 2.	17
1.8	Scatter event occurs when one or both photons are Compton scattered and strike the detectors within a timing coincidence window.	18
2.1	Transmission images and their pixel intensity histograms acquired in (a) practical scan time, (b) long scan time.	36
3.1	Light output from an 8x8 block of detectors. A row (r1..r4) or a column (c1..c4) was irradiated by a point source of either $^{68}\text{Ge}/^{68}\text{Ga}$ (Ge) or ^{137}Cs (Cs) collimated using two parallel lead blocks.	49



3.2	Light distribution in an 8x8 block of detectors. An uncollimated point source of either $^{68}\text{Ge}/^{68}\text{Ga}$ (Ge) (left) or ^{137}Cs (Cs) (right) was positioned 62 cm away from the detectors.	50
3.3	Ratio of mass attenuation coefficient of biological tissues to water.	52
3.4	Energy of photons after scattering through a given angle.	55
3.5	Relative differential scattering probability as a function of scattering angle.	55
3.6	Transmission images of a 21 cm water cylinder containing a 2.5 cm aluminum insert and a 5 cm air insert without scatter correction (a) and after scatter correction (b).	60
4.1	The basic structure of the ANN. The PCA has 49 inputs (x_0 to x_{48}) and 5 outputs (y_0 to y_4). The MLP has two hidden layers, one with 8 nodes ($h1_0$ to $h1_7$), the other with 4 nodes ($h2_0$ to $h2_3$). The outputs of the MLP ($y1$, $y2$ and $y3$) are the conditional probabilities that the central input pixel (x_{24}) belongs to the class 'air', 'lung' or 'soft tissue'.	67
4.2	The rate of learning of the MLP portion of the ANN during the training process.	70
4.3	Plot of $P(\text{soft tissue} \mathbf{x})$ against $P(\text{air} \mathbf{x})$.	73
4.4	Calibration curve for mapping $P(\text{soft tissue} \mathbf{x})$ to attenuation coefficients.	74
4.5	Correlation constant as a function of true counts in the transmission images, each image is correlated with the one containing most counts.	78
4.6	Average absolute error as a function of true counts in the transmission images.	78
4.7	The segmented attenuation coefficients for 8 trials of transmission measurements of a phantom containing hexane, acetone and water.	80

4.8	Results of a study in a patient with a history of ischaemic heart disease. The first row shows the transmission images (25 min., segmented 5 min., and segmented 25 min. from the left). The second and third rows show the ^{18}F FDG and ^{13}N -ammonia images respectively, reconstructed with the corresponding attenuation data in the first row.	83
4.9	Block diagram for obtaining accurate ACFs using 'singles' measurements and ANN.	86
5.1	An artificially generated CT image is used for training the ANN.	94
5.2	The top left curve shows the mapping from CT number to attenuation coefficients. The top right curve indicates that the conditional probabilities of a pixel being soft tissue ($P(\text{st} x)$) and aluminium ($P(\text{al} x)$) are a one-to-one function if $P(\text{al} x)$ is larger than 0.2. Therefore, the calibration curve on the bottom right which converts $P(\text{al} x)$ to attenuation coefficients is used when $P(\text{al} x)$ is larger than 0.2, otherwise, the calibration curve on the bottom left which converts $P(\text{st} x)$ to attenuation coefficients is used.	95
5.3	The original CT images (left) and the segmented CT images (right).	96
5.4	The CT image (left) and segmented image (right) after reduction of matrix size from 512x512 to 128x128. The images are smoothed with a 9x9 Gaussian filter to obtain a spatial resolution of 6 mm.	97



INTRODUCTION

Positron tomography (PET) has been in development for several decades. During this evolution, the primary objective has been the improvement of the accuracy with which radioactivity distributions can be measured in subjects who have been administered specific molecules labeled with positron emitters. The accuracy with which activity per unit volume can be measured in vivo will influence the quantitative interpretation of images, and the quantitative assessment of metabolic processes. This accuracy is limited by statistical uncertainties in the measured emission data and the need to account for the absorption and scattering of the annihilation photons in the subjects.

A unique property of PET is the ability to perform accurate attenuation correction of the emission data. In cardiac PET studies, because of the heterogeneous structure of the chest, attenuation correction is generally performed by means of transmission measurements. However, the success of the technique is limited by the noise due to limited counting statistics and scattered radiation in the measured transmission data. The problem of noise in the emission image can only be compounded when modified for attenuation correction by noisy transmission data.

The development of a new technique for measuring transmission data that relies on the detection of photons in 'singles' mode rather than 'coincidence' mode no longer restricts the choice of transmission sources to those that decay by positron emission. The incentive for using the 'singles' mode of operation is the substantial increase in statistical accuracy of the transmission data that can be achieved. With the development in this work of a simple method for extrapolating attenuation coefficients measured at one energy to those which would have been obtained at another, ^{137}Cs is proposed as a suitable radiation source for the transmission measurements in 'singles' mode. A dual-

energy-window scatter correction technique is also developed to allow scatter correction to be made on-the-fly during data acquisition.

Although the scatter contamination in the transmission data can be corrected for by scatter correction techniques, the statistical noise in the transmission data will be increased by this additional measurement. In this work, a technique is developed that uses artificial neural networks (ANN) for processing count-limited transmission data. The ANN technique requires short transmission scan times, and is capable of providing accurate, subject independent and reproducible attenuation data without the need for scatter correction. It is shown to predict accurately the value of the attenuation coefficient for any material in the range from air to water. Thus, accurate attenuation data can be obtained by acquiring a short transmission scan in 'singles' mode, and then processing these data using the ANN technique.

A description of the principles of PET is presented in chapter 1. This is followed, in chapter 2, by a review of the attenuation correction methods in PET and the relevant techniques for improving the accuracy of the methods. Chapter 3 discusses the feasibility of using ^{137}Cs as the radiation source for transmission measurements in 'singles' mode. A description of the development and validation of the ANN method is presented in chapter 4. Chapter 5 contains the conclusion of this work and suggestions for future work.

CHAPTER 1

POSITRON TOMOGRAPHY

Positron tomography (PET) is a technique for studying metabolic processes in vivo. The technique combines principles of image reconstruction from projections and the use of specific molecules labeled with positron emitters. The radioisotopes commonly used, such as ^{11}C , ^{13}N , ^{15}O , are natural constituents of organic molecules, and can be generated in particle accelerators such as cyclotrons. The detection in coincidence of the pair of photons resulting from the annihilation of a positron with an electron forms the basis of the measurement. Reconstructed data represent the distribution of isotope concentration in cross sections of the patient.

From the regional distribution and the time course of the isotope concentration, decisions can be made about the state of health and disease of the organ under study. The accuracy of the PET measurements are affected by factors such as attenuation, scatter, and random coincidences. Hence, the inaccuracies, or lack of adequate corrections, for those factors limit the accuracy of the physiologic information to be extracted from the measurements. In this chapter, the essential physical principles of PET are reviewed, the PET scanner used in this work is described, and the limitations of quantitation in PET measurements are discussed.

1.1 PHYSICAL PRINCIPLES OF PET

Proton-rich nuclides have two means of transformation into stable nuclides: (a) positron emission, or (b) electron capture. In both cases, a neutrino is also emitted. Electron capture is more prevalent for heavy nuclei because the large nuclear charge draws the orbital electrons closer to the nucleus. For light elements, such as those mostly used in PET studies, positron emission is the predominant process (table 1.1).

Table 1.1 : Properties of commonly used radioisotopes in PET (from Bacharach 1992, Lederer 1968).

Isotopes	Percent β^+ Decay (%)	Half-Life	Max Energy (MeV)	Mean Energy (MeV)	Mean β^+ Range in soft-tissue (mm)
^{18}F	97	109 min	0.635	0.250	0.35
^{11}C	99	20.3 min	0.96	0.386	0.56
^{13}N	100	10.0 min	1.19	0.492	0.72
^{15}O	100	124 sec	1.72	0.735	1.1
^{68}Ga	88	68.3 min	1.90	0.836	1.1
^{82}Rb	96	75 sec	3.15	1.52	2.4

The emitted positron slows down as it loses energy through interactions with the surrounding matter. The average distance traveled by the positron varies with its initial kinetic energy and the density of the surrounding medium (table 1.1). When the kinetic energy of the positron reaches thermal levels (less than 10 eV), it can interact with an electron in a process in which the rest masses of the electron and the positron are converted to energy in the form of two 511 keV photons. Conservation of momentum dictates that the two photons must travel in opposite direction, exactly 180° apart; however, the photons can be emitted a few tenths of a degree more or less than 180° due to the residual momentum of the two particles (Evans 1982).

In a PET emission study, a set of coincidence measurements of the annihilation photons is taken at different locations at different angles around the object. Using this measured data, an emission image is reconstructed that represents the spatial distribution of the activity concentration of the positron emitting isotopes within the object. Due to the effect of positron range (table 1), the emission image will be blurred, and the effect is more pronounced for isotopes that emit positrons with high kinetic energy such as ^{82}Rb . As the resolution of positron scanners improves, the resolution limits imposed by the positron range are becoming a significant fraction of the overall systematic error associated with PET emission measurements.

The other errors are due to the interactions of the annihilation photons within the object, and to the recording of random coincidences. The annihilation photons will interact predominantly through photoelectric and Compton interactions. Both these effects will contribute to the attenuation of the flux of photons as it traverses the object. For 511 keV photons, the probability of photoelectric absorption varies with the atomic number (Z) of the element as $Z^{3.5}$, and with the photon energy (E) as E^{-3} (Evans 1982); whereas that of Compton scattering varies as Z (Knoll 1989). Thus, 511 keV photons in soft tissue will predominantly be scattered.

The scattering process results in a photon of lower energy, traveling at an angle θ with respect to the original path. The energy of the scattered photon is governed by the following equation.

$$E' = \frac{E}{1 + \frac{E}{m_0 c^2} (1 - \cos \theta)} \quad (1.1)$$

where E' = photon energy after scattering

E = original photon energy

$m_0 c^2$ = rest mass energy of an electron (0.511 MeV)

The angular distribution of scattered photons is predicted by the Klein-Nishina equation (Knoll 1989) for the differential scattering cross section $\partial\sigma_c/\partial\Omega$:

$$\frac{\partial\sigma_c}{\partial\Omega} = r_o^2 \left(\frac{1}{1 + \alpha(1 - \cos\theta)} \right)^2 \left(\frac{1 + \cos^2\theta}{2} \right) \left(1 + \frac{\alpha^2(1 - \cos\theta)^2}{(1 + \cos^2\theta)[1 + \alpha(1 - \cos\theta)]} \right) \quad (1.2)$$

where $r_o = 2.828$ fm is the classical electron radius and $\alpha = E/m_o c^2$. For 511 keV annihilation photons, $\alpha = 1$ and equations (1.1) and (1.2) reduce to :

$$E' = \frac{E}{2 - \cos\theta} \quad (1.3)$$

$$\frac{\partial\sigma_c}{\partial\Omega} = r_o^2 \left(\frac{3 - 3\cos\theta + 3\cos^2\theta - \cos^3\theta}{2(2 - \cos\theta)^3} \right) \quad (1.4)$$

With the understanding of the unique property of positron decay that the annihilation of the positron with an electron will result in the emission of two 511 keV photons at the same instant in time and traveling at 180° to each other, it becomes obvious that coincidence detection of these photons by detectors on opposite sides of an object places the site of the annihilation on the line joining the two detectors, named the line of response (LOR). In other words, the LOR defines a column in space within which the annihilation photons originated, containing the location of the decaying isotope. This 'electronic' collimation is quite unlike that required by other nuclear imaging techniques which use lead collimators to block the emissions in a particular direction with respect to the face of the radiation detector.

In practice, any two photons that are detected within a coincidence timing window, τ_c (typically 10-15 ns), are considered as occurring simultaneously (Knoll 1989). At the present time, the most commonly used photon detector is bismuth germanate

(BGO: $\text{Bi}_4\text{Ge}_3\text{O}_{12}$), a scintillation crystal optically coupled to a photomultiplier tube (PMT). The probability that an incident gamma ray will be absorbed in the crystal is high, because the high atomic number (83) of the bismuth leads to high photoelectric cross section. Thus, a signal is generated which ideally represents the full energy of the gamma ray. Pulse height analysis can then be used to select photopeak events and reject low energy scattered photons. However, the scintillation efficiency, i.e. the ratio of light output to incident photon energy, is low (about 8 % of NaI(Tl)) (Knoll 1989). Of the light photons produced, only about 20-30 % will actually be converted into electrons at the photocathode of the PMT (Knoll 1989). Therefore, the statistical fluctuations in the height of the pulse coming from the PMT are high. This limits the scintillation detector's energy resolution (i.e. the accuracy of resolving photon energy). The energy resolution for BGO is approximately 25 % at 511 keV. For a BGO detector, photons are recorded in practice within an energy window, 350-650 keV, centered about 511 keV. Despite the poor energy resolution of the BGO detector, the timing resolution is fair. The decay time of a light flash for BGO has a half-life of 300 ns, compared to 230 ns for NaI(Tl), but the afterglow due to phosphorescence is much smaller than that for NaI(Tl) (Knoll 1989). At high counting rates, the phosphorescence will tend to build up due to multiple overlaps from many preceding pulses. This afterglow is an undesirable characteristic of NaI(Tl) in high counting rate applications.

In order to perform a PET measurement, the scanner must be capable of recording the time of arrival and energy of the annihilation photons as well as the detector pair involved. As position information is derived from the location of the detectors, spatial resolution is determined predominantly by the material and sensitivity of the detector, and its dimensions. To obtain high spatial resolution, the dimensions of the detectors must be minimized while a high probability of interaction in the detector material must be maintained.

1.2 IMAGE FORMATION

The aim of PET imaging is to estimate the distribution of positron labeled molecules, in space and time, within a region of the object. Assuming the distribution does not change for the period of time during which a frame of data is collected, the measured data thus describes quantitatively the spatial and temporal distribution of the positron labeled molecules in the region. Transverse tomographic images are reconstructed from a series of measurements taken at different angles around the object under study. The mathematical algorithms used to recover the distribution are similar to those developed for X-ray computed tomography (Gelfand and Thomas 1988).

1.2.1 PET Scanner

The PET scanner used in this study was the SIEMENS/CTI ECAT 953/31 at McMaster University. The scanner consists of 16 rings of BGO detectors. Each BGO crystal has dimensions 6.22 mm (transaxial width) x 6.75 mm (axial length) x 30 mm (radial depth). A matrix of 8 x 8 crystals forms a detector block which is coupled to 4 PMTs as illustrated in figure 1.1(a). Identification of the detector element in which the interaction occurred is calculated from the ratios of the PMT outputs. As shown in figure 1.1(b), four adjacent blocks share a common electronics unit to form a bucket and there are 12 buckets per ring (figure 1.1(c)).

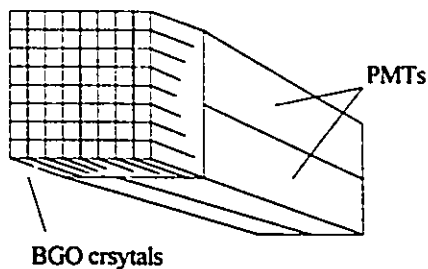


Figure 1.1(a) A block of 8 x 8 BGO detectors coupled to 4 PMTs.

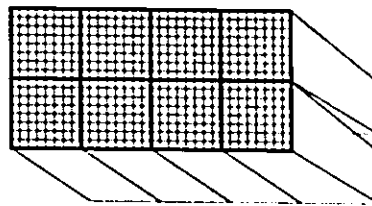


Figure 1.1(b) Two buckets mounted side by side, each bucket contains 4 blocks of detectors.

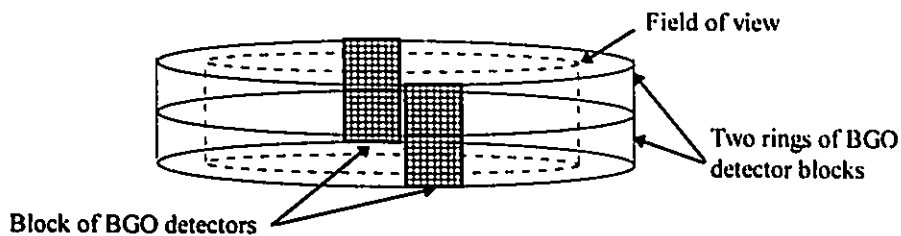


Figure 1.1(c) ECAT scanner has 16 arrays of BGO detectors encircling the field of view. Each ring of detector blocks contains 12 buckets of detectors.

The 16 crystal detector rings are collimated by interplane septa, annuli of tungsten, 1 mm (axial thickness) x 7.7 cm (radial thickness), that are spaced and positioned to align with the tiny gaps between the rings of detectors. They are mounted together with the spacing between each annulus of tungsten maintained in an expanded polystyrene structure surrounded by carbon fiber. As illustrated in figure 1.2, detectors are also shielded from radioactivity beyond the axial field of view of the tomograph by two thick lead annuli.

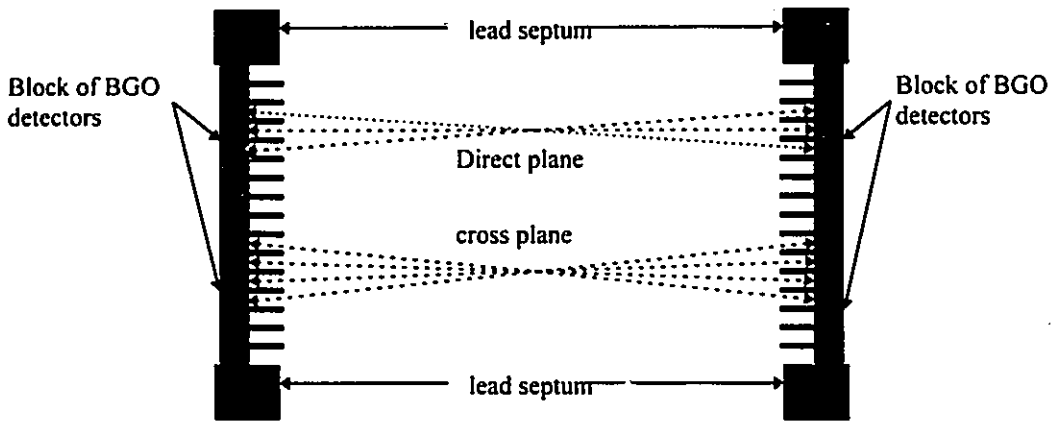


Figure 1.2 The interplane septa and the lead collimators are used to attenuate non-transaxial coincident events.

1.2.2 Sinogram

In the ECAT 953/31 scanner, each detector is allowed to form a LOR with the 160 opposing detectors across the field of view (FOV). Each LOR formed records the activity in the region of space subtended by the two detectors, and its location can be described by the radial distance (r) from the center of the FOV and the angle of the LOR (θ) as shown in figure 1.3. Since there are 384 BGO detectors in a ring, 192 projection angles are possible. The projection data are stored in a 160×192 matrix in which each element corresponds to a particular $p(r,\theta)$. This matrix is called a sinogram. During acquisition, valid coincidence signals from the detectors are passed from the image plane coincidence processors to the real time sorter (RTS), the special purpose hardware which sorts, in real time, the LOR into their correct location in the appropriate sinogram.

It is always advantageous to detect as many photons as possible because this increase the sensitivity of the scanner. In general, any detector in a ring can be in

coincidence with another detector in any other ring. In 2D mode, the coincidences are restricted to those detectors within the same ring (ring difference of zero) or rings that are offset by one position (ring difference of 2). These are called direct planes. For cross plane, the coincidences are restricted to those detectors that are in adjacent rings (ring difference of 1), or rings that are offset by two positions (ring difference of 3). Hence, a set of 31 sinograms (16 direct, 15 cross planes) are generated to record the coincidence events in the object being imaged. This mode of operation minimizes random and out of plane scatter coincidences, but also restricts the sensitivity of the tomograph as many valid coincidences are not considered since annihilation photons are emitted isotropically.

Therefore the scanner was modified to allow 3D imaging by removing the interplane septa (Dahlbom *et al* 1989), although the ECAT 953/31 was designed originally for 2D imaging. This allows true coincidence LORs between pairs of detectors more than two rings apart to be measured. During a three-dimensional acquisition (3D mode), coincidence events may occur between detectors in any of the 16 detector rings as shown in figure 1.4. Hence, a total of 256 sinograms are required to record all the projection data in 3D. This is achieved by a straightforward reconfiguration of the RTS memory in order to map the additional LOR into the correct memory location.

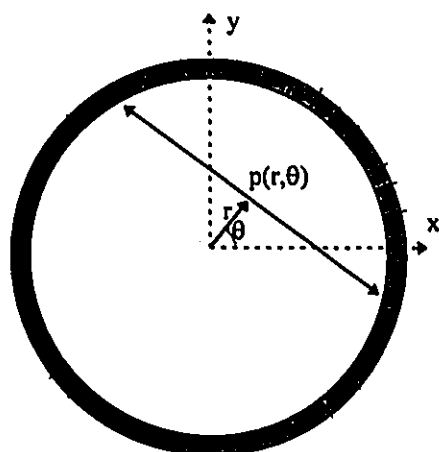


Figure 1.3 Line of response definition.

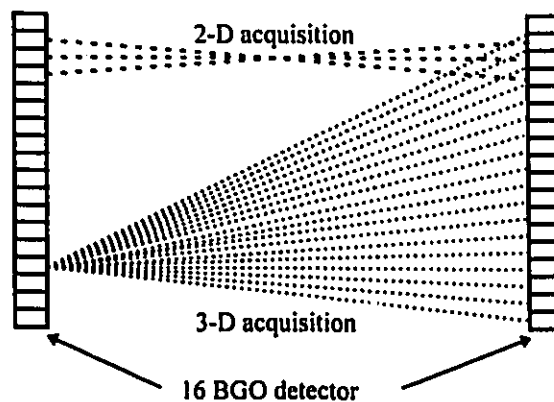


Figure 1.4 2D acquisition and 3D acquisition.

1.2.3 Normalization

Since the sensitivity of each detector will differ, it is necessary to equalize the relative efficiencies for all detector pairs to give, within measurement error, a uniform response to a uniform source. Therefore, the accuracy and precision of the measured data rely on the accuracy of the normalization procedure. The usual procedure is to perform a scan using a rotating plane source to measure the sensitivity of each detector pair. Taking into account the source and scanner geometry, the normalization factors can then be calculated for each LOR and stored into normalization sinograms. These normalization sinograms are then applied during image reconstruction, and they provide scaling factors to weight the LORs being processed into the image. Software is provided with the ECAT 953/31 scanner for the routine determination of the normalization factors.

1.3 LIMITATION OF QUANTITATION IN PET

1.3.1 Spatial Resolution

Ideally, the value in each pixel of a reconstructed PET image is proportional to the concentration of positron emitter at that location in the object. In practice, as in all measurements, there are a number of sources of error in the technique.

One source of error is the spatial resolution of the PET scanner. Poor resolution can affect results of a PET measurement by: (a) failing to resolve two closely lying structures and incorrectly placing activity from one structure in the region of the other, (b) reducing the apparent isotope concentration in structures that are smaller than about twice the spatial resolution of the scanner (Hoffman *et al* 1979), and (c) causing an

overestimation in the size of structures smaller than about twice the spatial resolution of the PET scanner (Hoffman *et al* 1979), all causing difficulty in the interpretation of the reconstructed images.

One of the physical limits of the spatial resolution in PET systems is the size of the BGO detectors. The transaxial width of the detectors influences the in-plane resolution, while the axial length affects the resolution in the axial direction. Other factors, such as the noncollinearity of the annihilation photons, or the positron range, also affect the spatial resolution (Phelps *et al* 1986).

The counting statistics in PET measurement are generally limited and the measured data are normally smoothed for noise reduction. However, this filtering operation also degrades the resolution in the reconstructed image. As illustrated in figure 1.5, the poor spatial sampling from systems with large detectors results in poor spatial resolution in the reconstructed images. With the introduction of BGO material, it is possible to make the detectors small enough to perform adequate sampling; however, the counting statistics for each LOR is also reduced. Thus, there is always a trade-off between spatial resolution and counting statistics.

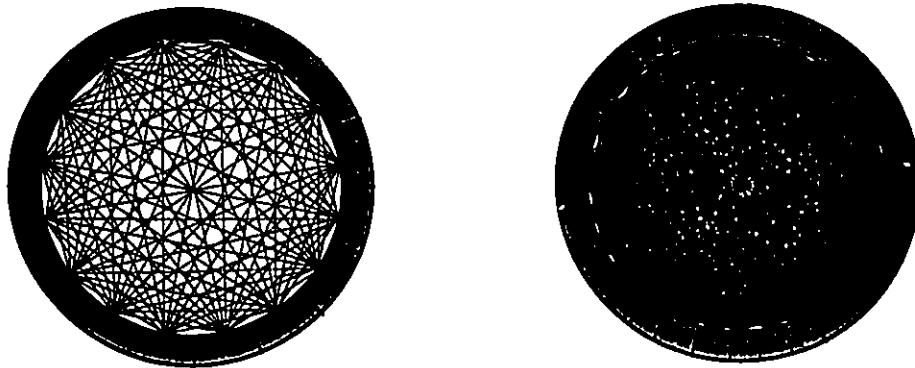


Figure 1.5 All possible sampling of LOR in a circular PET system. The system on the right side has detectors with half of the size of those in the system on the left.

1.3.2 Random and Multiple Coincidences

Random and multiple coincidences are two sources of noise in PET. As illustrated in figure 1.6, a false datum will be registered as a coincidence count when a pair of photons originating from two separate annihilation events are detected within τ_c . These coincidences are called random coincidences (RC). Random coincidences affect PET measurements by either overestimating the measured activity for each LOR when RC are not subtracted from the scan data, or by increasing the statistical noise through propagation of statistical errors in their measurement and subtraction from the total coincidence data (Hoffman *et al* 1981).

The random rate can be estimated theoretically from the product of the singles count rates in each detector in a pair multiplied by τ_c . Since the singles count rate is much higher than the total coincidence rate, the precision of this method is good in terms of statistical accuracy. However, accurate methods for dead time correction for both single event rates and coincidence events rates must be determined before this method can be used.

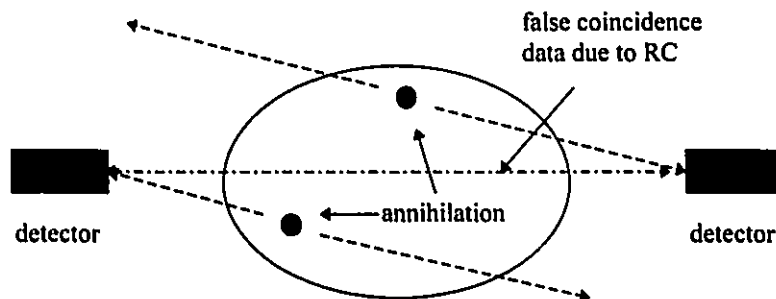


Figure 1.6 Random coincidence occurs when a pair of uncorrelated photons strikes the detectors within the timing coincidence window.

where D is the total distance, $a+b$, through the body; and μ is the attenuation coefficient of the medium.

The number of measured true emission events (m_p) along the LOR joining the two detectors can be represented by the product of the true emission events with no attenuation (n_p) and the probability of transmission (P_{12}), as expressed in the following equation.

$$m_p = n_p * P_{12} \quad (1.6)$$

Thus, the attenuation correction factor (ACF) is just the inverse of P_{12} .

In water, the attenuation coefficient has a theoretical value 0.0957 cm^{-1} for 511 keV photons. Since soft tissue is mainly composed of water, more than 85% of the photons will be attenuated as they pass through a body with a thickness of 20 cm soft-tissue according to equation (1.5). Obviously, attenuation can have a significant effect on the quantitation of PET data. Unlike single photon emission computed tomography (SPECT) in which attenuation factors will vary depending on the depth at which the isotope is located in tissue, attenuation factors in PET depend only upon the attenuation through the total body thickness between the two detectors. Different approaches to attenuation correction techniques have been developed, and they will be described in chapter 2.

The ECAT 953/31 scanner uses another technique called the delayed coincidence method. The delayed coincidence method is based on the principle that the random coincidence event rate detected in a delayed time window is approximately equal to that in the coincidence time window. Since the random coincidences are measured with the same circuitry as the total coincidence events, except for the time delay, random coincidences are subject to the same dead time losses. Thus, RC measured using this method should be a good estimate of the real RC in the total coincidence data. The major problem of this method is the statistical noise in the measurement.

Multiple coincidences occur when more than two photons are detected within τ_c . This can be caused by either a true coincidence event and a single photon or three independent single photons. Whatever the causes, the LOR cannot be determined and the data must be discarded resulting in losses of true events.

1.3.3 Attenuation

When annihilation photons travel through an object, many will undergo Compton scattering and/or photoelectric interaction in the object. The loss of coincidence events due to these interactions is termed attenuation. For 511 keV photons traveling through soft-tissue, most of the interactions are Compton scatter events. Even in bone, photoelectric interactions are not likely.

In order for a coincidence event to be detected, both annihilation photons must reach their respective detectors. As illustrated in figure 1.7, photon 1 and 2 must travel respectively through a thickness of tissue a and b without interaction. The probability that both photons will exit the object is then

$$P_{12} = e^{-\mu a} \times e^{-\mu b} = e^{-\mu(a+b)} = e^{-\mu D} \quad (1.5)$$

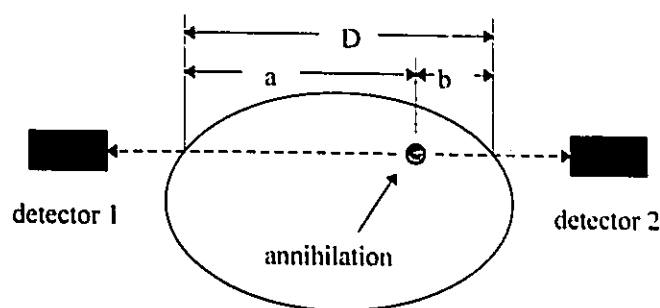


Figure 1.7 Annihilation photons must travel through a distance a to reach detector 1 and a distance b to reach detector 2.

1.3.4 Scatter

As mentioned in the last section, Compton scattering is the predominant interaction in the attenuation process. When one or both photons in a coincidence event are Compton scattered in the body, the resultant LOR will convey false position information as shown in figure 1.8. These events contribute noise, which in turn results in loss of image contrast and produces quantitative inaccuracies.

Two basic techniques can be used to reduce the scatter effect in the reconstructed image. One is to suppress the scatter events in the acquired data. Since the scattered photons are at lower energy than their original energy, the normal setting of the energy window (i.e. 350-650 keV) will exclude some of the scatter events. According to equation (1.3), photons scattered at an angle less than 57° still have energies greater than 350 keV, and thus may fall within the energy window. The proportion of scattered events excluded can be raised if the lower discrimination level of the energy window is set to a higher value (Koral *et al* 1986). A method (Dahlbom *et al* 1987) originally designed to reduce random noise by raising the energy discrimination threshold, will also reduce scattered photons simultaneously. However, the energy resolution of BGO detectors is relatively

poor and most of the scattered photons are forward scattered without losing much of their original energy. Therefore, the technique is not adequate to reject all of the scattered events without significantly reducing the number of true events detected. Another means of scatter suppression is improving the shielding geometry of the detectors with narrow planes and long septa as proposed by Thompson (1988). This stops cross-plane scattered events effectively, but cannot have any effect on the in-plane scattered photons.

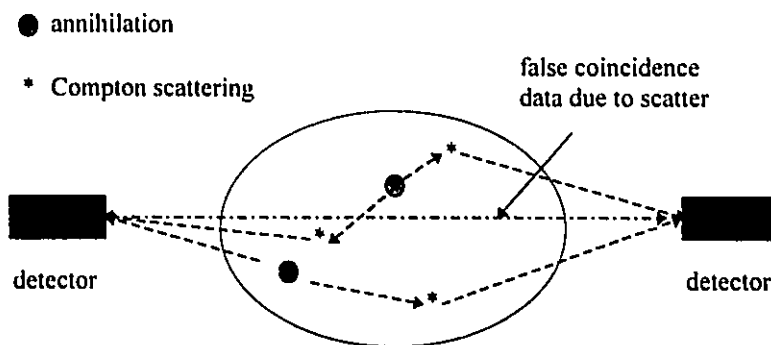


Figure 1.8 Scatter event occurs when one or both photons are Compton scattered and strikes the detectors within a coincidence timing window.

The second technique is scatter compensation in which the scattered events in each LOR are estimated and subtracted before image reconstruction. Sophisticated scatter compensation techniques have been developed, and they can be categorized roughly as either energy based scatter correction methods or filtered scatter correction methods.

Energy based scatter correction methods that make use of the energy information of the detected events have been used for some time in SPECT, particularly the dual-energy-window (DEW) technique (Jaszczak *et al* 1984). The DEW technique was modified and applied to PET data (Grootoink *et al* 1991, Harrison *et al* 1991). In brief, data are acquired in two non-overlapping energy windows: the photopeak window, and a second lower energy window. True and scattered events will be acquired in both

windows, but in different proportions. The lower energy window will contain a higher proportion of scattered events, and when scaled appropriately, will compensate for the scattered events in the photopeak window. The basic assumption of the technique is that the scaling factor measured using a simple phantom does not vary with object geometry and source distributions. The disadvantage of this technique is the propagation of noise as a noisy data set is subtracted from another noisy data set, and the increase in data storage necessary in dual energy window acquisition, especially in 3D mode. Another problem is that even though the technique is useful in removing the right proportion of counts from the photopeak window, it cannot discriminate between those LOR in which one or both photons have scattered from those in which none did. This implies that some LORs conveying erroneous position information are not eliminated, and some true coincidence counts are eliminated by this technique.

Filtered scatter correction techniques estimate the response of a point source of positron emitter at any position within the object being imaged. Since any source distribution is actually a superposition of many independent point sources, scatter profiles can be estimated by performing either convolution subtraction or deconvolution on the acquired projection data. Convolution subtraction was first proposed by Bergstrom *et al* in 1983. It models the scatter component as a convolution of the measured projection with a point spread function (PSF). The estimated scatter component can then be subtracted from the measured projection data. The technique, though, is slow since the convolution requires considerable computation time, and it cannot be done on-the-fly during data acquisition. Based on Bergstrom's method, more sophisticated and accurate techniques (Shao and Karp 1991, Barney *et al* 1993) have subsequently been proposed.

Techniques have also been developed which are neither energy based methods or filtered methods. The extraction of trues method (Bendriem *et al* 1994) is a hybrid technique based on both DEW and convolution correction methods. A scatter correction method for performing 3D scatter correction in PET was proposed by Cherry *et al* in

1993. An analytic 3D scatter correction based on the Klein-Nishina equation was developed by Bowen (1994).

REFERENCES

- Bacharach SL (1992). *The Physics of Positron Emission Tomography. In: Positron Emission Tomography of the Heart.* Bergmann SR, Sobel BE (eds). Mount Kisco, NY, Futura Publishing Company, Inc.
- Barney JS, Ronald H, and Dykstra CJ (1993). Source distribution dependent scatter correction for PVI. *IEEE Trans. Nucl. Sci.* 40:1001-1007.
- Bendriem B, Trebossen R, Frouin and Syrota A (1994). A PET scatter correction using simultaneous acquisitions with low and high lower energy thresholds. preprint:1-5
- Bergstrom M, Eriksson L, Bohm C, Blomqvist G, and Litton J (1983). Correction for scattered radiation in a ring detector positron camera by integral transformation of the projections. *J. Compt. Assist. Tomogr.* 7:42-50.
- Bowen C (1994) *Analytic 3D Scatter Correction in Positron Tomography Using the Klein-Nishina Equation.* McMaster University: M.Sc. Thesis.
- Cherry S, Meikle SR, and Hoffman EJ (1993). Correction and Characterization of scattered events in three-dimensional PET using scanners with retractable septa. *J. Nucl. Med.* 30:2029-2035.
- Dahlbom M, and Hoffman EJ (1987). Problems in signal-to-noise ratio for attenuation correction in high resolution PET. *IEEE Trans. Nucl. Sci.* 34:288-293.
- Dahlbom M, Eriksson L, Rosenqvist G, and Bohm C (1989). A study of the possibility of using multi-slice PET systems for 3D imaging. *IEEE Trans. Nucl. Sci.* 36:1066-1071.
- Evans RD (1982). *The Atomic Nucleus* New York: McGraw-Hill Book Company, Inc.

- Gelfand MJ and Thomas SR (1988). *Effective Use of Computers in Nuclear Medicine*
New York: McGraw-Hill Book Company.
- Grootoink S, Spinks TJ, Jones T, Michel C, and Bol A (1992). Correction for scatter using a Dual-Energy-Window technique with a tomography operated without septa. *IEEE 1991 Medical Imaging Conf. Rec. (Santa Fe, NM, 1991)* New York:IEEE 1569-1573.
- Harrison RL, Haynor DR and Lewellen TK (1992). Dual energy window scatter corrections for positron emission tomography. *IEEE 1991 Medical imaging Conf. Rec. (Santa Fe, NM, 1991)* New York:IEEE 1700-1704.
- Hoffman EJ, Huang SC, and Phelps ME (1979). Quantitation in positron emission computed tomography: 1. Effect of object size. *J. Comput. Assist. Tomogr.* 3:299-308.
- Hoffman EJ, Huang SC, Phelps ME, and Kuhl DE (1981). Quantitation in positron emission computed tomography: 4. Effect of accidental coincidences. *J. Comput. Assist. Tomogr.* 5:391-400.
- Hoffman EJ and Phelps ME (1986). Positron emission tomography: Principles and quantitation. *Positron Emission Tomography and Autoradiography: Principles and Applications for the Brain and Heart.* (Phelps M, Mazziotta, and Schelbert H, eds.) New York: Raven Press.
- Jaszczak RJ, Greer KL, Floyd CE, Harris CC, and Coleman RE (1984). Improved SPECT quantification using compensation for scatter photons. *J. Nucl. Med.* 25:893-900.
- Knoll GF (1989). *Radiation Detection and Measurement.* New York: John Wiley & Sons.
- Koral K, Clinthorne N, and Rogers WL (1986). Improving emission computed tomography quantitation by Compton scatter rejection through offset windows. *Nucl. Instrum. Methods A242:610-614.*
- Lederer CM, Hollander JM and Perlman I (1968). *Table of Isotopes 6th edn.* New York: Wiley.

Shao L and Karp J S (1991). Cross-plane scatter correction-point source deconvolution in PET. *IEEE Trans. Med. Imag.* 10:234-239.

Thompson CJ (1988). The effect of collimation on scatter fraction in multi-slice PET. *IEEE Trans. Nucl. Sci.* 35:598-602.

CHAPTER 2

ATTENUATION CORRECTION TECHNIQUES

The annihilation photons forming the image in positron tomography (PET) undergo significant attenuation before emerging from the body section being studied. Thus, attenuation correction is essential for quantitative PET imaging. Attenuation correction techniques have been developed, and they can be divided roughly into three categories: calculated, measured, or hybrid methods. The first technique applies a constant linear attenuation coefficient per unit distance to a measured chord length for each line of response (LOR), whereas the measured technique provides an estimate of the attenuation correction factor (ACF) for each LOR from the ratio of the events recorded from a transmission source with and without the object in the field of view. The third method is a combination of the first two techniques, in which appropriate attenuation coefficients are assigned to segmented regions in the transmission image. ACF for each LOR is then calculated by the exponent of the forward projected value from the segmented image. In this chapter, current techniques belonging to each category will be discussed.

2.1 CALCULATED ATTENUATION CORRECTION

Suppose the geometry of the object and its associated attenuation properties are known, ACFs can then be calculated for each line of response (LOR). The geometry of the object can be either approximated by an ellipse in the geometric outline method, or determined from the borders of the emission sinogram in the fitted outline method. Since no additional measurement is required, problems such as transmission/emission mismatch, random and scatter contamination in transmission data, and propagation of statistical noise from transmission data to emission data can be avoided. However, this method is only valid for simple geometries such as that of the brain. It is not possible to use this technique with any validity in the thorax because of the large size of the lungs, which have an attenuation coefficient about one-third of the surrounding tissue. Errors in the size and shape of the estimated contour will result in significant regional errors in tracer concentration estimation (Huang *et al* 1979). Therefore, the accuracy of this method depends on how well these physical parameters can be estimated.

2.1.1 Geometric Outline

The geometric outline method is a labor intensive technique. First, PET emission images are reconstructed without attenuation correction, and presented to a trained operator. The technique requires the operator to position an ellipse around each emission image. The orientation, size, and position of the ellipse are adjusted to fit the outline of the object as closely as possible. ACF for each LOR can then be calculated using the chord length of the LOR through the outlined ellipse, and an appropriate linear attenuation coefficient. After multiplying the emission projection data by the ACF's, attenuation corrected

emission images can be obtained by reconstructing the attenuation corrected projection data.

This technique is subjective and time consuming, as it requires two reconstructions, and user interaction for each transmission image. It is also subject to errors introduced by approximating the contour of the head by an ellipse.

2.1.2 Fitted Outline

Alternatively, the object shape may be obtained by using an edge detection algorithm applied on the emission images, provided that the tracer uptake in the region near the surface of the object is high enough. The detection of the object contour is done by thresholding the emission images (Thompson *et al* 1979). Once the object contour is determined, ACFs for each LOR can be calculated using appropriate linear attenuation coefficients, and attenuation corrected emission images can be obtained. This approach eliminates the ellipse fitting step, and thus yields a more accurate outline of the object.

However, it is more effective to determine the contour of a convex object from its projection data as this eliminates the reconstruction step for the object contour determination. Instead of thresholding the emission image, the object contour is estimated by thresholding the emission projection data (Bergstrom *et al* 1980). A refined version has been derived (Bergstrom *et al* 1982) such that the borders of the projections are determined by searching for the maximum slope from the outside of the object. In order to reduce the influence of noise, angular rebinning of the emission sinogram is done. The periphery of the object is then obtained by back-projecting these edges onto vectors issued from the object centroid and selecting the closest intersections to the centroid.

Another method using thresholding of emission projections has been developed by Tomitani *et al* (1987). This method uses a different approach for reducing noise. The estimated edge contour is smoothed by taking the Fourier transform of the edge contour and only the low frequency components in Fourier space are retained. The values of the threshold and the Fourier cutoff are selected in a way such that a smooth contour can be obtained.

Similar to Tomitani's approach, a technique has been developed (Michel *et al* 1989) which includes the attenuation of the head holder and a slightly modified algorithm for filtering. A more recent fitted outline method has been developed by Siegel *et al* (1992). The major departure from other methods is the partitioning of the emission sinogram into 16 sections with local thresholding, and the use of a Gaussian filter for noise suppression in the original sinogram.

Using the calculated methods for brain PET studies, it is important to account for the attenuation due to the skull bone (Tomitani *et al* 1987, Bergstrom *et al* 1982, Michel *et al* 1989). An underestimation causes all activity concentration values to be low, and the error becomes greater as one approaches the brain-skull interface, with an opposite effect if the skull thickness is overestimated. Attempts have been made to solve this problem based on different assumptions, such as assuming a constant skull thickness (Tomitani *et al* 1987, Siegel *et al* 1992), extending the attenuating soft-tissue region by a constant thickness (Bergstrom *et al* 1982) or assuming the extent of the soft-tissue is a constant fraction of the found contour while the rest is skull bone (Michel *et al* 1989). However, they do not account for variations in skull thickness such as the effects of lower attenuation through the eyes, nasal sinuses, etc.

2.2 MEASURED ATTENUATION CORRECTION

A different approach for correcting for attenuation is to measure directly the ACFs using an external source of radiation (Phelps *et al* 1975). Attenuation is independent of the source position and depends only upon the attenuation through the thickness of the body. Thus, attenuation can be measured using an external positron emitting source and two transmission measurements: a blank and a transmission scan. The blank and transmission scans are performed without and with the object in the field of view (FOV) of the tomograph. ACF's are then computed directly as blank/transmission.

In the ECAT 953/31, the transmission measurements are performed using a rod source of radiation (Derenzo *et al* 1981). The most commonly used source is $^{68}\text{Ge}/^{68}\text{Ga}$, and the rod is attached to a mechanism that rotates it at a constant speed around the gantry of the PET scanner.

Since it is a measure of the attenuation properties of the actual object, no assumptions are made about the shape and composition of the object being imaged. Obviously, this technique is more flexible and can be applied for body sections with significant non-homogeneities such as the thorax.

Although this technique is generally the accepted method for attenuation correction in cardiac PET studies, the technique is problematic. It has been shown (Huang *et al* 1979) that statistical noise in transmission measurements can significantly increase the noise level in reconstructed emission images. Practically, the transmission scan time is forced to be short, and the counting statistics are insufficient. Theoretically, a reduction in statistical fluctuations can be achieved by prolonging the transmission scan time. However, this will also increase the amount of patient discomfort, and the probability of errors in the ACFs due to patient motion (Huang *et al* 1979, McCord *et al* 1992, Bettinardi *et al* 1993, and Bacharach *et al* 1993). During a transmission scan, the recorded

data is inevitably contaminated by detection of photons which have been Compton scattered in the object being imaged, while almost no scatter is expected in the blank scan. Scattered photons cause detector pairs to register more events, and results in underestimation of the ACFs. Random coincidences are another source of noise in the transmission measurements. It affects the quantification in PET images by either distorting the image when random events are not subtracted from the total coincidence data, or increasing statistical noise through the subtraction (Hoffman *et al* 1981).

Since the noise in transmission data due to limited counting statistics, random coincidences and scattered radiation propagates to the measured emission data through the attenuation correction process, the success of the measured attenuation correction relies on how well one can reduce the noise from all of these sources.

Methods have been suggested for shortening the transmission scan time and reducing the noise in the measured transmission data. These include sinogram smoothing (Palmer *et al* 1986, Dahlbom *et al* 1987, Ostertag *et al* 1989), random sinogram processing (Casey *et al* 1986, Dahlbom *et al* 1987), reconstruction-reprojection (Riederer 1981), sinogram windowing (Huesman *et al* 1988, Kubler *et al* 1988, Ranger *et al* 1989), single-photon transmission measurements (deKemp and Nahmias 1994), scatter correction technique (Bergstrom *et al* 1980), and segmentation attenuation correction techniques (Huang *et al* 1981, Xu *et al* 1991, Meikle *et al* 1993, Xu *et al* 1994, Karp *et al* 1995). On the other hand, postinjection transmission measurements (Carson *et al* 1988, Daube-Witherspoon *et al* 1988) and simultaneous transmission/emission scans (Thompson *et al* 1991) have been proposed to reduce the total examination time, so that the likelihood of transmission/emission mismatch and patient discomfort can be minimized. This section will concentrate on a discussion of the measured attenuation correction technique and the related methods for improving the performance of the

technique. The segmented attenuation correction technique will be discussed in the next section.

2.2.1 Noise Reduction Techniques for Measured Attenuation Correction

2.2.1.1 sinogram smoothing

A common technique in noise reduction of transmission data is sinogram smoothing. It involves convolving the transmission sinogram and the blank sinogram individually with a Gaussian filter, so that a significant amount of image variance is removed (Palmer *et al* 1986, Dahlbom *et al* 1987, Ostertag *et al* 1989). Unfortunately, the reduction in variance is also accompanied by a degradation in spatial resolution. This mismatch in resolution between the transmission and emission measurements may lead to loss of quantitative accuracy and the generation of artifacts in the reconstructed emission images, particularly near the boundaries of the lung and the heart (Meikle *et al* 1993).

2.2.1.2 random sinogram processing

As mentioned in chapter 1, random events can be measured by the delayed coincidence technique. Events measured in the delayed coincidence window are subtracted to give the net true coincidence counts. If random events are stored in a separate sinogram, a better estimate of the random rate can be obtained using a technique developed by Casey *et al*

(1986). Thus, an indirect way of removing noise from transmission data can be achieved by removing noise in the random sinogram (Dahlbom *et al* 1987).

2.2.1.3 reconstruction-reprojection

A technique called reconstruction-reprojection, which reduces the variance of the transmission data was first proposed by Riederer (1981). Transmission data are first reconstructed to form an image, then ACFs are derived by reprojecting through the transmission image. Since there is a significant correlation between the means of individual projections, the technique is simply using this correlation to combine the projections such that the variance of the noisy projections is reduced.

Since the first step of this technique takes the natural logarithm of the ratio of the transmission sinogram to the blank sinogram, the logarithm tends towards negative infinity as the number of counts approaches zero, so this first step induces large noise spikes. On the other hand, the sinogram smoothing technique begins by smoothing the projections, so the number near zero tends to be filtered out. Thus, this technique shows inferior performance compared to the sinogram smoothing method for low-count transmission data (Ollinger 1992).

2.2.1.4 sinogram windowing

Instead of processing the transmission data, noise reduction can be achieved by modifying the acquisition procedure. From the exact knowledge of the position of the transmission source as it rotates around the patient, the scanner electronics can window out coincidences

which are not collinear with the source. Both random and scattered coincidence events are dramatically reduced and a better estimate of ACFs can be obtained, using this sinogram windowing technique (Huesman *et al* 1988, Kubler *et al* 1988). A slight modification was done by Ranger *et al* (1989) using a collimated orbiting point source instead of an orbiting rod source to reduce the dead time of the detectors. In this way, more true coincidence counts are recorded and a stronger source can be used to reduce the acquisition time. By subtracting an estimated fraction of the emission data from the transmission data and using this technique, postinjection transmission measurements (Carson *et al* 1988, Daube-Witherspoon *et al* 1988) and simultaneous transmission/emission acquisitions (Thompson *et al* 1991) were shown to be feasible. Therefore, sufficient photon statistics can be obtained by lengthening the transmission scan duration but not the total scanning time using these techniques. However, this approach is not ideal due to the sensitivity of the method to inaccuracies in emission subtraction (Daube-Witherspoon *et al* 1988) especially for emission source distributions containing localized hot regions. Although most of the random and scatter coincidences have been eliminated, correction for the residue is necessary to obtain more accurate ACFs.

2.2.1.5 single photon transmission measurement

The best way to increase the signal-to-noise ratio (SNR) in the transmission measurements is definitely by improving counting statistics. Theoretically, it can be achieved by prolonging the acquisition time and/or increasing the transmission source strength. However, high SNR transmission data usually require intolerably long scan times in real practice, and the source strength is limited by the dead time of the detector adjacent to the source.

Since the physical position of the transmission source is known, detection of the singles annihilation photons that strike the detectors across the FOV provides sufficient information to define a LOR. Based on this principle, a single-photon transmission measurement technique has been developed (deKemp and Nahmias 1994). Using this technique, the SNR is increased significantly due to a reduction in dead time losses and the elimination of random coincidences. The count rate can also be further increased because the reduction in dead time allows one to use a stronger source.

2.2.1.6 scatter correction for transmission measurement

As mentioned in chapter 1, scatter suppression techniques such as raising the energy discrimination threshold in the acquisition window (Dahlbom *et al* 1987), and placing septa between detector rings (Thompson 1988) are not sufficient to eliminate scatter events from measured data. Therefore, techniques are required to account for the contamination in the transmission data due to scattered radiation.

A post acquisition scatter correction method for transmission measurements was developed that subtracts an estimated scatter profile from the projection data (Bergstrom *et al* 1980). The scatter profile is obtained by fitting a 'standard' curve of scatter to the projection data within the background regions. This technique works reasonably well for simple object geometry, but does not work well for complex geometry such as the thorax. This is because the technique fails to account for the inhomogeneous distribution of the attenuation medium.

2.3 HYBRID ATTENUATION CORRECTION

It is possible to realize the benefits of both the calculated and measured attenuation corrections while minimizing their disadvantages by combining the two methods. This is achieved by acquiring a short transmission scan, and removing noise from the reconstructed transmission images using a segmentation algorithm.

Techniques have been developed, and they can be roughly divided into two categories, namely discrete attenuation methods and continuous attenuation methods. Discrete attenuation methods (Huang *et al* 1981, Xu *et al* 1991, Karp *et al* 1995) segment the major structures such as the lungs, soft tissue and air from the transmission image into different regions. Each region is then assigned either an attenuation coefficient which is equal to the average of the reconstructed attenuation coefficient in each of the regions, or the theoretical attenuation coefficient of the tissue type to each of the regions according to the classification. The segmented transmission image thus contains discrete values of attenuation coefficients.

Instead of discrete attenuation coefficients, continuous attenuation coefficients are assigned to the segmented images using the continuous attenuation methods (Meikel *et al* 1993, Xu *et al* 1994). One of the approaches (Meikel *et al* 1993) uses a pixel intensity histogram of the transmission image to estimate the probabilities of a given pixel belonging to one of the three tissue types: air, lung or soft tissue. The new pixel values in the segmented image are then computed as the sum of the product of the estimated probabilities and the corresponding attenuation coefficients for the three tissue types. The other approach is similar to the discrete attenuation method developed by Karp *et al* (1995), except that the segmented images are smoothed and recombined with the original transmission images in a weighted fashion to give continuous attenuation coefficients in the final segmented images.

After the segmented images are created, ACFs are then computed by taking the exponent of the forward projected value from the segmented image. The discrete and continuous attenuation methods are practical and capable of reducing both the transmission scan time and the noise in the ACFs.

2.3.1 Discrete Segmentation Methods

The potential of applying the segmentation technique to process transmission images was first suggested by Huang *et al* (1981). They proposed to smooth the transmission image using a Gaussian filter and a Laplacian filter, then to segment the transmission image into three discrete regions (air, lung and soft tissue) using an edge-tracing algorithm. Each segmented region is assigned a uniform attenuation coefficient equal to the average value within the region of the original transmission image. Thus, the image is quantized into a few discrete levels of attenuation coefficients. This method removes noise from the original transmission images, but it may also introduce error to the ACFs due to falsely detected edges because conventional edge-detection methods, such as gradient and Laplacian, do not work well in noisy images. This method is also time-consuming and subjective, since it requires operator interactions.

Based on Huang's method, Xu *et al* (1991) proposed a segmented attenuation correction (SAC) method which automatically determines organ boundaries by thresholding the pixel intensity histogram of the transmission image. Figure 2.1 shows the transmission images and their pixel intensity histograms acquired in a practical scan time (30 minutes) and a long scan time (3 hours), respectively. The two thresholds for identifying soft tissue, air and lungs are selected by examining the relation between the thresholds and the polar map quantitative recovery for the whole heart from a few clinical

cases. This technique is fast, but the borders of the body contour are always misclassified to lung tissue.

To eliminate this misclassification problem, Karp *et al* (1995) proposed a SAC technique which extracts the body contour using a threshold determined from the pixel intensity histograms of the transmission image. Three transmission subimages are then created: (1) region enclosed by body contour; (2) region below the bottom of the body, and (3) region above the bottom of the body and outside the body contour. Pixel intensity histograms were generated for subimages (1) and (2). The lungs are then separated from soft tissue using a second threshold determined from the pixel intensity histogram of subimage (1). Similarly, the patient table is segmented by thresholding the pixel intensity histogram of subimage (2). Subimage (3) does not require segmentation since it contains only air and all pixels in subimage (3) are assigned to the value of attenuation coefficient for air. A morphological operation, erosion, is then applied to smooth the segmented boundaries in each subimage. The final segmented transmission image was created by merging the three processed subimages.

These automated SAC techniques are practical and objective. A problem of this approach, though, is that different regions of the lungs may have different attenuation properties, especially for patients with pulmonary edema. Moreover, the segmented attenuation data may be erroneous if the original transmission image is very noisy.

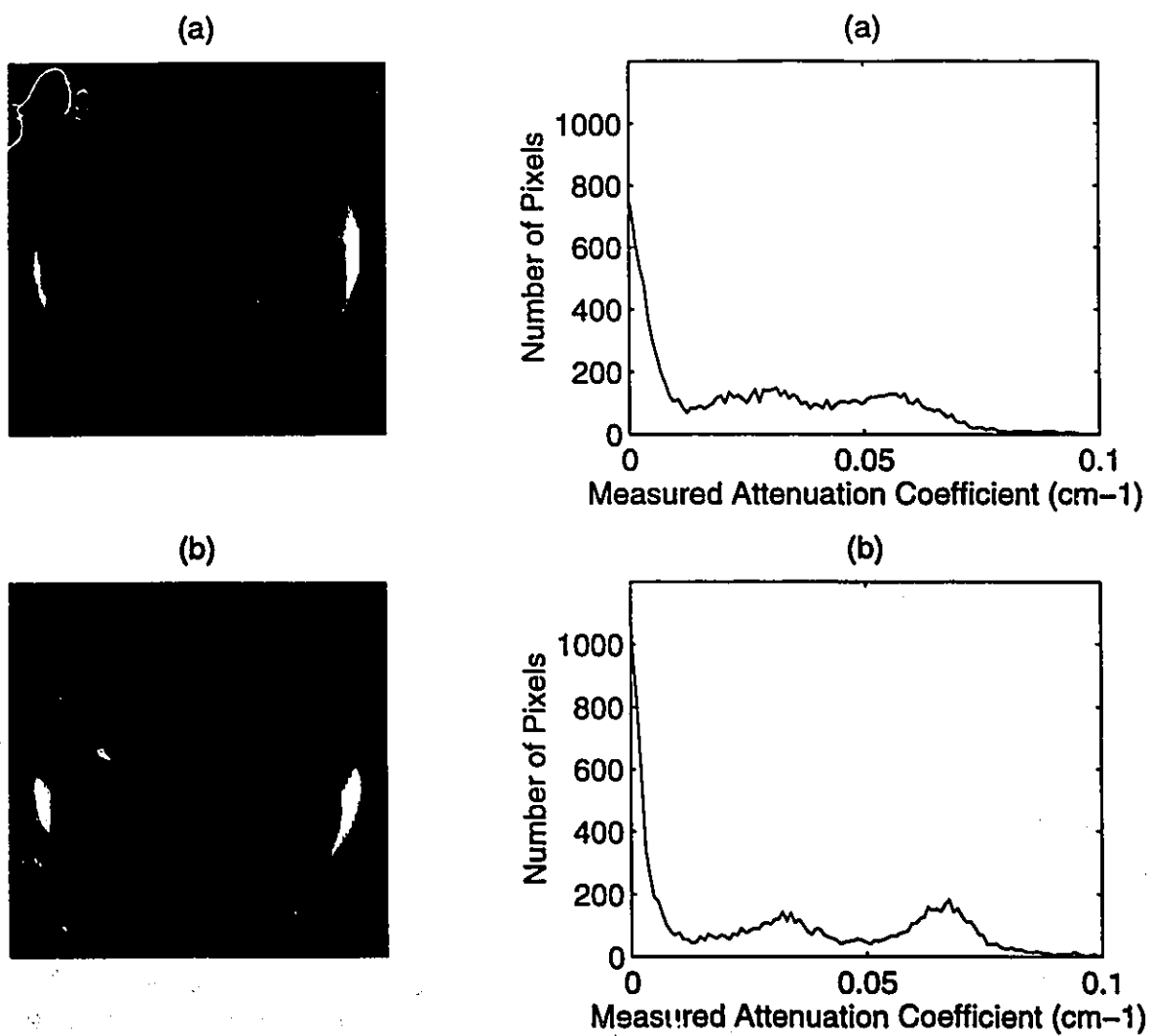


Figure 2.1 Transmission images and their pixel intensity histograms acquired in (a) practical scan time, (b) long scan time.

2.4.2 Continuous Segmentation Methods

Since not all anatomic regions can be classified as a particular tissue type, it is better to obtain segmented transmission images with continuous pixel values. After all, the task is to reduce noise in the ACFs, not to classify the transmission image. A continuous attenuation method was introduced by Meikle *et al* (1993). First, the original transmission images are processed with a three-dimensional median filter to improve the signal-to-noise ratio. A pixel intensity histogram is subsequently created using the filtered transmission image. An estimation of the probabilities of a given pixel value belonging to one of three tissue types: air, soft tissue or lung is done by fitting a Gaussian function to each of the three peaks in the filtered histograms. Continuous pixel values are then assigned as the sum of the product of the estimated probability for each tissue class and the corresponding attenuation coefficients for that tissue type.

This method is practical and objective. However, there are problems in the assignment of the appropriate linear attenuation coefficients to pixels in the segmented image. Since the transmission image is noisy, a region in a same attenuation medium may end up having large variation of segmented attenuation values due to the large variance of pixel values in the transmission image.

Another continuous attenuation method has been developed by Xu *et al* (1994) using global and local pixel intensity histograms for segmentation. This technique is similar to Karp's technique. The major differences are that the discrete segmented transmission images are smoothed then recombined with the original transmission images in a weighted fashion, and the patient table is added using a separate high-statistics transmission image of the table instead of segmenting the table from a transmission subimage.

This technique has the same problems as the discrete attenuation methods. Other problems of this technique come from the process of combining the original transmission image with the segmented image. Since attenuation coefficients in the transmission image are underestimated due to scattered radiation; the final segmented attenuation data are underestimated unless the original transmission data are corrected for scatter. The other shortcoming is that the noise in the transmission image will propagate to the final segmented image through the combination process.

REFERENCES

- Bacharach SL, Douglas MA, Carson RE, Kalkowski PJ, Freedman NMT, Perrone-Filardi P, and Bonow RO (1993). Three-dimensional registration of cardiac positron emission tomography attenuation scans. *J. Nucl. Med.* 34:311-321.
- Bergstrom M, Bohm C, Ericson K, Eriksson L, and Litton J (1980). Corrections for attenuation, scattered radiation, and random coincidences in a ring detector positron emission transaxial tomograph. *IEEE Trans. Nucl. Sci.* 27:549-554.
- Bergstrom M, Litton J, Eriksson L, Bohm C, and Blomqvist (1982). Determination of object contour from projections for attenuation correction in cranial positron emission tomography. *J. Comput. Assist. Tomogr.* 6:365-372.
- Bettinardi V, Gilardi MC, Lucignani G, Landoni C, Rizzo G, Striano G, and Fazio F (1993). A procedure for patient repositioning and compensation for misalignment between transmission and emission data in PET heart studies. *J. Nucl. Med.* 34:137-142.

- Carson RE, Daube-Witherspoon ME, and Green MV (1988). A method of postinjection PET transmission measurements with a rotating source. *J. Nucl. Med.* 29:1558-1567.
- Casey ME and Hoffman EJ (1986). Quantitation in positron emission computed tomography: 7. A technique to reduce noise in accidental coincidence measurements and coincidence efficiency calibration. *J. comput. Assist. Tomogr.* 10:845-850.
- Dahlbom M and Hoffman EJ (1987). Problems in signal-to-noise ratio for attenuation correction in high resolution PET. *IEEE Trans. Nucl. Sci.* 34:288-293.
- Daube-Witherspoon ME, Carson RE, and Green MV (1988). Post-injection transmission attenuation measurements for PET. *IEEE Trans. Nucl. Sci.* 35:757-761.
- deKemp R and Nahmias C (1994). Attenuation correction in PET using single photon transmission measurement. *Med. Phys.* 21:771-778.
- Derenzo SE, Budinger TF, Huesman RH, Cahoon JL, and Vuletich T (1981). Imaging properties of a positron tomograph with 280 BGO crystals. *IEEE Trans. Nucl. Sci.* 28:81-89.
- Hoffman EJ, Huang SC, Phelps ME, and Kuhl DE (1981). Quantitation in positron emission computed tomography: 4 Effect of accidental coincidences. *J. Comput. Assist. Tomogr.* 5:391-400.
- Huang SC, Carson RE, Phelps ME, Hoffman EJ, Schelbert HR, and Kuhl DE (1981). A boundary method for attenuation correction in positron computed tomography. *J. Nucl. Med.* 22:627-637.
- Huang SC, Hoffman EJ, Phelps ME, and Kuhl DE (1979). Quantitation in positron tomography: 2. Effects of inaccurate attenuation correction. *J. Comput. Assist. Tomogr.* 3:804-814.

- Huesman RH, Derenzo SE, Cahoon JL, Geyer AB, Moses WW, Uber DC, Vuletich T, and Budinger TF (1988). Orbiting transmission source for positron tomography. *IEEE Trans. Nucl. Sci.* 35:735-739.
- Karp JS, Muehllehner G, Qu H, and Yan XH (1995). Singles transmission in volume-imaging PET with a ^{137}Cs source. *Phys. Med. Biol.* 40:929-944.
- Kubler WK, Ostertag H, Hoverath H, Doll J, Ziegler S, and Lorenz WJ (1988). Scatter suppression by using a rotating pin source in PET transmission measurements. *IEEE Trans. Nucl. Sci.* 35:749-752.
- McCord ME, Bacharach SL, Bonow RO, Dilsizian V, Cuccolo A, and Freedman N (1992). Misalignment between PET transmission and emission scans: its effect on myocardial imaging. *J. Nucl. Med.* 33:1209-1214.
- Meikle SR, Dahlbom M, and Cherry SR (1993). Attenuation correction using count-limited transmission data in positron emission tomography. *J. Nucl. Med.* 34:143-150.
- Michel C, Bol A, De Volder AG, and Goffinet AM (1989). Online brain attenuation correction in PET: towards a fully automated data handling in a clinical environment. *Eur. J. Nucl. Med.* 15:712-718.
- Ollinger JM (1992). Reconstruction-reprojection processing of transmission scans and the variance of PET images. *IEEE Trans. Nucl. Sci.* 39:1122-1125.
- Ostertag H, Kubler WK, Doll Josef, and Lorentz WJ (1989). Measured attenuation correction methods. *Eur. J. Nucl. Med.* 15:722-726.
- Palmer MR, Rogers JG, Berstrom M, Beddoes MP, and Pate BD (1986). Transmission profile filtering for positron emission tomography. *IEEE Trans. Nucl. Sci.* 33:478-481.
- Phelps ME, Hoffman EJ, Mullani NA, and TerPogossian M (1975). Application of annihilation coincidence detection to transaxial reconstruction tomography. *J. Nucl. Med.* 16:210-224.

- Ranger NT, Thompson CJ, and Evans AC (1989). The application of a masked orbiting transmission source for attenuation correction in PET. *J Nucl. Med.* 30:1056-1068.
- Riederer SJ (1981). Application of the noise power spectrum to position emission CT self-absorption correction. *Med. Phys.* 8:220-224.
- Siegel S and Dahlbom M (1992). Implementation and evaluation of a calculated attenuation correction for PET. *IEEE Trans. Nucl. Sci.* 39:1117-1121.
- Thompson CJ, Yamamoto YL, and Meyer E (1979). Positome II. A high efficiency positron imaging device for dynamic brain studies. *IEEE Trans. Nucl. Sci.* 26:583-589.
- Thompson CJ (1988). The effect of collimation on scatter fraction in multi-slice PET. *IEEE Trans. Nucl. Sci.* 35:598-602.
- Thompson CJ, Ranger N, Evans AC, and Gjedde A (1991). Validation of simultaneous PET emission and transmission scans. *J. Nucl. Med.* 32:154-160.
- Tomitani T (1987). An edge detection algorithm for attenuation correction in emission CT. *IEEE Trans. Nucl. Sci.* 34:309-312.
- Xu EZ, Mullani NA, Gould KL, and Anderson WL (1991). A segmented attenuation correction for PET. *J. Nucl. Med.* 32:161-165.
- Xu M, Luk WK, Cutler PD, and Digby WM (1994). Local threshold for segmented attenuation correction of PET imaging of the thorax. *IEEE Trans. Nucl. Sci.* 41:1532-1537.

CHAPTER 3

SINGLE-PHOTON TRANSMISSION MEASUREMENTS USING ^{137}Cs

A technique for measuring transmission data that relies on the detection of photons in 'singles' mode rather than 'coincidence' mode has been developed (deKemp and Nahmias 1994). As mentioned in chapter 2, substantial increase in the statistical accuracy of the transmission data can be achieved using this single-photon transmission measurement technique. This technique also releases the restriction of the choice of transmission sources to those that decay by positron emission. For this purpose, ^{137}Cs is proposed to be a suitable isotope. As compared to $^{68}\text{Ge}/^{68}\text{Ga}$, the traditional source used in coincidence transmission measurements, ^{137}Cs is more economical because of a longer half-life and lower cost. ^{137}Cs can be used for single-photon transmission measurements without any recalibration of the tomograph, and the spatial resolution is comparable to that obtained using $^{68}\text{Ge}/^{68}\text{Ga}$ in 'coincidence' mode. Since ^{137}Cs emits a monoenergetic gamma ray at 662 keV and emission data are acquired by detecting annihilation photons of energy 511 keV, a simple method is developed to extrapolate the attenuation coefficients measured at 662 keV to 511 keV. To eliminate scatter contamination in transmission data, the dual-energy-window scatter correction technique is modified so that correction can be made on-the-fly during data acquisition. As indicated in section 3.5 (table 3.4, page 55), the measured linear attenuation coefficients using the newly developed technique agree with the theoretical values (Yu and Nahmias 1995).

3.1 INTRODUCTION

Transmission measurements in 'coincidence' mode are limited to the use of expensive sources of positron emitters. In coincidence counting, the dead time of the detectors located next to the source is high; this limits severely the count rate and hence the statistical accuracy of the measurements in practical scan time. Recently, a technique called single-photon transmission measurements (deKemp and Nahmias 1994) was developed to remove the coincidence requirement. In this technique, single annihilation photons are recorded in the detectors opposite the transmission source. This results in a fivefold to tenfold increase in count rate, and in the concomitant improvement in statistics. Hence, radioisotopes that emit monoenergetic gamma rays at about 511 keV, such as ^{85}Sr ($E_{\gamma}=514$ keV (100%), $T_{1/2}=64$ days), could be used as transmission sources. However, more convenient radioisotopes could be used if transmission measurements could be done using gamma rays with energy other than 511 keV.

Using radionuclides with different photon energies was first introduced in radioisotope scanning by Kuhl *et al* (1966) to obtain simultaneously the distribution of a radionuclide in the body as well as an estimate of the corresponding anatomy in the patient. The technique of using radionuclides with different photon energies to perform simultaneous transmission/emission measurements has also been applied to single-photon-emission-computed-tomography studies. This was done in an effort to reduce the examination time required if separate transmission and emission scans had to be performed (Bailey *et al* 1987, Ljungberg and Strand 1990). A refinement of the technique that overcomes the limitation that the transmission radionuclide be of lower energy than the emission radionuclide has been described (Tan *et al* 1993). All of these techniques rely on pulse height analysis to separate the emissions from the different radionuclides.

In positron tomography, one of the advantages of using photon energies other than 511 keV is to offer more choice of radioisotopes for transmission measurements.

However, the relatively poor energy resolution of the BGO detectors precludes the separation of two emissions using pulse height analysis techniques. The reliance on relative light distribution in a detector block to give spatial localization within the block requires that this distribution be similar for the proposed radionuclides. Furthermore, in order to use transmission data measured at other energies, the measured data must be extrapolated to the values of those obtained with 511 keV photons.

3.2 SUITABLE RADIOISOTOPES FOR SINGLE-PHOTON TRANSMISSION MEASUREMENTS IN PET

There are a number of factors that need to be considered in the selection of a radioisotope as the radiation source for single-photon transmission measurements. First, radioisotopes that emit monoenergetic gamma rays are preferable. Otherwise, the measured attenuation coefficients will be inaccurate if the detected events originally come from gamma rays with different energies. Furthermore, any emitted gamma rays, which are excluded by the energy window, not only give no information in the transmission measurements, but also increase the radiation dose to the patient. The relative light distribution in a detector block at the energy of the transmission source should be similar to that obtained from 511 keV photons. This enables the scanner to perform transmission and emission measurements with the same set of calibration data. Moreover, the probability of photon detection by the BGO detectors decreases with increase in photon energy; whereas larger angle scattered events will be recorded for photons with lower energies. High probability of the gamma ray emission is also important. Possible contamination of the measured transmission data from the associated emitted radiation such as characteristic X-rays and bremsstrahlung should be kept minimal. Ideally, the energies of the associated radiation should be lower than the lower energy discrimination level of the acquisition window, so that this

associated radiation will not be recorded during the transmission measurements. Practically, the half-life of the isotope should be long so that the radioactivity in the transmission source is maintained at a steady level. This also makes the transmission source more convenient and more economical to use in practice since it does not need to be replaced frequently. The financial cost of the isotope is also an important concern from an economic point of view.

Table 3.1 List of monoenergetic gamma ray emitters with $T_{1/2} > 30$ days, gamma ray energy ranging from 400 keV to 700 keV (from Lederer *et al* 1968).

Radioisotopes	$T_{1/2}$	Major radiation : approximate energies (MeV) and intensities		Principal means of production
^7Be	53.6 days	γ	0.477 (10.3%)	$^6\text{Li}(d,n)^7\text{Be}$ $^{10}\text{B}(p,\alpha)^7\text{Be}$ $^{12}\text{C}(^3\text{He},2\alpha)^7\text{Be}$
^{36}Cl	3.08×10^5 years	β^- γ	0.714 max S X-rays, 0.511 (0.003%)	$^{35}\text{Cl}(n,\gamma)^{36}\text{Cl}$
^{85}Kr	10.76 years	β^- γ	0.67 max 0.514 (0.41%)	$^{84}\text{Kr}(n,\gamma)^{85}\text{Kr}$
^{85}Sr	64 days	γ e^-	Rb X-rays, 0.514 (100%) 0.499	$^{84}\text{Sr}(n,\gamma)^{85}\text{Sr}$ $^{85}\text{Rb}(p,n)^{85}\text{Sr}$ $^{85}\text{Rb}(d,2n)^{85}\text{Sr}$
^{137}Cs	30.0 years	β^- e^- γ	1.176 max (7%), 0.514 max 0.626, 0.656 Ba X-rays, 0.662 (85%)	fission
^{240}Pu	6580 years	α γ e^-	5.17 (76%), 5.12 (24%) U L X-rays, 0.65 ($2 \times 10^{-5}\%$) 0.026, 0.040	multiple n-capt from ^{238}U , ^{239}Pu

Table 3.1 (Lederer *et al* 1968) lists the radioisotopes with a half-life greater than 30 days, that emit monoenergetic gamma rays with energies in the range from 400 keV to 700 keV. The associated radiation emitted from the radioisotopes and the principal means of production are also included. Note the probabilities of gamma ray emission are low for ^7Be , ^{36}Cl , ^{85}Kr and ^{240}Pu as compared to either ^{85}Sr or ^{137}Cs . Since the half-life of ^{137}Cs is

much longer than that of ^{85}Sr , and its cost is lower, selection of ^{137}Cs for single-photon transmission measurement in PET is sensible.

3.3 ^{137}Cs AS A TRANSMISSION SOURCE IN PET

^{137}Cs emits two beta particles with maximum energies of 1.176 MeV (6.5%) and 0.514 MeV (93.5 %); two electrons with 0.626 MeV and 0.656 MeV; a monoenergetic gamma ray with 662 keV (85 %) and barium x-rays (Lederer *et al* 1968). The energies of the barium x-rays are all below 40 keV and they will be excluded by the energy window in transmission data acquisition. The continuous slowing down approximation (CSDA) range for a 1.25 MeV electron in Perspex is $0.5902 \text{ cm}^2 \text{ g}^{-1}$ and the density of Perspex is 1.190 g cm^{-3} (Berger and Seltzer 1983). Thus, approximately 7 mm of Perspex should be sufficient to shield the two beta particles and the two electrons emitted from ^{137}Cs . When the beta particles and electrons interact in the shield, part of their energy is converted into electromagnetic radiation in the form of bremsstrahlung. This bremsstrahlung is unavoidable but can be minimized by using a low-atomic-number shielding material. The radiation yields, the fractions of initial energy of an electron that are converted to bremsstrahlung energy as the electron slows down to rest, for 0.55 keV and 1.25 keV electrons in Perspex are 1.9×10^{-3} and 3.9×10^{-3} , respectively. Therefore, the bremsstrahlung generated from 0.514 MeV and 1.176 MeV beta particles is less than 0.19 % and 0.39 %, respectively, and can be neglected. Similarly, the bremsstrahlung generated from the 0.626 MeV and 0.656 MeV electrons is less than 0.5 %. Hence, more than 99.7 % of the detected events are from the 662 keV gamma rays.

The half-life of ^{137}Cs is 30 years, approximately 40 times longer than the half-life of $^{68}\text{Ge}/^{68}\text{Ga}$. A batch of 5 mCi $^{68}\text{Ge}/^{68}\text{Ga}$ usually costs a few thousand dollars, but a

batch of the same activity of ^{137}Cs only costs a few hundred dollars. Thus, ^{137}Cs is more economical than $^{68}\text{Ge}/^{68}\text{Ga}$ in terms of longer half-life and lower financial cost.

As mentioned in chapter 1, the ECAT 953/31 uses blocks of detectors of BGO coupled to four photomultiplier tubes (PMTs). The relative amount of scintillation light collected by each of the PMTs from an interaction in the block will determine to which element within the block this interaction will be assigned. For this, calibration of each block of detectors in the tomograph is required. In this process, the gains of the PMTs are set to provide the same count rate by each detector in response to a uniform source of gamma rays.

Experiments were carried out by illuminating either all rows of one of the eight columns at once, or all columns of one of the eight rows. Two lead blocks were placed in parallel with a 4 mm gap between them in order to collimate the incoming photons to either a row or a column of detectors. A 1 mCi radioactive source of either ^{137}Cs or $^{68}\text{Ge}/^{68}\text{Ga}$ was positioned at the opposite side of the gantry.

Table 3.2. The ratio of mean light output from an irradiated row (r) or column (c) to that of the adjacent unirradiated rows or columns in an eight detector block.

	$^{68}\text{Ge}/^{68}\text{Ga}$	^{137}Cs
r1	0.21 ± 0.02	0.25 ± 0.02
r2	0.26 ± 0.02	0.32 ± 0.02
r3	0.29 ± 0.02	0.30 ± 0.02
r4	0.21 ± 0.02	0.31 ± 0.02
c1	0.39 ± 0.02	0.13 ± 0.02
c2	0.28 ± 0.02	0.13 ± 0.02
c3	0.23 ± 0.02	0.12 ± 0.02
c4	0.14 ± 0.02	0.12 ± 0.02

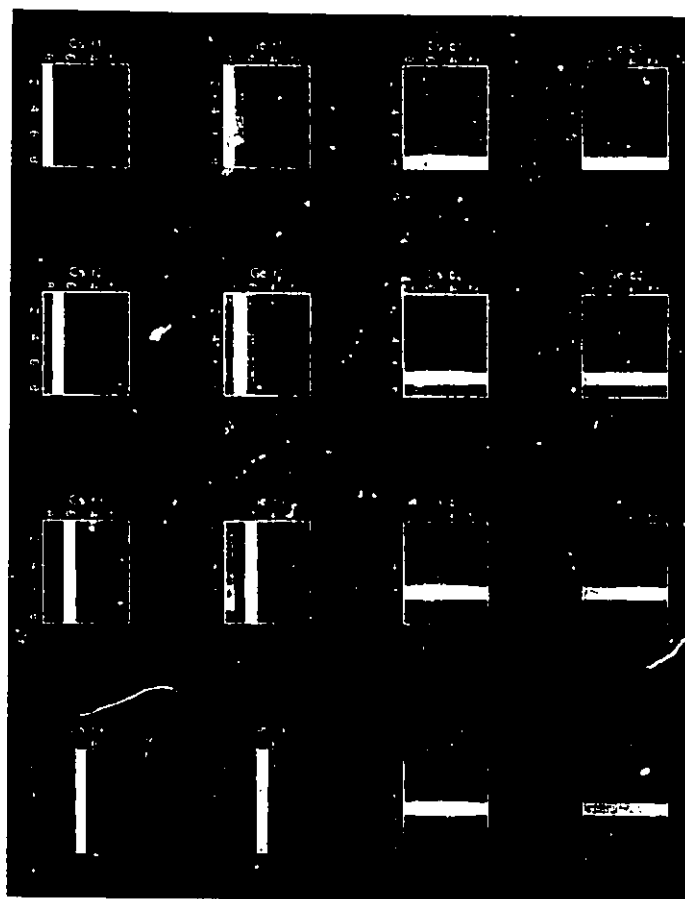


Figure 3.1 Light output from an 8x8 block of detectors. A row (r1..r4) or a column (c1..c4) was irradiated by a point source of either $^{68}\text{Ge}/^{68}\text{Ga}$ (Ge) or ^{137}Cs (Cs) collimated using two parallel lead blocks.

Results from figure 3.1 and table 3.2 show that the light output distribution from a ^{137}Cs source is approximately that from $^{68}\text{Ge}/^{68}\text{Ga}$. By removing the lead collimation, a comparable light output is obtained from both sources as shown in figure 3.2. In this case, the mean output value was 1858 ± 453 counts when using $^{68}\text{Ge}/^{68}\text{Ga}$ source, and 2139 ± 616 counts when using the ^{137}Cs source. These results indicate that ^{137}Cs can be used for single-photon transmission measurement without any recalibration of the tomograph.

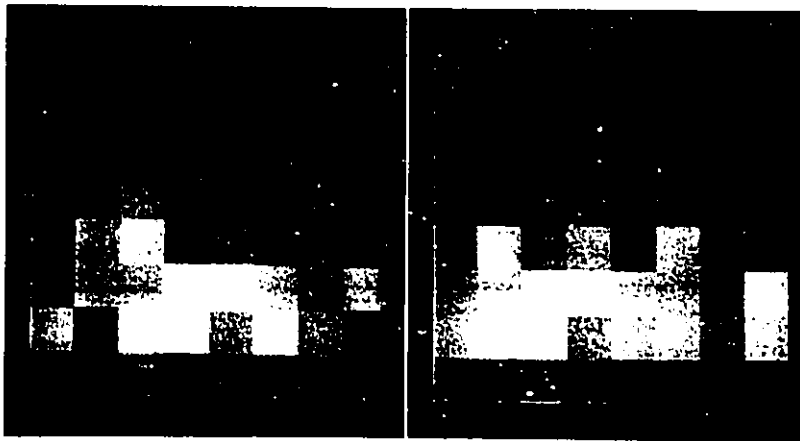


Figure 3.2 Light distribution in an 8x8 block of detectors. An uncollimated point source of either $^{68}\text{Ge}/^{68}\text{Ga}$ (Ge)(left) or ^{137}Cs (Cs) (right) was positioned 62 cm away from the detectors.

An estimate of transaxial resolution was obtained using the transmission image of a 21 cm cylindrical water phantom positioned off center in the FOV, such that an edge of the phantom was 0 cm, 5 cm, or 10 cm from the center. Transmission and blank scans were acquired in singles mode for at least 100 million counts. The energy window used for acquisition was 350-850 keV for $^{68}\text{Ge}/^{68}\text{Ga}$, and 450-950 keV for ^{137}Cs . Images were reconstructed, without smoothing, using a ramp filter cut-off at the Nyquist frequency. The reconstructed pixel size was 2 mm x 2 mm. The edge response was estimated by

measuring the half width at half maximum (HWHM) at the edge of the phantom, and assuming the full width at half maximum (FWHM) to be twice the HWHM.

Little difference was observed in the measured edge response at 662 keV and 511 keV. The FWHM was estimated to be 5 mm, 6 mm and 7 mm at the center of the field of view and 5 cm and 10 cm away, respectively. Theoretically, a slightly better resolution should be obtained at 662 keV than at 511 keV because of fewer scattered photons. However, because of the limitations on the pixel size imposed by the sampling distance of the tomograph, more accurate measures could not be obtained.

3.4 EXTRAPOLATION OF ATTENUATION CORRECTION FACTORS

Since the emission data are acquired by detecting annihilation photons of energy 511 keV, attenuation data measured at other energies must be extrapolated to those values that would have been measured with 511 keV photons. For composite materials, the effective mass attenuation coefficient can be calculated by

$$\frac{\mu}{\rho} = \sum \frac{f_i \mu_i}{\rho_i} \quad (3.1)$$

where μ/ρ is the effective mass attenuation coefficient (μ), f_i is the weighting factor of material i and μ_i (equal to μ_i/ρ_i) is the mass attenuation coefficient of material i .

A plot of the ratios of the mass attenuation coefficient of biological tissues to water as a function of energy is shown in figure 3.3 (Hubbell 1992). The ratios do not vary significantly for most biological tissues in the energy range from 400 keV to 1 MeV. Hence,

$$\frac{u(E)_i}{u(E)_w} = k_i, \quad 400 \text{ keV} \leq E \leq 1 \text{ MeV} \quad (3.2)$$

where k_i is a constant for tissue i . Dividing equation (3.1) by u_w ,

$$\frac{u(E)}{u(E)_w} = \sum \frac{f_i u(E)_i}{u(E)_w} = \sum f_i k_i, \quad (3.3)$$

and since both f_i and k_i are energy independent,

$$u(511) = \frac{u(E)u(511)_w}{u(E)_w} = u(662) \frac{0.96}{0.87} \quad \text{for } E = 662 \text{ keV} \quad (3.4)$$

where $u(E)$ is the mass attenuation coefficient at energy E keV, $u(511)_w = 0.0096 \text{ m}^2 \text{ kg}^{-1}$ and $u(662)_w = 0.0087 \text{ m}^2 \text{ kg}^{-1}$, obtained by fitting a fourth-order polynomial to the published data of $u(E)_w$ (Hubbell 1982).

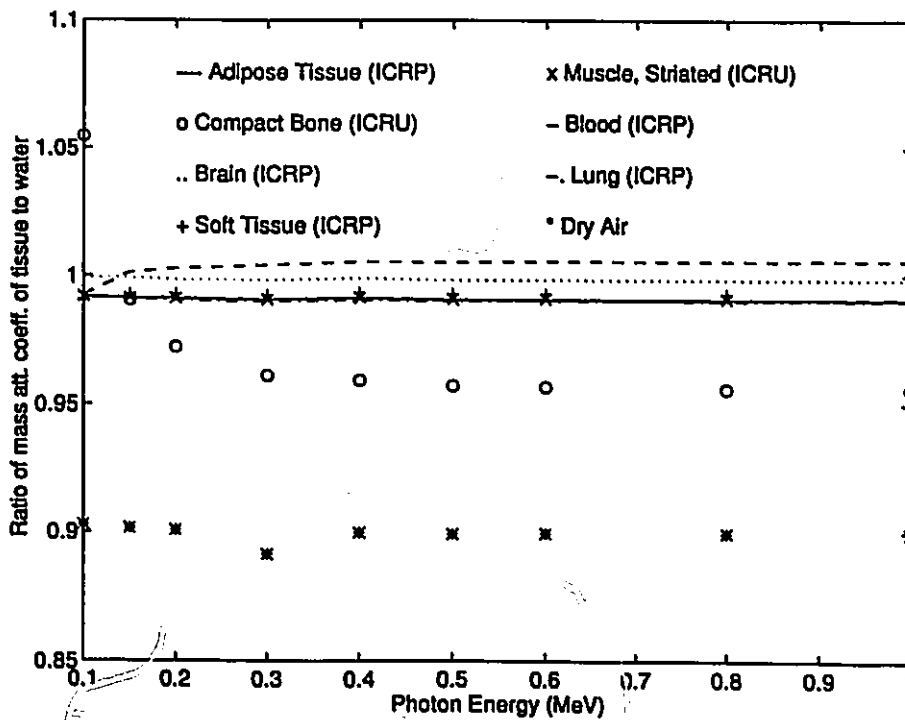


Figure 3.3 Ratio of mass attenuation coefficient of biological tissues to water.

A beam of monoenergetic photons is attenuated to an intensity I from an incident intensity I_o when passed through layers of tissue with mass thickness t_i according to the exponential absorption law,

$$I = I_o B \exp\left(-\sum u_i t_i\right) \quad (3.5)$$

where B is the build-up factor caused by scattered photons. Theoretically, B will be reduced to unity after scatter correction. By taking the logarithm, rewriting the equation (3.5) with $B = 1$ and dividing both sides of the equation by u_w ,

$$\sum \frac{u_i t_i}{u_w} = \frac{\ln(I_o / I)}{u_w} \quad (3.6)$$

Since both the total mass thickness and the ratio of mass attenuation coefficients are not energy dependent,

$$\frac{\ln[I_o(E) / I(E)]}{u(E)_w} = \frac{\ln[I_o(511) / I(511)]}{u(511)_w} \quad (3.7)$$

Thus,

$$\ln\left[\frac{I_o(511)}{I(511)}\right] = \left\{ \ln\left[\frac{I_o(E)}{I(E)}\right] \right\} \left[\frac{u(511)_w}{u(E)_w} \right] = \ln\left[\frac{I_o(662)}{I(662)}\right] \frac{0.96}{0.87} \quad \text{for } E = 662 \text{ keV} \quad (3.8)$$

When reconstructed and scaled for the sampling distance, this will give the distribution of linear attenuation coefficients in the object.

The ACFs measured at 662 keV can be extrapolated to those that would have been measured at 511 keV using

$$\frac{I_o(511)}{I(511)} = \left[\frac{I_o(662)}{I(662)} \right]^{\frac{0.96}{0.87}} \quad (3.9)$$

Since only raising to a power by a constant is required to extrapolate the ACFs from energy 662 to 511 keV, this could be done in the sinogram without the need to reconstruct the data.

A singles transmission image of a phantom positioned at the center of the FOV is shown in figure 3.6(a) (page 57). Image was acquired with a 1 mCi point source of either ^{137}Cs or $^{68}\text{Ge}/^{68}\text{Ga}$ for more than 10 million counts per plane. The energy window for acquisition was 380-850 keV for $^{68}\text{Ge}/^{68}\text{Ga}$, and 450-950 keV for ^{137}Cs . Circular regions of interest of diameter 9 cm, 4 cm and 2 cm were placed in the parts of the phantom containing water, air and aluminum, respectively, and the mean values for the measured linear attenuation coefficient were recorded. Extrapolated values of linear attenuation coefficient were calculated according to equation (3.4) and the results are listed in table 3.3. Good agreement between the measured linear attenuation coefficients using ^{137}Cs and $^{68}\text{Ge}/^{68}\text{Ga}$ are observed, however, for water and aluminum the measured values are significantly lower than the theoretical values due to the fact that the contribution of scattered radiation has not been accounted for in these measurements.

Table 3.3. Linear attenuation coefficients measured using ^{68}Ge and ^{137}Cs in 'singles' mode without interplane septa.

Material	Linear attenuation coefficient (cm^{-1})		
	Measured		Theoretical
	^{68}Ge	^{137}Cs (extrapolated)	
Water	0.074 ± 0.005	0.071 ± 0.003	0.096
Aluminum	0.150 ± 0.008	0.144 ± 0.006	0.226
Air	0.011 ± 0.008	0.003 ± 0.004	0.000

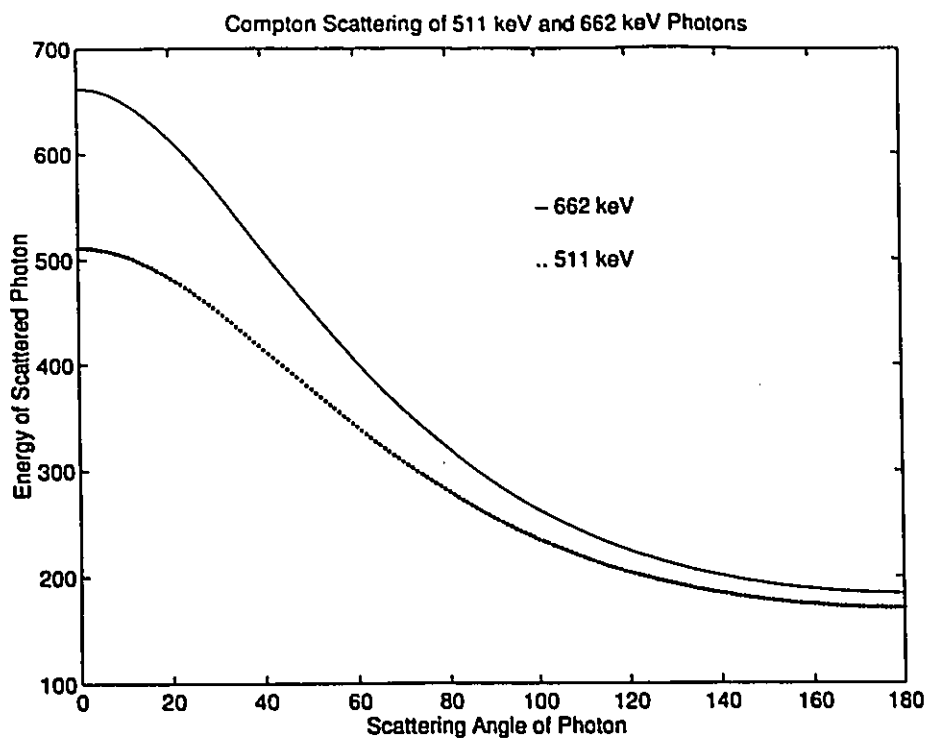


Figure 3.4 Energy of photons after scattering through a given angle.

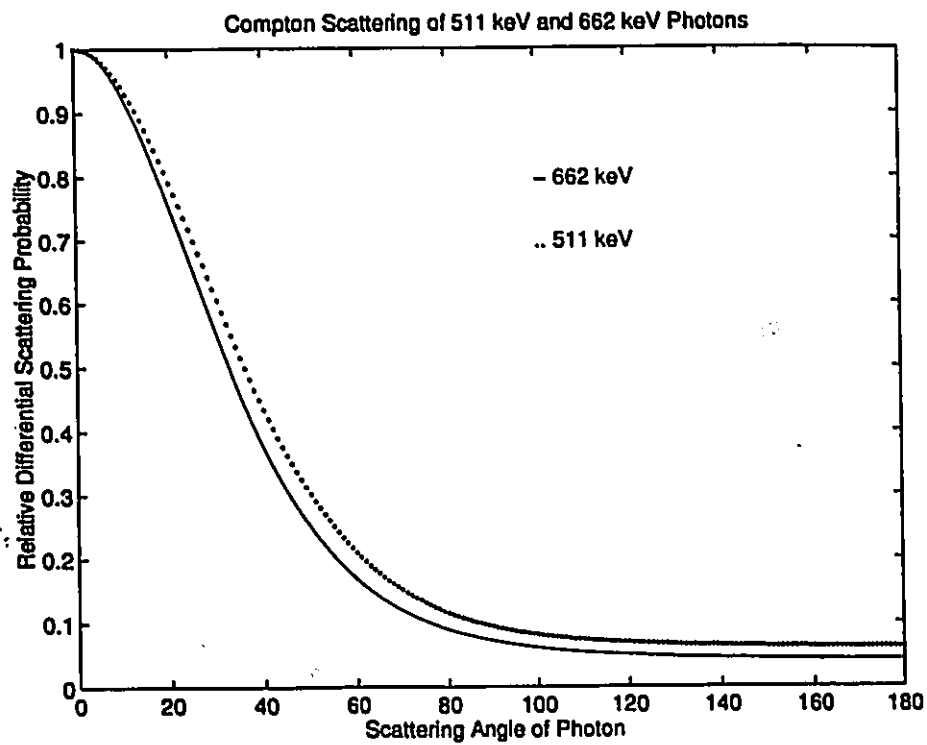


Figure 3.5 Relative differential scattering probability as a function of scattering angle.

3.5 SCATTER CORRECTION OF THE TRANSMISSION DATA

Scatter correction is necessary not only for emission data, but also for transmission data (Digby and Hoffman 1989). Scattered events are acquired inevitably along with the true events, and the energy of the scattered photon is governed by equation (1.1).

The rate of energy loss of the initial photon with respect to the scattering angle is inversely proportional to the initial photon energy. Suppose, for example, the photopeak window is set to include $\pm 25\%$ of the initial photon energy, so that the low energy discrimination level will be 380 keV for 511 keV photons and 490 keV for 662 keV photons. Photons scattered within 44° will be accepted for 662 keV photons compared to 50° for 511 keV photons (figure 3.4). The probability of scattering can be calculated using the Klein-Nishina equation (equation (1.2)). Figure 3.5 illustrates the variation of the relative scatter probability as a function of scattering angle for 662 keV and 511 keV photons. It shows that photons with higher energy are not only more forward scattered, but also less likely to scatter than lower-energy photons. The ratio of the integral from 0° to 44° for 662 keV to that from 0° to 50° for 511 keV gives 0.897. Thus, the scattering probability and the angle of scattering are both smaller for 662 keV than 511 keV photons when the width of the photopeak window is set to $\pm 25\%$ of the initial photon energy.

Dual-energy-window (DEW) scatter correction techniques (Grootoink *et al* 1992, Harrison *et al* 1992) have been developed to account for scattered events in the emission data. The DEW techniques cannot be applied unless dual-energy window data acquisition is completed, and the data acquired in the photopeak window and the scatter window must be stored in separate sinograms.

Unlike the case of the emission data, in which the scattered LOR should be considered, the DEW scatter technique is appropriate for the transmission data. With a simple modification, the DEW scatter correction can be applied on-the-fly during data acquisition. This is achieved by choosing the two energy windows such that the ratio of

the scatter events in the photopeak window to the sum of the true and scatter events in the scatter window is equal to unity. The true, unscattered, counts in LOR i , T_{pi} , can then be determined from the total counts in the photopeak window, M_{pi} , and in the scatter window, M_{si} , by:

$$T_{pi} = M_{pi} - M_{si} \quad (3.10)$$

In order to determine the energy windows that satisfy equation (3.10), energy spectra were measured experimentally by a series of blank and transmission scans obtained using a narrow energy window centered at a number of different energies. A 21 cm diameter cylindrical water phantom positioned at the center of the FOV was used for these measurements. Because the phantom is of known geometry and is uniformly filled with water, and assuming negligible scattering by air, the number of unscattered events in the photopeak window can be calculated from the blank scan data:

$$T_{pi} = B_{pi} e^{-\mu_w x_i} \quad (3.11)$$

where B_{pi} is the number of counts in LOR i of the blank scan measured in the photopeak window, x_i is the path length for LOR i through the phantom and μ_w is the linear attenuation coefficient for water.

The difference between the measured number of counts in the photopeak window for LOR i (M_{pi}) and this calculated value must represent the number of scattered events present in the photopeak window. The blank and transmission energy spectra are integrated between different lower and upper thresholds to find the photopeak and scatter energy windows that satisfy equation (3.10).

The two energy windows that satisfy equation (3.10) were found to be 260-450 keV and 450-950 keV for ^{137}Cs , and 230-380 keV and 380-850 keV for $^{68}\text{Ge}/^{68}\text{Ga}$.

A transmission image of a 21 cm cylindrical phantom with a 5 cm diameter cylindrical air insert and a 2.5 cm diameter cylindrical aluminum insert at the center of the FOV is shown in figure 3.6(a). The image obtained after scatter correction is shown in figure 3.6(b).

Regions of interest were placed in the center of the each object, and the mean values of the measured linear attenuation coefficient for each material were recorded. Extrapolated values for the linear attenuation coefficients were calculated according to equation (3.4). The results are listed in table 3.4.

Table 3.4. Linear attenuation coefficients measured using ^{68}Ge and ^{137}Cs in 'singles' mode without septa after scatter correction.

Material	Linear attenuation coefficient (cm^{-1})		
	Measured		Theoretical
	^{68}Ge	^{137}Cs (extrapolated)	
Water	0.095 ± 0.01	0.094 ± 0.01	0.096
Aluminum	0.22 ± 0.03	0.23 ± 0.03	0.226
Air	-0.01 ± 0.01	-0.02 ± 0.01	0.000

Using this modified version of DEW method, post-acquisition processing and extra storage memory space are no longer required.

3.6 DISCUSSION

Accurate attenuation correction is essential for quantitative positron tomography. With a new technique for measuring transmission data using single-photons, radioisotopes with more desirable features can be chosen for this measurement. ^{137}Cs is more economical

compared to $^{68}\text{Ge}/^{68}\text{Ga}$ in terms of the useful lifetime and cost. ^{137}Cs emits gamma rays, at 662 keV, which have a higher energy than the energy of the annihilation photons.

The sensitivity of the tomograph is expected to be lower for ^{137}Cs compared to $^{68}\text{Ge}/^{68}\text{Ga}$ due to lower probability of interaction of the higher-energy photons in the detectors. In addition, the probability of emission of a 662 keV photon from ^{137}Cs is 0.79, compared to 0.88 for the decay of ^{68}Ga through positron emission. This means that a ^{137}Cs source will have to be about 10 % stronger than a $^{68}\text{Ge}/^{68}\text{Ga}$ source to observe the same number of detected events.

Another disadvantage of using ^{137}Cs is a reduction in contrast between biological tissues. As an example, the mass attenuation coefficients of soft tissue are $9.6 \times 10^{-3} \text{ m}^2 \text{ kg}^{-1}$ at 511 keV and $8.7 \times 10^{-3} \text{ m}^2 \text{ kg}^{-1}$ at 662 keV; and the mass attenuation coefficients of cortical bone are $9.3 \times 10^{-3} \text{ m}^2 \text{ kg}^{-1}$ at 511 keV and $8.4 \times 10^{-3} \text{ m}^2 \text{ kg}^{-1}$ at 662 keV (Hubbell 1982). The typical densities of cortical bone and soft tissue are 2 kg m^{-3} and 1 kg m^{-3} ; using 662 keV instead of 511 keV photons results in an approximate 9% loss in contrast between bone and soft tissue. However, the ratio of mass attenuation coefficient of water to the mass attenuation coefficient of bone only deviates by 0.5 % from 662 keV to 511 keV (figure 3.3), so that extrapolation of linear attenuation coefficients is possible even with a change of contrast between tissues.

For PET imaging using multielement detectors, an important parameter is the ability to determine the crystals in which the incident photons have deposited their energy. Our measurements of the light output indicate that ^{137}Cs can be used for transmission measurements without any recalibration of the tomograph. Theoretically, 662 keV should provide a slightly better spatial resolution than 511 keV due to fewer and small-angle scattered photons. However, the effect is too small to be measured with our tomograph.

Transmission data obtained using photons with energies other 511 keV must be extrapolated to give values if they were measured with 511 keV photons. A simple

extrapolation method has been developed, and extrapolation can be performed in the sinogram.

The poor agreement between the measured and the theoretical values of linear attenuation coefficients (table 3.3) indicates the need to correct the measurements for scatter radiation. The DEW technique was used for scatter correction in this study. When corrected for scatter, the measured linear attenuation coefficients for water and aluminum compare well with typical values. The measured negative values of linear attenuation coefficient for air indicate an overcorrection for scatter events (table 3.4). By selecting judiciously the two energy windows, correction can be made on-the-fly during dual energy data acquisition.

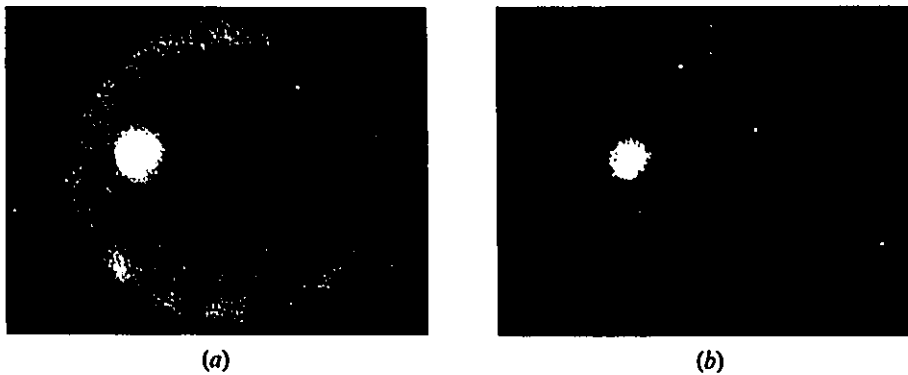


Figure 3.6 Transmission images of a 21 cm water cylinder containing a 2.5 cm aluminium insert and a 5 cm air insert without scatter correction (a) and after scatter correction (b).

REFERENCES

Bailey DL, Hutton BF, and Walker PJ (1987). Improved SPECT using simultaneous emission and transmission tomography. *J. Nucl. Med.* 28:844-851.

- Barney SJ, Harrop R, and Atkins MS (1994). Addition of noise by scatter correction methods in PVI. *IEEE Trans. Nucl. Sci.* 41:1551-1555.
- Berger MJ and Seltzer SM (1983). *Stopping Powers and Ranges of Electrons and Positrons 2nd edn.* Washington, DC: National Bureau of Standards.
- deKemp R and Nahmias C (1994). Attenuation correction in PET using single-photon transmission measurement. *Med. Phys.* 21:771-778.
- Digby WM and Hoffman EJ (1989). An investigation of scatter in attenuation correction for PET. *IEEE Trans. Nucl. Sci.* 36:1038-1042.
- Evans RD (1955). *The Atomic Nucleus.* New York: McGraw-Hill.
- Grootenk S, Spinks TJ, Jones T, Michel C, and Bol A (1992). Correction for scatter using a Dual-Energy-Window technique with a tomography operated without septa. *IEEE 1991 Medical Imaging Conf. Rec. (Santa Fe, NM, 1991)* New York:IEEE 1569-1573.
- Harrison RL, Haynor DR, and Lewellen TK (1992). Dual energy window scatter corrections for positron emission tomography *IEEE 1991 Medical imaging Conf. Rec. (Santa Fe, NM, 1991)* New York:IEEE 1700-1704.
- Hubbell JH (1982). Photon mass attenuation and energy-absorption coefficients from 1 keV to 20 MeV. *Int. J. Appl. Radiat. Isot.* 33:1269-1290.
- Knoll GF (1979). *Radiation Detection and Measurements.* New York: JohnWiley & Sons.
- Kuhl DE, Hale J, and Eaton WL (1966). Transmission scanning: a useful adjunct to conventional emission scanning for accurately keying isotope deposition to radiographic anatomy. *Radiology* 87:278-284.
- Lederer CM, Hollander JM and Perlman I (1968). *Table of Isotopes 6th edn.* New York: Wiley.

- Ijungberg M and Strand SE (1990). Attenuation correction in SPECT based on transmission studies and Monte Carlo simulations of build-up functions. *J. Nucl. Med.* 31:493-500.
- Tan P, Bailey DL and Meikle SR, Eberl S, Fulton RR, and Hutton BF (1993). A scanning line source for simultaneous emission and transmission measurements in SPECT. *J. Nucl. Med.* 34:1752-1760.
- Yu SK and Nahmias C (1995). Single-photon transmission measurements in positron tomography using ^{137}Cs . *Phys. Med. Biol.* 40:1255-1266.

CHAPTER 4

SEGMENTED ATTENUATION CORRECTION USING ARTIFICIAL NEURAL NETWORKS IN PET

The measured attenuation correction technique is widely used in cardiac positron tomographic studies. However, the success of this technique is limited because of insufficient counting statistics achievable in practical transmission scan times, and because of the scattered radiation in the transmission measurements which leads to an underestimation of the attenuation coefficients. To overcome these problems, a segmented attenuation correction technique is developed that uses artificial neural networks. The technique is validated in phantoms and verified in human studies. The results indicate that attenuation coefficients measured in the segmented transmission image are accurate and reproducible. Activity concentrations measured in the reconstructed emission image can also be recovered accurately using this new technique. The accuracy of the technique is subject independent and insensitive to scatter contamination in the transmission data. This technique has the potential of reducing the transmission scan time, and satisfactory results are obtained if the transmission data contains about 400,000 true counts per plane. Moreover, it can predict accurately the value of any attenuation coefficient in the range from air to water in a transmission image with or without scatter correction (Yu and Nahmias 1996).

4.1 INTRODUCTION

Despite its shortcomings, the measured attenuation method is generally accepted for attenuation correction in cardiac PET studies. However, the method will be more successful if one can reduce the noise in the transmission data. Moreover, there is a need to shorten the transmission scan time due to the concern of patient discomfort, and the probability of errors in the ACFs due to patient motion (Huang *et al* 1979, McCord *et al* 1992, Bettinardi *et al* 1993, Bacharach *et al* 1993).

As mentioned in chapter 2, methods have been suggested for reducing the noise in the measured transmission data. Among these methods, only the single-transmission measurement method (deKemp and Nahmias 1994) and the segmented attenuation correction (SAC) techniques (Huang *et al* 1981, Xu *et al* 1991, Meikle *et al* 1993, Xu *et al* 1994, and Karp *et al* 1995) can greatly reduce both the transmission scan time and the statistical noise in the transmission data. However, to provide accurate attenuation data these techniques must be incorporated with a scatter correction technique and account for the noise introduced by scattered radiation. There are also problems with the existing SAC techniques, as discussed in chapter 2.

In this section, a new approach to SAC is developed that uses artificial neural networks (ANN). Instead of classifying pixels based on the original pixel intensity histogram, a local matrix of 7x7 pixels centered around the pixel being considered is used. In this way, information from the neighboring pixels is used for segmentation. A new pixel value is then obtained from a calibration curve that relates the theoretical linear attenuation coefficients to the probability that the pixel belongs to the 'soft tissue' class. The technique is verified for reproducibility, and for subject independence in recovering appropriate attenuation coefficients in both phantom and human studies. The effect of scatter in the transmission data on the segmented data, and the capability of recovering activity concentrations in emission studies are also investigated. Finally, the new SAC

technique is applied to cardiac studies in human subjects, and the results are compared with those obtained by using the conventional measured attenuation correction method.

4.2 TRANSMISSION MEASUREMENTS

In this work, the phantom and human studies were performed on an ECAT 953/31 positron tomograph. The scanner is equipped with a rotating rod source which contained approximately 0.5 mCi of $^{68}\text{Ge}/^{68}\text{Ga}$ at the time the studies were performed. Although the scanner has been modified to allow single-transmission measurements and interplane septa have been removed for 3D volume imaging, the studies were done using coincidence counting in 2D mode without septa. Transmission and blank scans were acquired with an energy window of 350-850 keV and the acquired data were processed by sinogram smoothing (Palmer *et al* 1986, Dahlbom *et al* 1987, Ostertag *et al* 1989). Images were reconstructed into 128x128 matrices using a Hann windowed ramp filter, with roll-off at 80 percent of the Nyquist frequency. Transmission images were reconstructed after taking the natural logarithm of the ratio of blank to transmission data. The pixel values in these matrices were read directly as linear attenuation coefficients (μ) in units of cm^{-1} .

Because each of the reconstructed planes in the ECAT 953/31 overlaps the adjacent planes by 50 %, a 3D median filter was applied to improve the signal-to-noise ratio in the transmission images. This filter has the property that it achieves some degree of noise suppression while maintaining resolution across boundaries (Gonzalez and Wintz 1987). For each image, a new pixel value was assigned as the median value of a surrounding 5x5 in-plane and 5x5 adjacent planes neighborhood. The purpose of this step is to prepare a less noisy image that incorporates information from adjacent planes as input to the ANN.

To acquire data for training the ANN, transmission scans of the chest of a human volunteer were acquired for 5 minutes and 3 hours, while a blank scan was acquired on the same day for 12 hours. The 3 hour transmission images were segmented into 3 classes (air, lung and soft tissue) using an optimal thresholding algorithm (Reddi *et al* 1984). In the training process, the desired outputs of the artificial neural network for each pixel were assigned based on the classification of the pixel in the 3 hour segmented image, while the 5 minute transmission images were used as training data.

4.3 ARTIFICIAL NEURAL NETWORK (ANN)

As shown in figure 4.1, the proposed ANN consists of two parts, principal components analysis (PCA) and backpropagation multilayer perceptrons (MLP). The PCA serves as a preprocessor to the MLP. The PCA technique used in this study is the generalized Hebbian algorithm (GHA) (Haykin 1994). The GHA is a self-organizing system composed of an input layer and an output layer. The nodes in the input layer are interconnected to all the nodes in the output layer. Each interconnection weights the data values sent across it. The output of the GHA is computed as,

$$y_j(n) = \sum_{i=0}^{p-1} w_{ji}(n)x_i(n) \quad (4.1)$$

where $y_j(n)$ is the output of node j in the output layer for the n th pattern; $w_{ji}(n)$ is the interconnection weight between input node i and output node j ; $x_i(n)$ is the input of node i in the input layer; p is the number of input node. There are 49 input nodes to the GHA in which pixel values of a local area of the image are being processed (i.e. a matrix of 7x7 pixels in which the pixel being considered is located at the center of the matrix). Since the

measured attenuation coefficient of an object varies with factors such as scattered events in the transmission data; and for the purpose of limiting the outputs of the GHA to a range of some finite values, the pixel values in the transmission image being processed were normalized to a range from 0 to 10 before data were fed to the GHA.

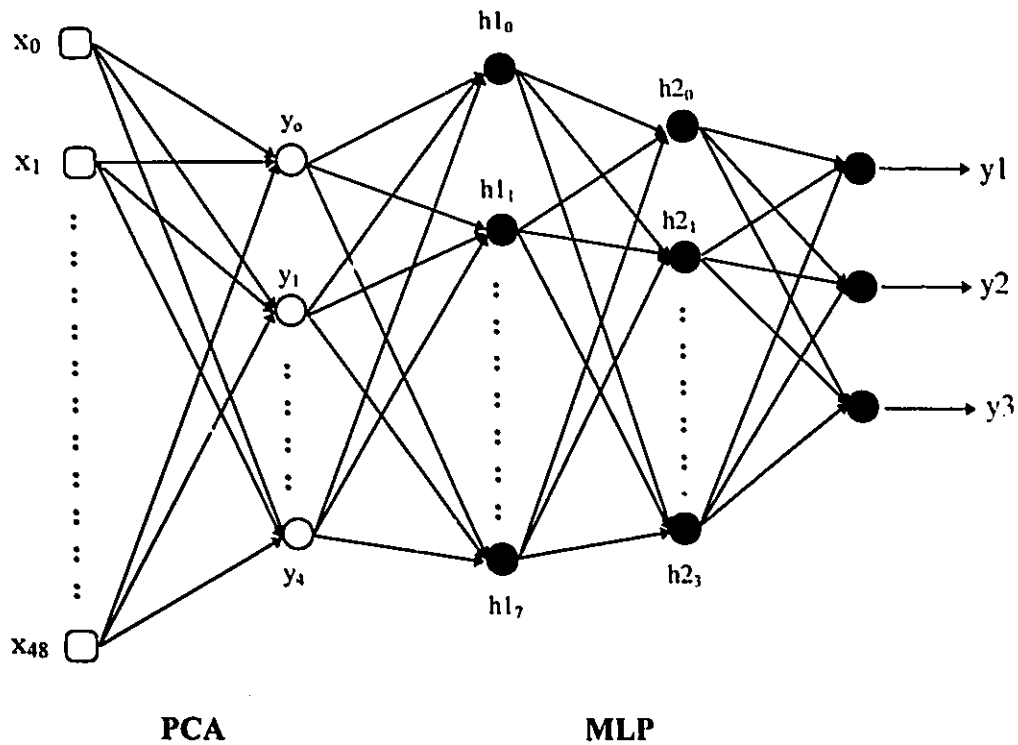


Figure 4.1 The basic structure of the ANN. The PCA has 49 inputs (x_0 to x_{48}) and 5 outputs (y_0 to y_4). The MLP has two hidden layers, one with 8 nodes ($h1_0$ to $h1_7$), the other with 4 nodes ($h2_0$ to $h2_3$). The outputs of the MLP ($y1, y2$ and $y3$) are the conditional probabilities that the central input pixel (x_{34}) belongs to the class 'air', 'lung' or 'soft tissue'.

During the training process, the interconnection weights are updated as follows,

$$\Delta w_{ji}(n) = \eta \left[y_j(n)x_i(n) - y_j(n) \sum_{k=0}^l w_{kj}(n)y_k(n) \right] \quad (4.2)$$

where $\Delta w_{ji}(n)$ is the adjustment applied to interconnection weight w_{ji} of output node j connected to input node i for the n th training pattern; η is the learning rate. Using the training image, the PCA was trained iteratively until the interconnection weights reached their steady-state values. Features with small variances were then discarded and only those features with large variances were retained. As a result, the output of the PCA contains only 5 features which represents effectively the 49 input data.

The output from the PCA is then used as the input to the MLP. The purpose of the MLP is to classify the features in the transmission image into three tissue types : air, lung or soft tissue. The input layer of the MLP distributes the output from the PCA, through interconnections, to all the nodes in the first hidden layer. Each interconnection weights the data values sent across it. The weights associated with the interconnections are the parameters adjusted during training and consequently, represent the knowledge possessed by the ANN. Each node in the ANN sums the values received from the interconnections and generate an output via an activation function. The activation function is employed so that the output of the node is limited to a permissible amplitude range. In order to avoid saturating the activation function, the outputs from the PCA for all the input patterns were grouped together and normalized to a range from 0 to 10 before feeding to the MLP. During the training process, the error in the segmentation is calculated for each node in the output layer by subtracting the actual output from the desired output. This output difference is backpropagated through the network to make interconnection weight adjustments that will minimize the network error. The backpropagation training algorithm adjusts the interconnection weight values according to the generalized delta rule (Haykin 1994),

$$\Delta W_{ji}(n) = \alpha \Delta W_{ji}(n-1) + \lambda \delta_j(n) Y_i(n) \quad (4.3)$$

where $\Delta W_{ji}(n)$ is the adjustment applied to interconnection weight W_{ji} of node j connected to node i for the n th training pattern; α is the momentum constant; λ is the learning rate;

Y_j is the input of node j ; δ_j is the local gradient of node j . When node j is an output node, δ_j is equal to the product of the activation function derivative and the difference between the desired output and the actual output. If node j is a hidden node, δ_j is equal to the product of the activation function derivative and the sum of the product of each local gradient and the corresponding interconnection weight in the succeeding layer.

The adjustment of the interconnection weights minimizes the error between the desired output and the actual output. The learning rate governs the magnitude of each adjustment. The momentum constant helps accelerate the rate of learning and also stabilizes the ANN. As shown in equation (4.3), when ΔW_{ji} has the same algebraic sign on two consecutive patterns, ΔW_{ji} is increased by a large amount. On the contrary, ΔW_{ji} decreases in magnitude when $\Delta W_{ji}(n)$ and $\Delta W_{ji}(n-1)$ have opposite algebraic signs.

During the training process, the learning rates and the momentum constants were updated according to the search-then-converge schedule (Darken and Moody 1992) defined by

$$\lambda(n) = \frac{\lambda_o}{1 + (n / \tau_\eta)} \quad \text{and} \quad \alpha(n) = \frac{\alpha_o}{1 + (n / \tau_\alpha)} \quad (4.4)$$

where λ_o , α_o , τ_α and τ_η are constants. The idea is to decrease the initial learning rate, λ_o , and the initial momentum constant, α_o , as the ANN is learning more and more about the feature of the patterns. It helps to stabilize the ANN as the weights are converging to their optimum values. To evaluate the performance of the network during training, the mean square error, MSE, is calculated as

$$MSE = \frac{\sum_{n=1}^N \left(\sum_{j=1}^p D_j(n) - Y_j(n) \right)^2}{N} \quad (4.5)$$

where p is the number of nodes in the output layer (i.e. $p=3$); N is the total number of patterns in a training image (i.e. $N = \text{total number of pixels being segmented}$); $D_j(n)$ and $Y_j(n)$ are the desired and actual outputs of node j for the n th input pattern. Patterns of the training image are shuffled for the next iteration until the mean square error converged to a stable minimum value. In general, the optimal selection of the parameters such as learning rate and momentum constant are those which yield convergence of the MSE to a minimum value with the least number of iterations in training. Following this strategy, the parameters are selected such that the MSE converges to a stable value less than 0.05 in 50 iterations. As illustrated in figure 4.2, the MSE converges to a value of less than 0.035 within 20 iterations using the final selected parameters.

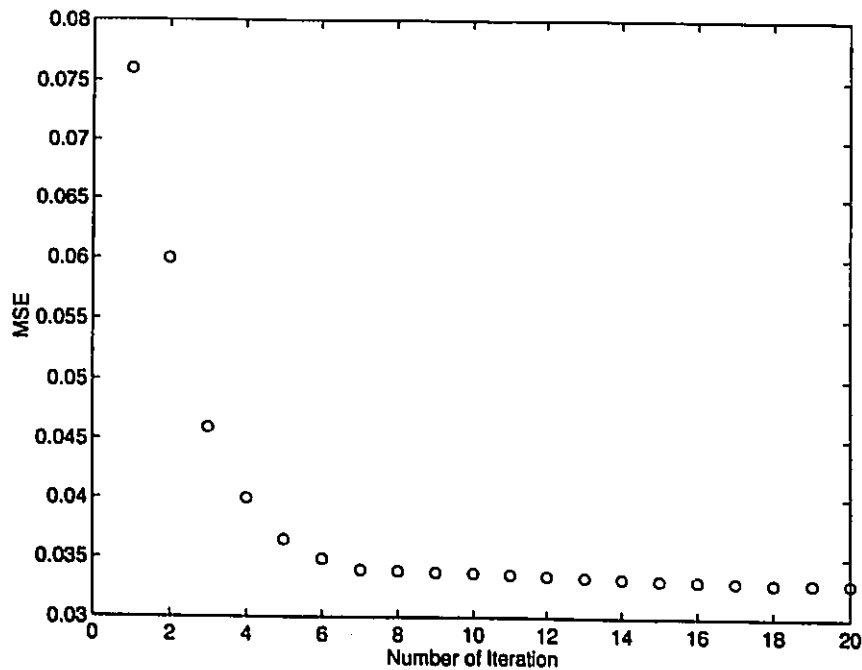


Figure 4.2 The rate of learning of the MLP portion of the ANN during the training process.

Since a neural network with minimum size may generalize better to new data and consume less time, the MLP was built based on the cascade-correlation learning

architecture (Fahlman and Lebiere 1990). The network begins with the designed input and output nodes, and 2 hidden layers (5 nodes in the first hidden layer and 3 nodes in the second hidden layer). Hidden nodes are added one by one to the network until the MSE converges to a value less than 0.05. The final structure of the MLP contains 5 nodes in the input layer, 8 nodes in the first hidden layer, 4 nodes in the second hidden layer, 3 nodes in the output layer, and they are fully connected.

In general, a MLP trained with the back-propagation algorithm may learn faster when the activation function built into the model of the nodes of the network is asymmetric. Therefore, a hyperbolic tangent function, which limits the range of the output of the node to -1.716 to 1.716, is used in the model of all hidden nodes.

$$Y_j = 1.716 \tanh\left(\frac{2v_j}{3}\right) \quad (4.6)$$

However, a sigmoid function, which gives a desirable range from 0 to 1, is used in the model of all the output nodes.

$$Y_j = \frac{1}{1 + e^{-v_j}} \quad (4.7)$$

and

$$v_j = \sum_{k=1}^m W_{jk} x_k - \theta_k \quad (4.8)$$

where Y_j is the output of node j ; W_{jk} is the interconnection weights between node j and node k in the preceding layer; θ_k is the threshold which governs the net input to the activation function (v_j); x_k is the input to node j from the output from node k .

The desired outputs of the MLP were assigned to be 0.85 for the correct tissue type, and 0.15 for the other two outputs. These values were chosen to avoid saturating the network during training. After training is completed, the output nodes provide the conditional probability for classification $P(\text{soft tissue}|x)$, $P(\text{lung}|x)$ and $P(\text{air}|x)$ given an input data vector x (i.e the 7x7 neighboring pixels).

4.4 MAPPING OUTPUTS FROM ANN TO NEW ATTENUATION COEFFICIENT

Since the outputs from the ANN are just the conditional probabilities of the pixel belonging to the three specific tissue types, it is dangerous to assume that the appropriate linear attenuation coefficient is simply the sum of the theoretical attenuation coefficients weighted by the conditional probabilities. Thus, calibration is required to map these outputs to their corresponding theoretical attenuation coefficients.

In the calibration procedure, a 3 hour transmission scan of a 20 cm water phantom containing an empty bottle (4.5 cm in diameter) and four blocks of different woods (3.5cm x 7 cm in cross section) was performed. A modified dual-energy-window technique (Yu and Nahmias 1995) was applied before segmentation to correct for scattered events. The chemical compositions of the woods, their density and theoretical attenuation coefficient at 511 keV are listed in table 4.1 (Webber 1981).

Table 4.1 Weight fractions, density and the theoretical attenuation coefficients at 511 keV of 4 different kinds of wood (from Webber 1981).

Woods	Weight Fractions			Density (g/cm ³)	Theoretical μ at 511 keV (cm ⁻¹)
	Carbon	Hydrogen	Oxygen		
Balsa	0.4681	0.0601	0.4718	0.116	0.0106
Light Pine	0.4868	0.0672	0.4460	0.374	0.0345
Pine	0.4868	0.0672	0.4460	0.475	0.0438
Maple	0.4735	0.0679	0.4586	0.783	0.0722

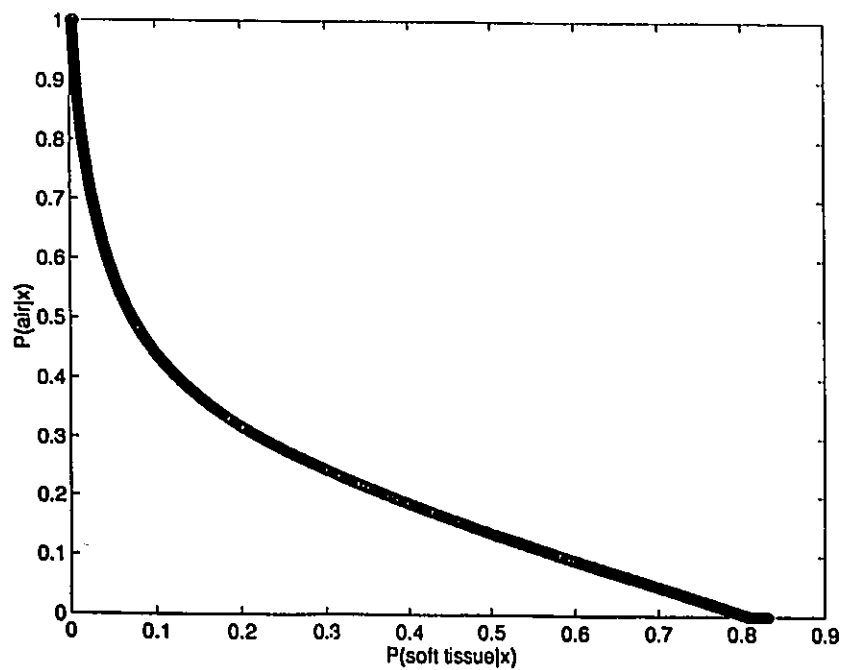


Figure 4.3 Plot of $P(\text{soft tissue}|x)$ against $P(\text{air}|x)$.

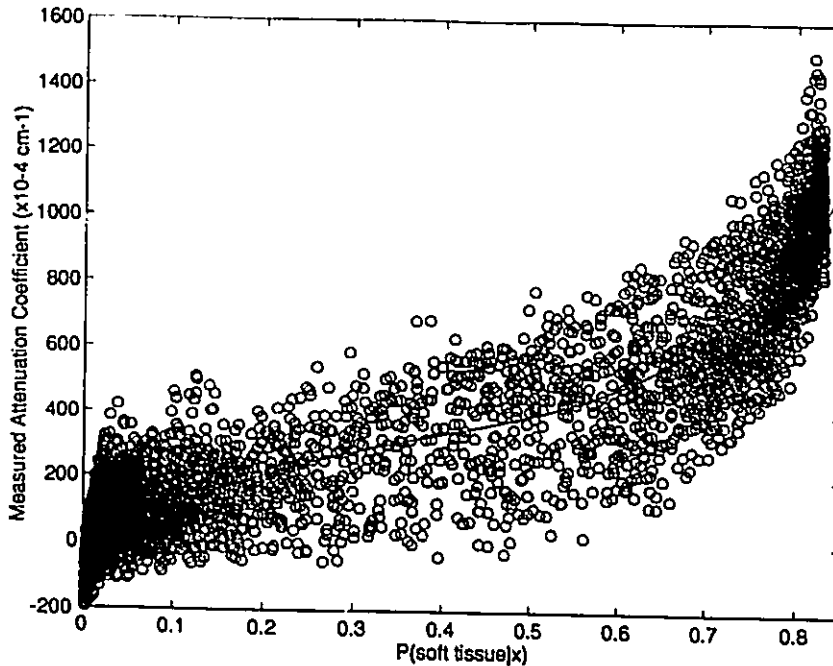


Figure 4.4 Calibration curve for mapping $P(\text{soft tissue}|\mathbf{x})$ to attenuation coefficients at 511 keV.

Calibration was done by mapping $P(\text{soft tissue}|\mathbf{x})$ to the measured attenuation coefficient pixel-by-pixel in the transmission image, since the sum of $P(\text{lung}|\mathbf{x})$, $P(\text{soft tissue}|\mathbf{x})$ and $P(\text{air}|\mathbf{x})$ is equal to unity, and $P(\text{soft tissue}|\mathbf{x})$ and $P(\text{air}|\mathbf{x})$ is a one-to-one function as illustrated in figure 4.3. A plot of this mapping is shown in figure 4.4, and a calibration curve is obtained by fitting the data using a 4th order polynomial function. Using the calibration curve, a continuous range of new pixel values can be assigned to the transmission image. Once the image is processed, the ACF for each LOR can then be calculated directly by taking the exponential of the forward projected transmission data.

4.5 VERIFICATION OF THE CALIBRATION

In order to verify the accuracy of the calibration, as well as the effect of scatter on the segmented attenuation coefficients, transmission measurements were made of a 20 cm water phantom containing either an air insert (5 cm in diameter) or a block of wood (3.5 cm x 7 cm in cross section). A number of blocks of wood with different attenuation properties were used. Transmission images were reconstructed with and without applying the dual energy scatter correction technique. For further assessment of the sensitivity of scatter to the new SAC technique, another set of transmission measurements were performed on each individual block of wood in air. A cylindrical container of water (7 cm in diameter) was also placed in the field of view at least 15 cm away from the block of wood, during the measurements. No scatter correction was applied to the transmission data, and all the reconstructed transmission images were segmented using the new SAC technique. The average μ for each insert was obtained from a region of interest half the size of the insert in extent and located at the center of the insert.

As shown in table 4.2, the segmented attenuation coefficients agree with their theoretical values except for a slight overestimation for air and balsa wood. Moreover, the segmented μ only deviate slightly between segmented transmission images with and without scatter correction, and similar values of segmented μ were also observed for the transmission measurements on the individual blocks of wood and the bottle of water in air without scatter medium. This implies that the output of the ANN is insensitive to the contamination of scattered radiation, and that this attenuation correction technique is capable of providing accurate attenuation coefficients without the need for scatter correction of the transmission measurements. Furthermore, the same calibration curve was used to estimate the attenuation coefficient of acetone and hexane, and good agreement between the estimated and theoretical values was found (table 4.4, page 75).

Table 4.2 Attenuation coefficients obtained from the ANN technique with and without scatter correction of the transmission data.

Material	[scatter corrected] Segmented μ (cm^{-1})	[no scatter correction] Segmented μ (cm^{-1})	[no scatter correction, no scatter medium] Segmented μ (cm^{-1})	Theoretical μ (cm^{-1})
Air	0.008 ± 0.004	0.008 ± 0.005		0.000
Balsa	0.018 ± 0.005	0.015 ± 0.004	0.009 ± 0.003	0.011
Light Pine	0.036 ± 0.003	0.033 ± 0.002	0.032 ± 0.003	0.035
Pine	0.048 ± 0.004	0.043 ± 0.003	0.041 ± 0.003	0.044
Maple	0.072 ± 0.003	0.070 ± 0.002	0.070 ± 0.003	0.072
Water	0.094 ± 0.002	0.094 ± 0.002	0.096 ± 0.003	0.096

4.6 VERIFICATION OF THE ANN TECHNIQUE

4.6.1 Counting Statistics Requirement and Subject Dependence of the ANN Technique

It should be evident that improvements in the quality of the transmission image will lead to more accurate segmentation. However, there must be a minimum counting statistics or transmission scanning time required in order to give reasonably good segmentation results. To this end, transmission scans were performed on 7 healthy human volunteers with acquisition times ranging from 5 minutes to 30 minutes. Transmission images were all segmented using the new SAC technique. The segmented transmission images of the 7 human volunteers were also classified into three tissue types - air, lung or soft tissue,

using an optimal thresholding algorithm (Reddi *et al* 1984). Average values for the segmented attenuation coefficient of each tissue type for each volunteer's transmission image, standard deviation of the segmented μ within subjects and standard deviation of average segmented μ between subjects were calculated.

Segmented images from low counting statistics transmission data were compared to their corresponding segmented images from the 30 minute transmission data for the seven healthy volunteers. Plots of the correlation constant and the average absolute error against the number of true counts in the transmission image are given in figures 4.5 and 4.6. For all subjects, the graphs show that better correlation and less error are obtained for higher counting statistics, and both the correlation constant and absolute error reach a plateau when the transmission image contains about 400,000 true counts per plane. As shown in table 4.3, the variation between subjects is about 4 times less than the variation within the subjects. Hence, the performance of the segmentation technique is not subject dependent, and correlation ($r \cong 0.99$) and average error in segmented attenuation coefficient (0.0025 cm^{-1}) are expected for a transmission image with 400,000 true counts. Good segmentation for all image planes requires approximately 12 million true counts, or 5 minutes acquisition time with a 2 mCi rotating rod source for the ECAT 953/31 PET scanner without septa. However, the technique also works reasonably well for transmission data with less counting statistics.

Table 4.3 Variation of segmented attenuation coefficient between and within subjects.

Variation of segmented attenuation coefficient	Air	Lung	Soft Tissue
Between Subjects	37.5 %	7.7 %	3.9 %
Within Subjects	120.8 %	28.8 %	11.4 %

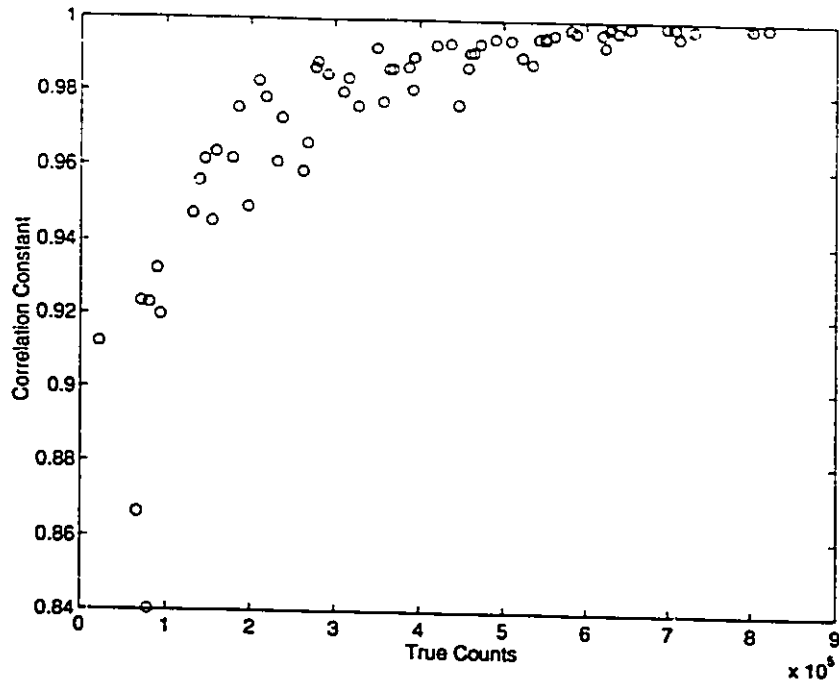


Figure 4.5 Correlation constant as a function of true counts in the transmission images, each image is correlated with the one containing most counts.

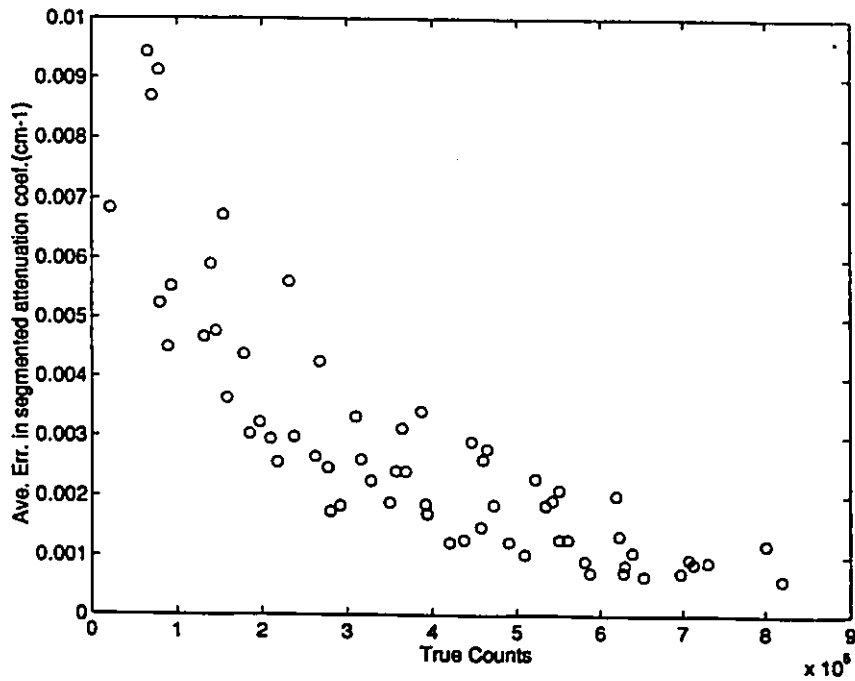
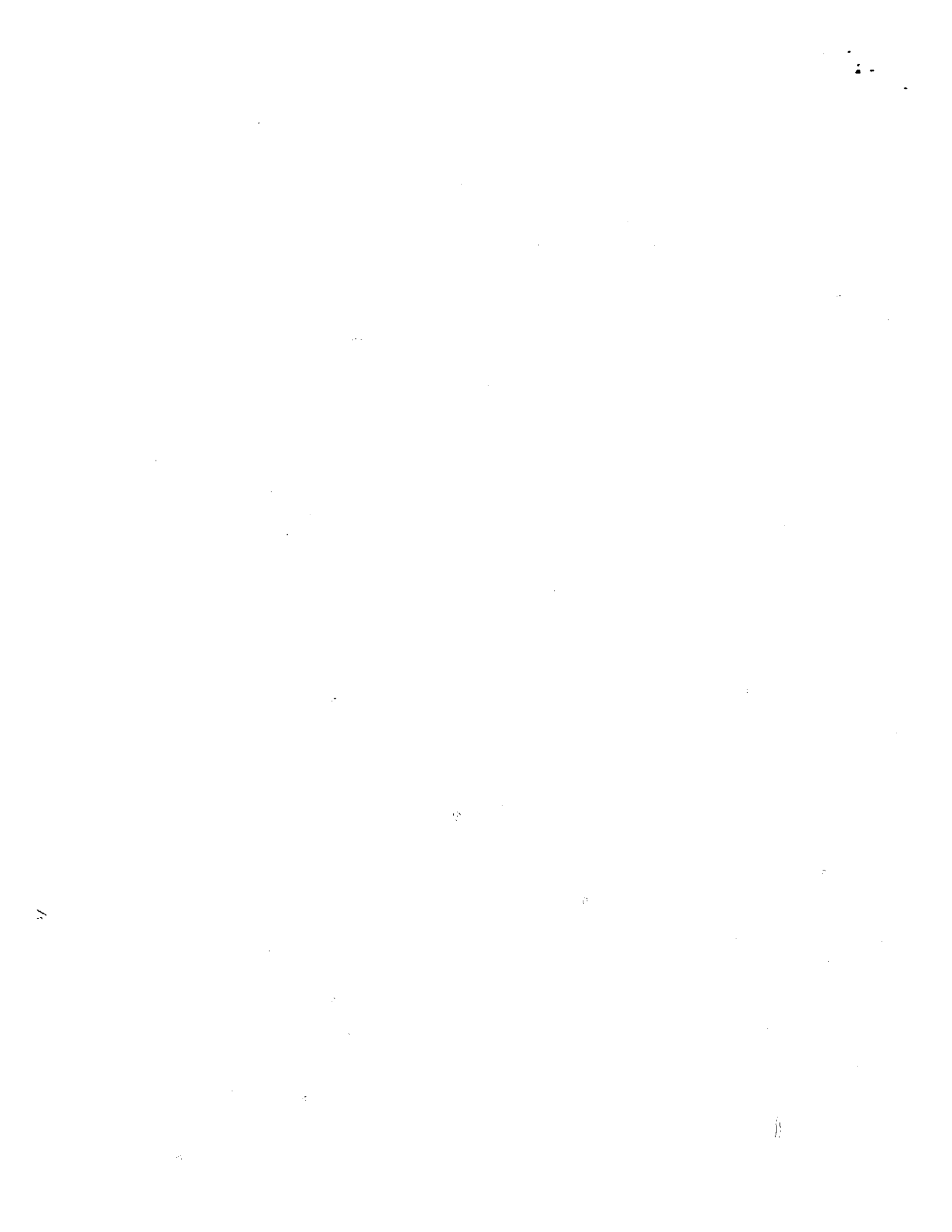


Figure 4.6 Average absolute error as a function of true counts in the transmission images.



4.6.2 Reproducibility of the ANN Technique

To test the reproducibility of the technique, 8 sets of transmission measurements of a phantom containing three 5 cm diameter cylindrical inserts of different attenuating materials were obtained. The insert materials were water, acetone and hexane, and their theoretical attenuation coefficients are 0.096 cm^{-1} , 0.072 cm^{-1} and 0.066 cm^{-1} respectively. In each set, two transmission measurements of the same phantom were acquired, one for 10 minutes and one for 3 hours.

Figure 4.7 shows the attenuation coefficients measured from the segmented transmission images for the 8 trials of transmission measurements of the phantom containing cylindrical inserts of water, hexane and acetone. Table 4.4 shows the average segmented attenuation coefficients over the 8 trials of the transmission measurements and their corresponding standard deviation between trials. The largest deviation between trials is about 3 % from the 10 min. segmented transmission image in the hexane region. Again, good agreement between the average segmented attenuation coefficients and the theoretical values was observed.

Table 4.4 Average segmented attenuation coefficients over 8 trials and their standard deviation between trials. Theoretical attenuation coefficients are also given for comparison to the average segmented μ .

Materials	[10 min.] Segmented μ (cm^{-1})	[3 hours] Segmented μ (cm^{-1})	Theoretical μ (cm^{-1})
Hexane	0.066 ± 0.002	0.066 ± 0.001	0.066
Acetone	0.071 ± 0.002	0.072 ± 0.001	0.072
Water	0.095 ± 0.001	0.096 ± 0.001	0.096

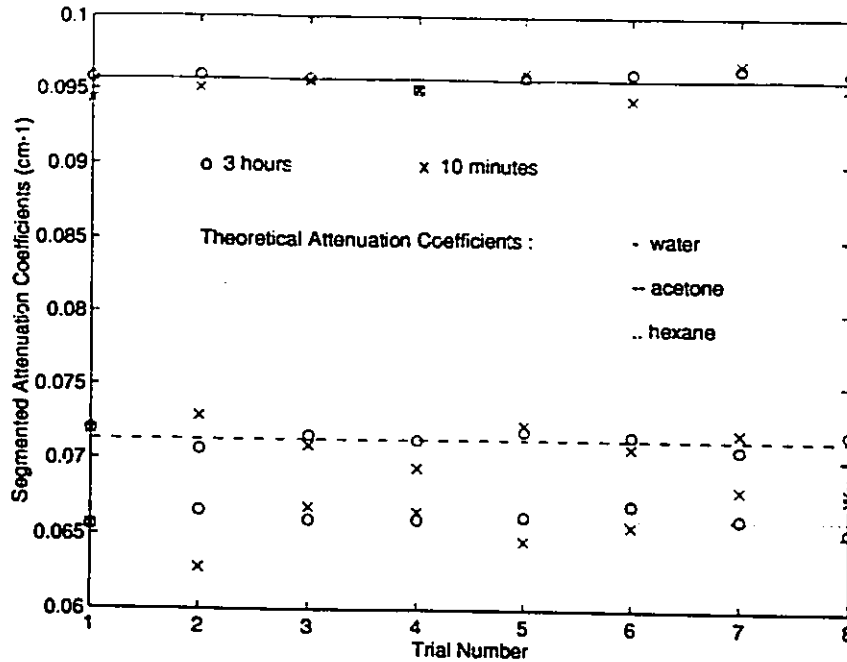


Figure 4.7 The segmented attenuation coefficients for 8 trials of transmission measurements of a phantom containing hexane, acetone and water.

4.6.3 Recovery of Activity Concentrations in Emission Measurements

For further verification of the technique, experiments were performed using a 20 cm water phantom containing 5 cm in diameter cylindrical inserts of different attenuating materials. The insert materials were methanol, hexane and water, and their theoretical attenuation coefficient are 0.079 cm^{-1} , 0.066 cm^{-1} and 0.096 cm^{-1} respectively. The activity concentrations were $0.012 \text{ } \mu\text{Ci/ml}$ in the water phantom, $0.088 \text{ } \mu\text{Ci/ml}$ in the methanol insert, $0.000 \text{ } \mu\text{Ci/ml}$ in the hexane insert, and $0.100 \text{ } \mu\text{Ci/ml}$ in the water insert. Emission measurement was acquired for one hour, and two transmission measurements were performed 12 hours later for 10 million and 60 million measured true counts,

respectively. Emission data were corrected for scatter and reconstructed with either no attenuation correction, measured attenuation correction or the new SAC.

As shown in table 4.5, the new SAC technique has superior performance in recovering activity concentrations in the emission measurement than the measured attenuation correction method.

Table 4.5 Recovered activity concentrations in emission measurements for no, measured and segmented attenuation correction with 10 and 60 million measured counts in transmission measurement compared to the actual activity concentrations in each insert.

Region	No ($\mu\text{Ci/ml}$)	Measured [10 M] ($\mu\text{Ci/ml}$)	Measured [60 M] ($\mu\text{Ci/ml}$)	Segmented [10 M] ($\mu\text{Ci/ml}$)	Segmented [60 M] ($\mu\text{Ci/ml}$)	Actual Activity Conc. ($\mu\text{Ci/ml}$)
Water Insert	0.019 \pm 0.003	0.081 \pm 0.007	0.082 \pm 0.006	0.095 \pm 0.006	0.104 \pm 0.006	0.100
Methanol Insert	0.016 \pm 0.002	0.062 \pm 0.007	0.068 \pm 0.004	0.080 \pm 0.005	0.092 \pm 0.005	0.088
Hexane Insert	0.0023 \pm 0.0009	0.008 \pm 0.004	0.005 \pm 0.002	0.008 \pm 0.003	0.006 \pm 0.003	0.000
Water Phantom	0.0011 \pm 0.0007	0.007 \pm 0.006	0.008 \pm 0.004	0.010 \pm 0.004	0.012 \pm 0.004	0.012

4.6.4 Human Studies

Seven patients undergoing routine viability assessment for ischaemic heart disease had a 5 minute and a 25 minute transmission measurement instead of the routine 30 minute one. Regional myocardial blood flow and metabolism were measured using ^{13}N -ammonia and ^{18}F -fluorodeoxyglucose (^{18}FDG) as described elsewhere (Fallen *et al* 1995). The ^{13}N -ammonia and ^{18}FDG emission data were corrected for attenuation using the 25 minute measured transmission data, the 5 minute or the 25 minute segmented transmission data.

All emission images were then reconstructed into a 128x128 matrices using a Hann filter with roll-off at 60% of the Nyquist frequency.

The results from a patient study are shown in figure 4.8, and results from all the patient studies can be found in appendix A. The first row shows the transmission images reconstructed from the 25 minute transmission scan, the segmented 5 minute transmission image and the segmented 25 minute transmission image. The second and the third rows show the reconstructed ^{18}F FDG and ^{13}N -ammonia images respectively, reconstructed with the corresponding attenuation data in the first row. There is no noticeable difference in image quality between the images using 5 minute segmented attenuation data and those using 25 minute segmented attenuation data. However, both segmented transmission images and their corresponding emission images are of better quality than the measured transmission images and its corresponding emission images.

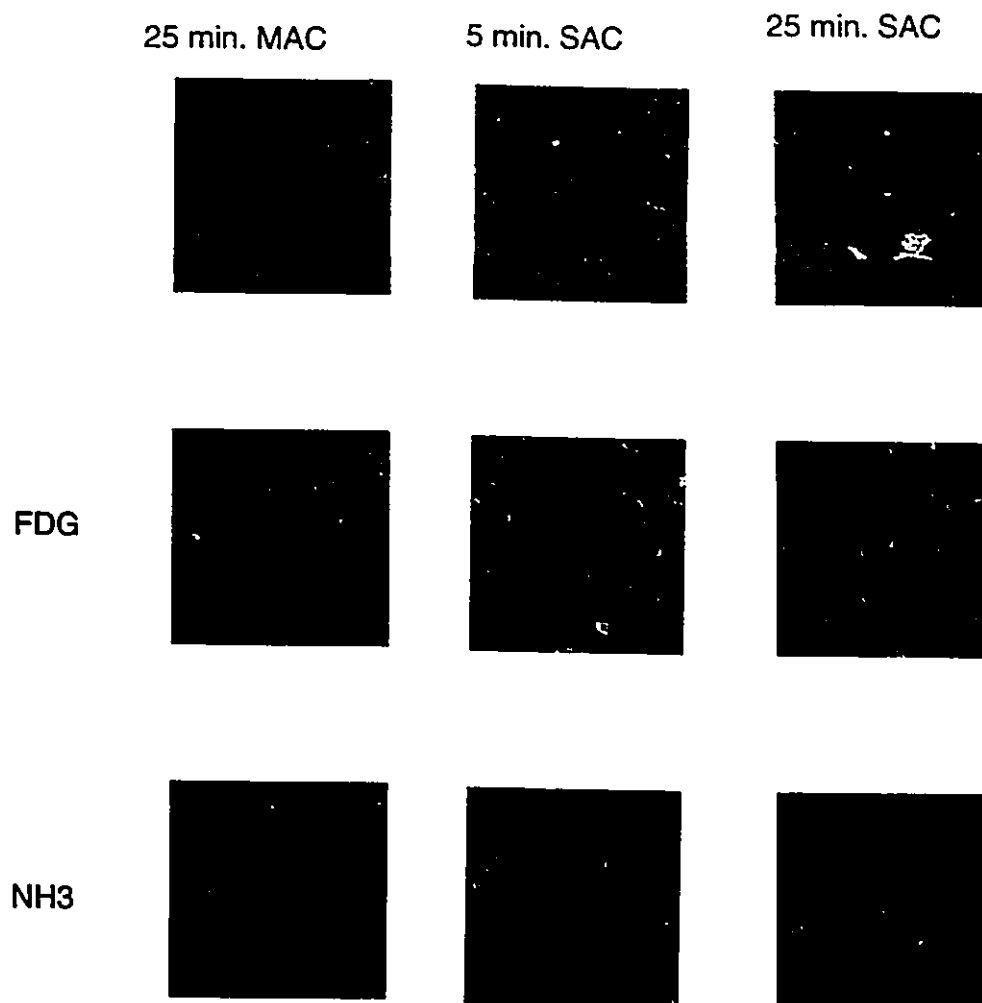


Figure 4.8 Results of a study in a patient with a history of ischaemic heart disease. The first row shows the transmission images (25 min., segmented 5 min., and segmented 25 min. from the left). The second and third rows show the ^{18}F FDG and ^{13}N -ammonia images respectively, reconstructed with the corresponding attenuation data in the first row.

4.7 DISCUSSION

The ability to measure directly and to correct for gamma ray attenuation makes PET an inherently quantitative procedure, enabling the biokinetics of the organ of interest to be studied in vivo (Phelps *et al* 1986). In cardiac studies, the attenuation properties of the subject are measured directly using an external source of radiation. Practically, the acquisition time for a transmission measurement is forced to be short, and the counting statistics are insufficient. During a transmission measurement, the recorded data are inevitably contaminated by the detection of photons which have been scattered in the object being imaged. These scattered events lead to an underestimation of the attenuation coefficients. Scatter contamination in the transmission data can be corrected for by techniques such as rod windowing (Thompson *et al* 1986) or dual energy window (Grootenk *et al* 1992, Yu and Nahmias 1995) in an attempt to provide more accurate attenuation data, but this will increase the noise level. Therefore, a technique is required that reduces both the effects of the Poisson noise and of scatter radiation in the attenuation data, and provides accurately the local distributions of attenuation coefficients within the object.

In this work, a new SAC technique has been developed that uses ANN to calculate the probability that any given pixel belongs to the class 'soft tissue', and that gives an accurate attenuation coefficient given that probability. First, the transmission data are filtered using a three dimensional median filter to reduce the statistical noise, and to augment the in-plane information with information from adjacent planes. Then the information from a pixel and its 48 nearest neighbors are used as input to an ANN. The ANN consists of two parts: principal component analysis (PCA) and backpropagation multilayer perceptrons (MLP). The purpose of the PCA is to extract the important features from the local matrix of 7x7 pixels such that fewer but more informative data are used as the input to the MLP. The outputs of the MLP are the conditional probabilities

that the central pixel of the local 7×7 neighborhood belongs to the tissue class 'air', 'lung', and 'soft tissue'. In practice, for pixels belonging to one class, the probability of those pixels belonging to the class is not one, and the other two probabilities are not zero, so that the attenuation coefficient to be assigned to those pixels cannot be obtained as the weighted sum of those probabilities multiplied by the appropriate theoretical attenuation coefficients for each of the classes (Meikle *et al* 1993).

A calibration procedure is used to map the output of the ANN to the appropriate attenuation coefficients. It is sufficient to consider the probability of any pixel belonging to the class 'soft tissue' ($P(\text{soft tissue}|\mathbf{x})$) as it was observed that there is a one-to-one correspondence between $P(\text{air}|\mathbf{x})$ and $P(\text{soft tissue}|\mathbf{x})$, and that this last probability exhibits the widest range of values (figure 4.3). A fourth order polynomial function relating $P(\text{soft tissue}|\mathbf{x})$ to attenuation coefficients that had been carefully measured in a scatter corrected transmission study can then be used to obtain a continuous range of linear attenuation coefficient values. This method was validated by comparing the results obtained with the theoretical linear attenuation coefficient values for the materials used in the calibration (table 4.2). The method was validated further by measuring the attenuation coefficients of materials not included in the calibration (tables 4.4 and 4.5). Therefore, the method does not rely on any knowledge of the theoretical attenuation coefficients of the tissue types that may be present in the object. We have demonstrated that the method does not require scatter correction of the transmission data (table 4.2). The method gives reproducible results to within 3% (table 4.4 and figure 4.7). The accuracy of the segmented data increases with increasing counting statistics, but acceptable results are obtained from studies containing as few as 400,000 counts per plane (figures 4.5 and 4.6).

The attenuation correction method that we have developed was shown to correct adequately emission data from a phantom (table 4.5). It was also shown to correct satisfactorily patient studies (figure 4.8).

The advantage of our approach is that it does not depend on the accurate delineation of boundaries between tissues in a transmission image (Huang *et al* 1981), nor does it rely on pixel intensity histograms to assign a give pixel to a given tissue class (Xu *et al* 1991, Meikle *et al* 1993, and Xu *et al* 1994). The use of artificial neural networks allows for the incorporation of local neighborhood data in the classification of pixels, making the method less susceptible to noise. The introduction, and validation of the calibration curve relating $P(\text{soft tissue}|x)$ to absolute value of μ , removes the requirement of scatter correction of the transmission data. Furthermore, this allows for the calculation of more precise ACF's as the method is sensitive to local variations in μ that are expected in clinical studies (Robinson and Kreel 1979). In practice, accurate ACF's can be obtained by acquiring a short transmission scan using the single-photon transmission measurement technique (deKemp and Nahmias 1994, Yu and Nahmias 1995), and then processing these data using the method developed in this chapter. This is illustrated in figure 4.9.

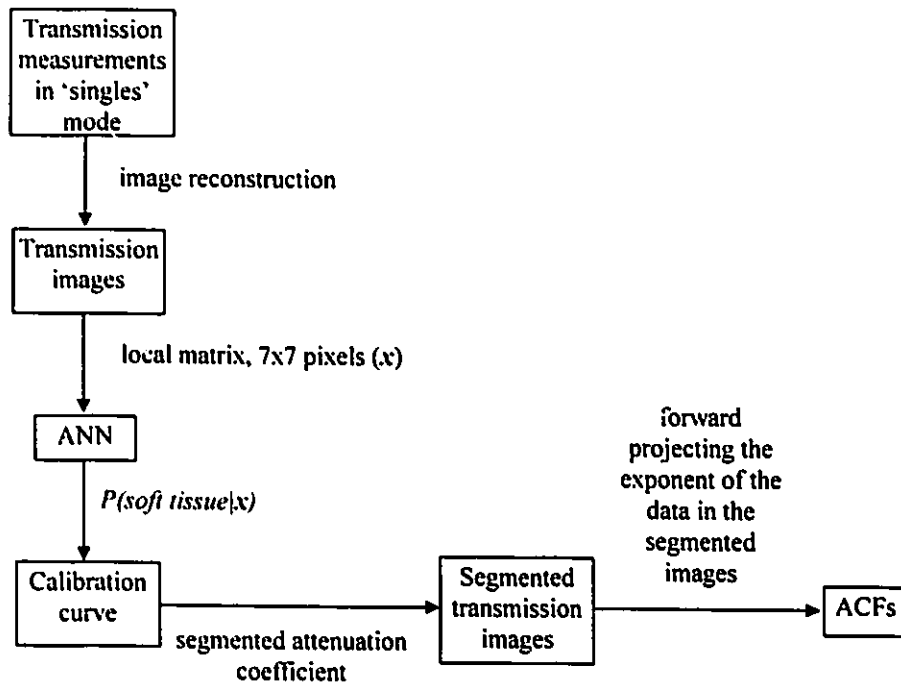


Figure 4.9 Block diagram for obtaining accurate ACFs using 'singles' measurements and ANN.

REFERENCES

- Bacharach SL, Douglas MA, Carson RE, Kalkowski PJ, Freedman N, Perrone-Filardi P, and Bonow RO (1993). Three-dimensional registration of cardiac positron emission tomography attenuation scans. *J. Nucl. Med.* 34:311-321.
- Bettinardi V, Gilardi MC, Lucignani G, Landoni C, Rizzo G, Striano G, and Fazio F (1993). A procedure for patient repositioning and compensation for misalignment between transmission and emission data in pet heart studies. *J. Nucl. Med.* 34:137-142.
- Dahlbom M, and Hoffman EJ (1987). Problems in signal-to-noise ratio for attenuation correction in high resolution PET. *IEEE Trans. Nucl. Sci.* 34:288-293.
- Darken C and Moody J (1992). Towards Faster Stochastic Gradient Search. *In Advances in Neural Information Processing Systems 4*. (Moody JE, Hanson SJ, and Lippmann RP, eds.) San Mateo, CA: Morgan Kaufmann 1009-1016.
- deKemp R and Nahmias C (1994). Attenuation correction in PET using single photon transmission measurement *Med. Phys.* 21:771-778.
- Fahlman SE and Lebiere C (1990). The cascade-correlated learning architecture. *In Advances in Neural Information Processing Systems 2*. (Touretzky DS, ed.) San Mateo, CA: Morgan Kaufmann 524-532.
- Fallen EL, Nahmias C, Scheffel A, Coates G, Beanlands R, and Garnett ES (1995). Redistribution of myocardial blood flow with topical nitroglycerin in patients with coronary artery disease. *Circulation* 91:1381-1388.
- Gonzalez RC, and Wintz P (1987). *Digital Image Processing*. Massachusetts: Addison-Wesley 191-195.
- Grootenck S, Spinks T J, Jones T, Michel C, and Bol A (1992). Correction for scatter using a Dual-Energy-Window technique with a tomography operated without

- septa. *IEEE 1991 Medical Imaging Conf. Rec. (Santa Fe, NM, 1991)* New York:IEEE 1569-1573.
- Haykin S (1994). *Neural Networks A Comprehensive Foundation*. New York: Macmillan
- Huang SC, Hoffman EJ, Phelps ME, and Kuhl DE (1979). Quantitation in positron emission tomography: 2. Effect of inaccurate attenuation correction. *J. Comp. Assit. Tomogr.* 3:804-814.
- Huang SC, Carson RE, Phelps ME, Hoffman EJ, Schelbert HR, and Kuhl DE (1981). A boundary method for attenuation correction in positron computed tomography. *J. Nucl. Med.* 22:627-637.
- Karp JS, Muehlelehner G, Qu H, and Yan XH (1995). Singles transmission in volume-imaging PET with a ^{137}Cs source. *Phys. Med. Biol.* 40:929-944.
- McCord ME, Bacharach SL, Bonow, RO, Dilsizian V, Cuocolo A, and Freedman N (1992). Misalignment between PET transmission and emission scans: Its effect on myocardial imaging. *J. Nucl. Med.* 33:1209-1214.
- Meikle SR, Dahlbom M, and Cherry SR (1993). Attenuation correction using count-limited transmission data in positron emission tomography. *J Nucl. Med.* 34:143-144.
- Ostertag H, Kubler WK, Doll J, Strauss LG, and Lorentz WJ (1989). Measured attenuation correction methods. *Eur. J. Nucl. Med.* 15:722-726.
- Palmer MR, Rogers JG, Berstrom M, Beddoes MP, and Pate BD (1986). Transmission profile filtering for positron emission tomography. *IEEE Trans. Nucl. Sci.* 33:478-481.
- Phelps M, Mazziotta J, and Schelbert H (1986). *Positron emission tomography and autoradiography: Principles and applications for the brain and heart*. New York: Raven Press.

- Robinson PJ and Kreel L (1979). Pulmonary tissue attenuation with computed tomography: Comparison of inspiration and expiration scans. *J. Comput. Assist. Tomogr.* 3:740-748.
- Reddi SS, Rudin SF, and Keshavan HR (1984). An optimal multiple threshold scheme for image segmentation. *IEEE Trans. Syst. Man Cybern.* 14:661-665.
- Thompson CJ, Dagher A, Lunney DN, Strother SC, and Evans AC (1986). A technique to reject scattered radiation in PET transmission scans. *International Workshop on Physics and Engineering of Computerized Multidimensional Imaging and Processing* (Nalcioglu O, Cho ZH, and Budinger TF, eds.) Proc SPIE 671:244-253.
- Webber C (1981). *Compton scattering in the measurement of lung density*. University of Surrey: Ph.D. Thesis.
- Xu EZ, Mullani NA, Gould KL, and Anderson WL (1991). A segmented attenuation correction for PET. *J. Nucl. Med.* 32:161-165.
- Xu M, Luk WK, Cutler PD, and Digby WM (1994). Local threshold for segmented attenuation correction of PET imaging of the thorax. *IEEE Trans. Nucl. Sci.* 41:1532-1537.
- Yu SK and Nahmias C (1995). Single-photon transmission measurements in positron tomography using ^{137}Cs . *Phys. Med. Biol.* 40:1255-1266.
- Yu SK and Nahmias C (1996). Segmented attenuation correction using artificial neural network in positron tomography (*Phys. Med. Biol.* in the press)

CHAPTER 5

CONCLUSION AND FUTURE WORK

5.1 CONCLUSION

Measured attenuation correction in cardiac PET studies is routinely performed using transmission scans. Reduction in acquisition time of the scans and noise in the measured data are necessary in order to provide accurate attenuation data with minimal patient discomfort.

Recently, a technique has been developed to acquire transmission data in 'single' mode (deKemp and Nahmias 1994) which results in a significant improvement in statistics. During the course of this research, ^{137}Cs was shown to be a suitable radiation source for transmission scans in PET using this 'singles' transmission measurement technique (Yu and Nahmias 1995). To correct for scattered radiation, and to extrapolate the measured linear attenuation coefficients from 662 keV to 511 keV, a modified dual energy scatter correction technique and a simple extrapolation technique have also been developed in this work. Using the developed techniques, the linear attenuation coefficients measured in 'singles' mode with ^{137}Cs as the radiation source compare well with the expected values.

A new segmentation attenuation correction technique has also been developed in this work. This technique requires short transmission scan times, and is capable of providing accurate, subject independent and reproducible attenuation data without the need for scatter correction. It can predict accurately the value of the attenuation coefficient for any material in the range from air to water.

Therefore, accurate attenuation data can be obtained by acquiring a short transmission scan in 'singles' mode, and then processing the data using the new segmentation attenuation correction method.

5.2 FUTURE WORK

5.2.1 Application of the ANN Technique for Attenuation Correction in PET/CT System

Recently, there has been an interest in using X-ray CT transmission data to correct for photon attenuation in a PET/CT scanner (Beyer *et al* 1995). The major advantage of the technique is that it allows high statistics attenuation data to be obtained in a short time, and there are no problem in coregistrating the emission and transmission data. However, the CT data are acquired using a polychromatic beam of X-rays with a maximum energy of 120 keV, whereas the PET emission data are acquired using monochromatic gamma rays at 511 keV. Therefore, conversion of the CT data from a mean energy of 80 keV to the attenuation coefficient for PET at 511 keV is required.

There are several possible methods for this conversion. In 1993, Hasegawa *et al* successfully obtained a monoenergetic attenuation map by using dual-energy X-ray CT. The technique converts the CT projection data into two basis materials projection data using calibration data; the fractional contribution of each material is then obtained and multiplied by the corresponding linear attenuation coefficient at the radionuclide energy to synthesize the monoenergetic attenuation map. A different approach is to segment the CT attenuation image into different regions, and then to assign the attenuation

coefficients for those regions at 511 keV. Another possible approach is to extrapolate the measured CT data from the mean energy of 80 keV to 511 keV (Beyer *et al* 1995).

These methods are practical and effective. However, they cannot account for the noise due to image reconstruction using filtered-backprojection. Moreover, it is preferable to use lower mAs settings to minimize the radiation dose to the patient. Thus, an approach using artificial neural network (ANN) (Yu and Nahmias 1996) may be more appropriate since it is capable of providing accurate attenuation data with substantial reduction of noise.

The ANN technique used in this preliminary study is similar to the one described in chapter 4, except for some minor changes. Since the noise in the CT image is low, the 3D median filtering step is removed, and because CT images are reconstructed using a 512x512 grid, the local matrix used as input to the ANN is changed from 7x7 to 3x3 to reduce the processing time. The transmission image is segmented into three classes: air, soft tissue or bone, instead of air, lungs and soft tissue in our previous network. For training of the ANN, an artificially generated CT image is used as shown in figure 5.1. CT number of -1000, 0 and 1500 are assigned to the respective regions of air, water and bone in the training image.

For the purpose of calibration, a 20 cm water phantom containing inserts of materials with different attenuation properties was scanned on a GE 9800 QUICK CT scanner at 120 kVp and two different mAs (200 and 400) settings. The calibration curve is shown in figure 5.2. The material in the inserts included balsa wood, light pine wood, pine wood, maple wood, hexane, methanol, and aluminum. The measured CT numbers, theoretical and segmented linear attenuation coefficients of the inserts at 511 keV are listed in table 5.

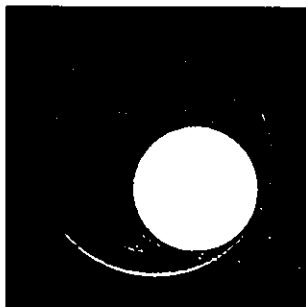


Figure 5.1 An artificially generated CT image is used for training the ANN.

Table 5.1 Theoretical linear attenuation coefficient and segmented linear attenuation coefficient of the inserts.

Material	Measured CT number	Segmented linear attenuation coefficient (cm^{-1}) at 511 keV	Theoretical linear attenuation coefficient (cm^{-1}) at 511 keV
Balsa	-842	0.006	0.011
Light Pine	-596	0.035	0.035
Pine	-523	0.044	0.044
Hexane	-323	0.065	0.066
Methanol	-241	0.074	0.072
Maple	-210	0.077	0.079
Water	10	0.097	0.096
Aluminum	1891	0.023	0.023

The original CT images and the segmented images are shown in figure 5.3. Since the matrix size and spatial resolution for CT images (512x512, 0.5 mm) is different than the PET images (128x128, 6 mm), the CT images are first compressed and the segmented images are convoluted with a Gaussian filter. The resultant images are shown in figure 5.4.

In this preliminary study, encouraging results (table 5.1 and figure 5.4) are obtained using the ANN technique for the conversion of CT data to attenuation map for PET.

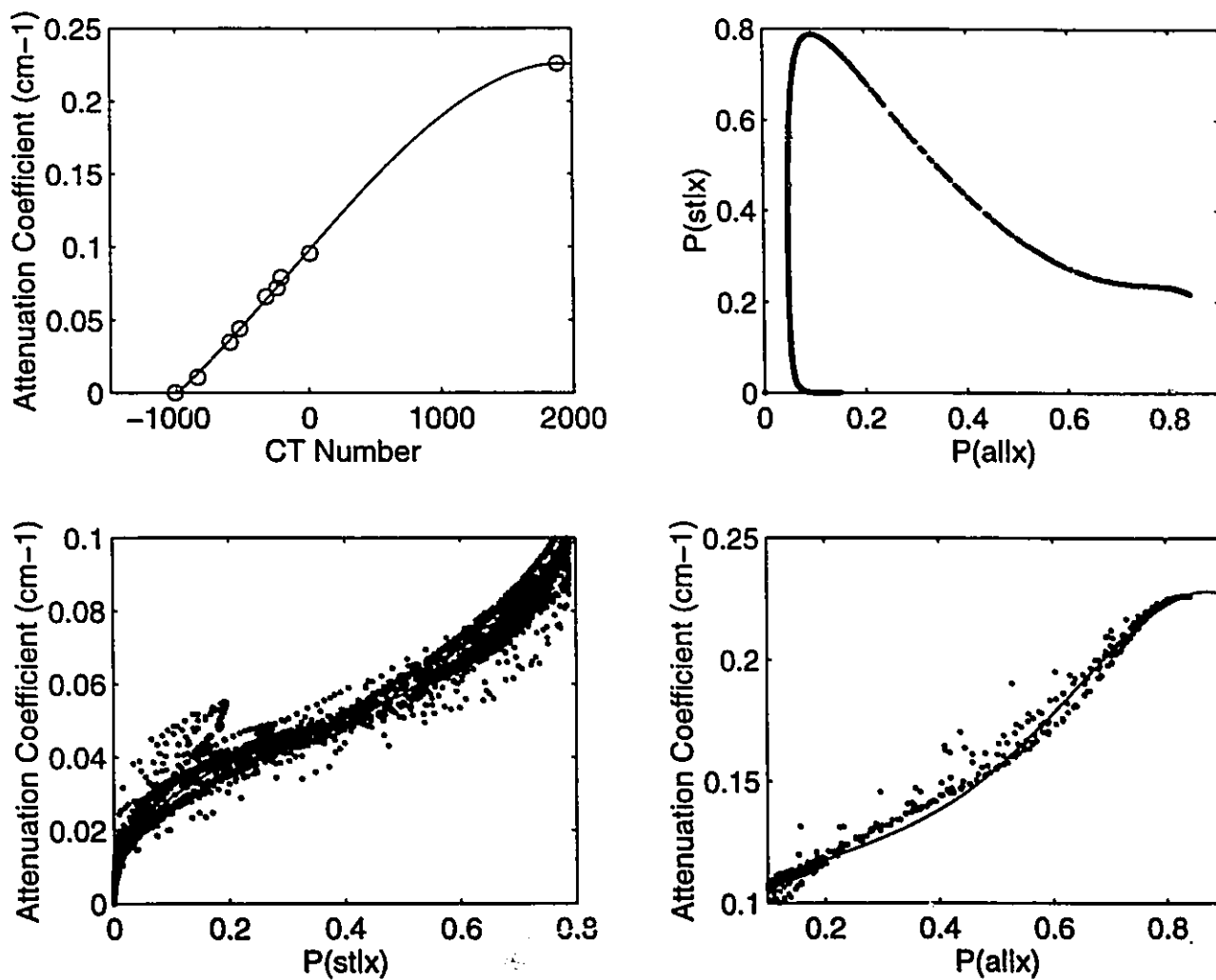


Figure 5.2 The top left curve shows the mapping from CT number to attenuation coefficients. The top right curve indicates that the conditional probabilities of a pixel being soft tissue ($P(\text{st}|x)$) and aluminium ($P(\text{al}|x)$) are a one-to-one function if $P(\text{al}|x)$ is larger than 0.2. Therefore, the calibration curve on the bottom right which converts $P(\text{al}|x)$ to attenuation coefficients is used when $P(\text{al}|x)$ is larger than 0.2, otherwise, the calibration curve on the bottom left which converts $P(\text{st}|x)$ to attenuation coefficients is used.

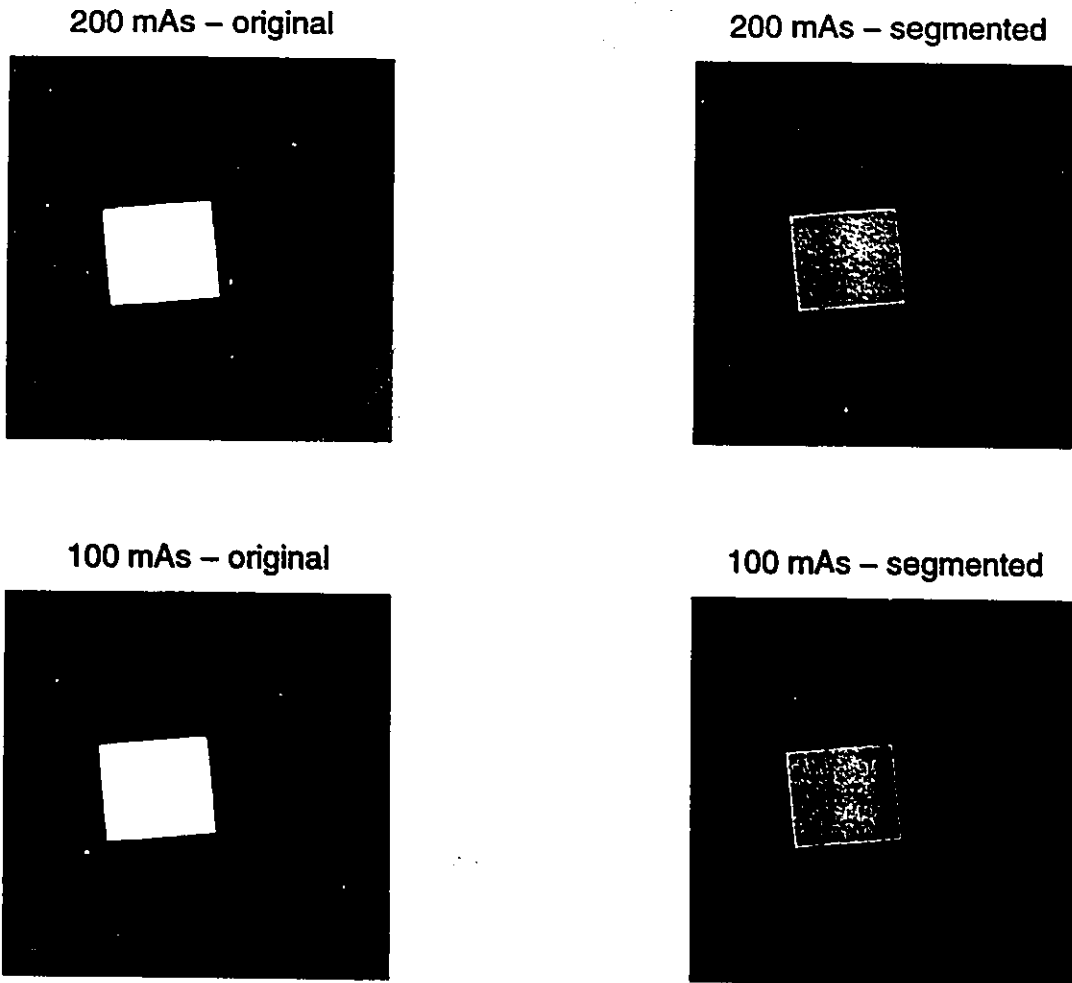


Figure 5.3 The original CT images (left) and the segmented CT images (right).

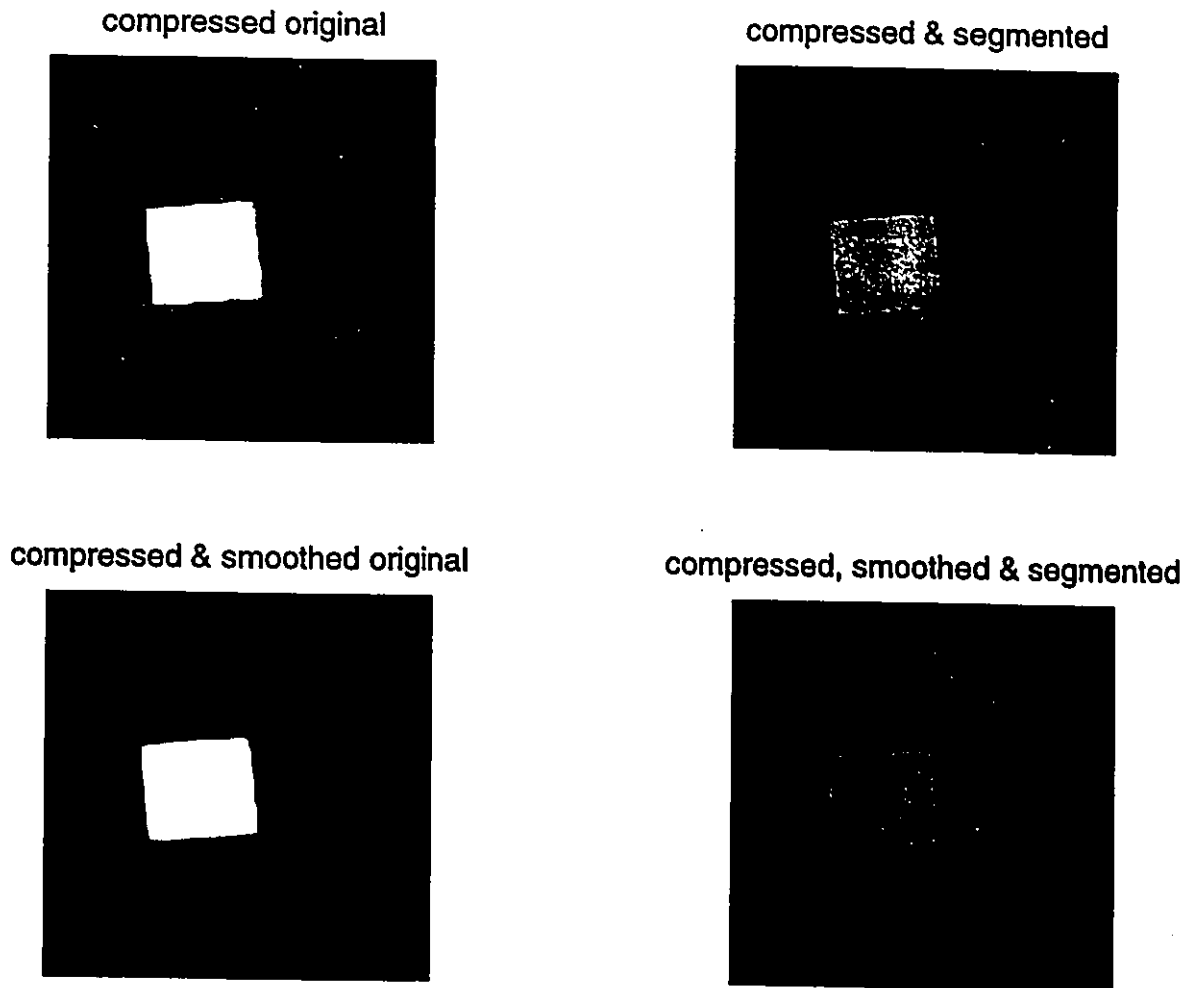


Figure 5.4 The CT images (left) and segmented images (right) after reduction of matrix size from 512x512 to 128x128. The images are smoothed with a 9x9 Gaussian filter to obtain spatial resolution of 6 mm.

5.2.2 Application of the ANN Technique for Assaying Heterogeneous Radioactive Wastes

It has been shown that the tomographic gamma-scanning (TGS) technique is useful for assaying heterogeneous radioactive wastes (Estep 1990). An emission scan produces a map of the radiation intensity, while a transmission scan gives the attenuation properties of the object. Combining the two allows accurate assay even with a complex emitter distribution. However, the assay speed is often considered a limitation when applying this method for waste management.

Since the ANN technique developed in this work is capable of predicting accurate attenuation coefficients for any material in a specified range, a fast and accurate assay can be obtained if the ANN technique is incorporated in the TGS technique.

5.2.3 Evaluation of the Diagnostic Performance of the ANN Technique

In the last chapter, the ANN technique has been verified for the capability of providing accurate attenuation data from noisy transmission data. However, there are still questions remaining. Will the physician come to a different diagnosis if different attenuation methods are applied? How much increase in the sensitivity and specificity will be obtained using the ANN technique compared to the conventional measured attenuation method?

To answer these questions, an objective evaluation of the diagnostic performance of the technique is necessary. This evaluation can be achieved by performing a receiver operating characteristic (ROC) analysis for clinical cardiac studies using the different attenuation correction techniques.

REFERENCES

- Beyer T, Kinahan P, Townsend D, and Sashin D (1995). Attenuation correction for a combined 3D PET/CT scanner. *1995 International Meeting on Fully Three-Dimensional image Reconstruction in Radiology and Nuclear Medicine, Aix-les-Bains-Savoie-France.*
- deKemp R and Nahmias C (1994). Attenuation correction in PET using single photon transmission measurement. *Med. Phys.* 21:771-778.
- Estep RJ (1990). Assay of heterogeneous radioactive wastes by low-resolution tomographic gamma scanning. *Trans. Am. Nucl. Soc.* 62:178.
- Hasegawa BH, Lang TF, Brown JK, Gingold EL, Reily SM, Blankespoor SC, Liew SC, Tsui BMW, and Ramanathan C (1993). Object-specific attenuation correction of SPECT with correlated dual-energy X-ray CT. *IEEE Trans. Nucl. Sci.* 40:1242-1252.
- Yu SK and Nahmias C (1995). Single-photon transmission measurements in positron tomography using ^{137}Cs . *Phys. Med. Biol.* 40:1255-1266.
- Yu SK and Nahmias C (1996) Segmented attenuation correction using artificial neural network in positron tomography. (*Phys. Med. Biol.* in the press).

100

100

GLOSSARY

ACF : Attenuation correction factor. It is calculated as the ratio of blank/transmission. Correction for attenuation of emission data is performed by multiplying the ACF with the appropriate line of response from the emission data.

ANN : Artificial neural network. An artificial neural network is an interconnected network of simple processing elements. Communication between processing elements occurs along paths of variable connection strengths. By changing the values of these connection strengths through a training process, the network is capable of storing the knowledge and making it available for use.

BGO : Bismuth germanate. The scintillation detector used in many PET scanners. When a gamma ray interacts with the detector material, a flash of light is emitted the intensity of which is proportional to the amount of energy deposited by the gamma ray in the scintillator.

CSDA : Continuous slowing down approximation. It is a schematization in which the rate of energy loss at each point along an electron or positron trajectory is assumed to be equal to the mean energy loss.

CT : Computed tomography.

DEW : Dual-energy-window. This refers to a scatter correction technique which is based on the assumption that the scattered events in the photopeak window is a constant fraction of the scattered events acquired in a scatter window.

¹⁸FDG : ¹⁸F-fluorodeoxyglucose. It is a biochemical molecule used for measuring the distribution of glucose consumption in vivo. ¹⁸F-fluorodeoxyglucose and glucose share the same carrier that transports them between plasma and tissue, and are substrates for hexokinase, which phosphorylates them to their respective hexose-6-phosphates. Unlike glucose-6-phosphate which is metabolized further eventually into CO₂ and water, deoxyglucose-6-phosphate is not a substrate for glucose-6-phosphate dehydrogenase. Deoxyglucose-6-phosphate is therefore essentially trapped in the tissues.

FOV : Field of view.

FWHM : Full-width at half-maximum. It is a measure of resolution. It is defined as the width of the distribution at a level which is half the maximum ordinate of the peak.

GHA : Generalized Hebbian algorithm. It is a self-organized, feedforward network composed of a single layer of processing elements. It performs principal component analysis, and operates under the Hebbian learning rule.

HWHM : Half-width at half-maximum. It is equal to half of the FWHM.

LOR : Line of response. It is the line joining two detectors that have detected two gamma rays within the coincidence timing window. LOR data are recorded in terms of angle and radius coordinates based on a perpendicular line from the LOR to the center of the field of view.

MLP : Backpropagation multilayer perceptrons. A type of artificial neural network which consists of multilayers of nodes, and which contains 'knowledge' learned using a backpropagation training algorithm.

MAC : Measured attenuation correction.

MSE : Mean square error.

Nal(Tl) : Thallium-activated sodium iodide. A commonly used scintillation material for gamma ray spectroscopy.

$^{13}\text{NH}_3$: ^{13}N -ammonia. It is a biochemical molecule used for measuring blood flow in vivo.

PCA : Principal component analysis. A transformation of the data such that they can be represented by a reduced number of "effective" features and still retain most of the information content of the data.

PET : Positron tomography. It is a tomographic imaging technique which is capable of providing quantitative measures of the distribution of administered "physiological" tracers which have been labeled with positron emitters.

PMT : Photomultiplier tube. The PMT is used to amplify the flash of light emitted by the BGO crystals. They are optically coupled to the BGO crystals forming the fundamental components of a detector block.

PSF : Point spread function. It is a count rate profile as a function of position obtained from a point source.

RC : Random coincidence. It occurs when two photons from separate annihilations strike the detector within the timing coincidence window. RC events incorrectly assume an annihilation event occurred along a particular LOR introducing noise in the coincidence data.

τ_c : Coincidence timing window (12 ns is used in ECAT 931/31). Events are assumed to be in coincidence if they are recorded within that interval of time. The coincidence timing window takes into account the timing resolution of the detector system and the difference in time of flight of the photons.

SAC : Segmented attenuation correction.

SNR : Signal-to-noise ratio.

SPECT : Single photon emission computed tomography. Similar to positron tomography, SPECT is an emission computed tomographic technique. Instead of detecting annihilation photons in coincidence, a gamma camera is used to record the spatial distribution of single photons. Projection data are collected with the gamma camera at different angles around the object under study. Transaxial tomographic images are then reconstructed to represent the relative distribution of the administered radiopharmaceutical.

RTS : Real time sorter. A device which sorts the lines of response into their correct location in the sinogram.

APPENDIX A : HUMAN STUDIES

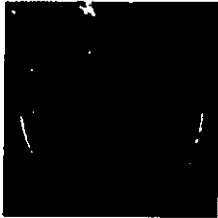
In this appendix, results from seven patient studies are shown in the following pages. For each patient, regional myocardial blood flow and metabolism were measured using ^{13}N -ammonia (NH_3) and ^{18}F -fluorodeoxyglucose (^{18}FDG). The emission data for both NH_3 and ^{18}FDG studies were corrected for attenuation using the 25 minute measured data, the 5 minute or the 25 minute segmented transmission data. The net true counts acquired in plane #20 for the 5 minute and the 25 minute transmission scans for each patient are also given in table A.1.

Table A.1 The acquired net trues in plane #20 for 5 minute and 25 minute transmission scans for each patient.

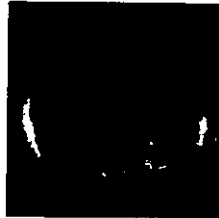
Subject	5 minute scan	25 minute scan
1	177,740	776,981
2	242,409	1,106,708
3	189,896	911,776
4	211,467	943,765
5	248,278	1,136,675
6	257,680	1,132,999
7	179,432	790,564

Images shown in the following pages are all from plane #20, the first row shows the measured and segmented transmission images, the second and third rows show the attenuation corrected emission images for ^{18}FDG and NH_3 respectively.

25 min. MAC



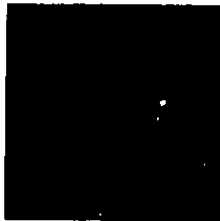
5 min. SAC



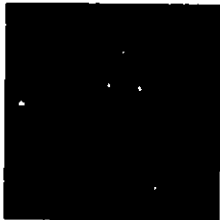
25 min. SAC



FDG



NH3



Subject #1

25 min. MAC



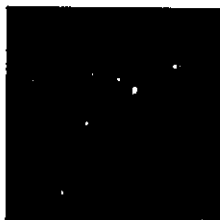
5 min. SAC



25 min. SAC



FDG

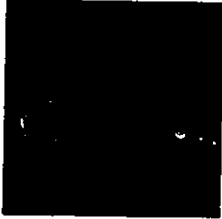


NH3



Subject #2

25 min. MAC



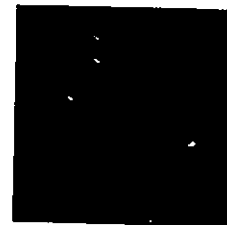
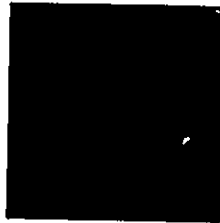
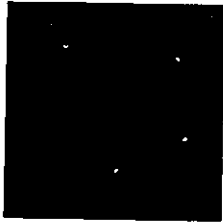
5 min. SAC



25 min. SAC



FDG



NH3



Subject #3

25 min. MAC



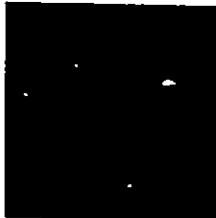
5 min. SAC



25 min. SAC



FDG

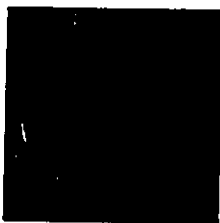


NH3

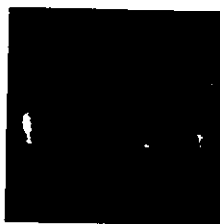


Subject #4

25 min. MAC



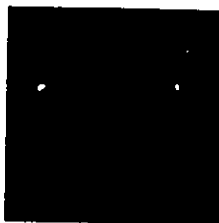
5 min. SAC



25 min. SAC



FDG

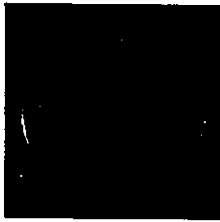


NH3



Subject #5

25 min. MAC



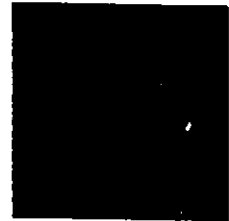
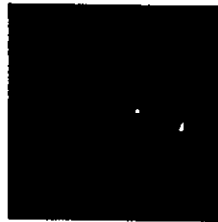
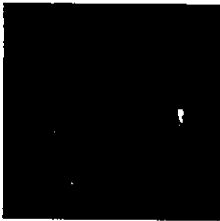
5 min. SAC



25 min. SAC



FDG

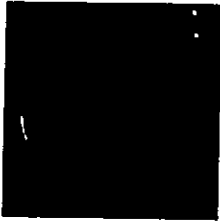


NH3



Subject #6

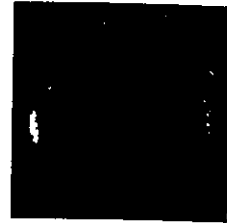
25 min. MAC



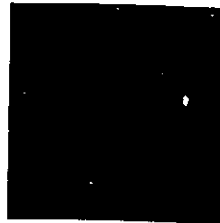
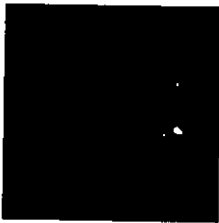
5 min. SAC



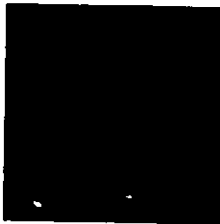
25 min. SAC



FDG



NH3



Subject #7

APPENDIX B : PROGRAM LISTING

Program: sac.c

```
/*.....*/
/*
/* Purpose :      This program is a short version of the ANN for SAC.      */
/*               and the training routine has been taken out. With          */
/*               the predefined weighting factors stored in files            */
/*               'w.dat' and 'pcaw.dat', this program calculates the         */
/*               attenuation coefficients in attenuation map based on        */
/*               the conditional probabilities of the three tissues.         */
/*               Results are then forward projected.                        */
/*
/* To use :      [1]   Type sac to run this program.                        */
/*               [2]   Enter the transmission image filename.              */
/*               [3]   When the segmentation is done, an attenuation map    */
/*               is created. The filename is the same as the image         */
/*               filename except the extension is changed from .img        */
/*               to _sac.atn.                                              */
/*
/* Author :      Ben Yu                                                    */
/*
/* Date : Feb, 1995.                                                       */
/*
/*.....*/
```

```
#include <stdio.h>
#include <math.h>
#include <stdlib.h>
#include <string.h>
#include <ctype.h>
#include <time.h>
#include <fcntl.h>
#include <malloc.h>
#include "matrix.h"

#define a 1.716
#define b 0.6666666667
#define output_node 3
#define input_node 5
#define hidden_node1 10
#define hidden_node2 5
#define m_size 128
#define t_size 122
#define n_epoch 20
```

```

#define pcap 49
#define pcam 7

double *w1,*w2,*w3,*yi,*yo,*yh;
double *th1,*th2,*th3,*w;
float *x,*yy;
short *t1;
int num_dat=t_size*t_size;
double RAND_MAX=(((unsigned) 1<<31)-1);

/*****/
/* activation function */
double bipolar(v)
    double v;
{
    if (v > 50.0) return 1.716;
    if (v < -50.0) return -1.716;
    return (double) (a*(1.0-exp(-b*v))/(1.0+exp(-b*v)));
} /* end of bipolar */
/*****/
/* activation function */
double sigmoid(v)
    double v;
{
    if (v > 50.0) return 1;
    if (v < -50.0) return 0;
    return (double) (1.0/(1.0+exp(-v)));
} /* end of sigmoid */
/*****/
/* normalize data set to the range from 0 to 10 */
void norm_x_dat()
{
    int i;
    float dat_max=-9999.9,dat_min=9999.9, p;

    for (i=0;i<(num_dat*pcap);i++) {
        p=x[i];
        if (p > dat_max) dat_max=p;
        if (p < dat_min) dat_min=p;
    }
    p=dat_max-dat_min;
    for (i=0;i<(num_dat*pcap);i++)
        x[i]=10.0*(x[i]-dat_min)/p;

} /* end of norm_train_dat */
/*****/
/* normalize data set to the range from 0 to 10 */
void norm_y_dat()

```

```

{
    int i;
    float dat_max=-9999.9,dat_min=9999.9, p;

    for (i=0;i<(num_dat*input_node);i++) {
        p=yy[i];
        if (p > dat_max) dat_max=p;
        if (p < dat_min) dat_min=p;
    }
    p=dat_max-dat_min;
    for (i=0;i<(num_dat*input_node);i++)
        yy[i]=10.0*(yy[i]-dat_min)/p;

    } /* end of norm_train_dat */
/*****
/* forward computation */
void forcom(n)
    int n;
{
    int i,j,k;
    double v;
    for (j=0;j<hidden_node1;j++) { /* input-hidden1 layer */
        v=0.0;
        for (i=0;i<input_node;i++)
            v+=w1[j*input_node+i]*((double) yy[n*input_node+i]);
        v-=th1[j];
        yi[j]=bipolar(v);
    } /* end of input-hidden layer */

    for (k=0;k<hidden_node2;k++) { /* hidden1-hidden2 layer */
        v=0.0;
        for (j=0;j<hidden_node1;j++)
            v+=w2[k*hidden_node1+j]*yi[j];
        v-=th2[k];
        yh[k]=bipolar(v);
    } /* end of hidden1-hidden2 layer */

    for (k=0;k<output_node;k++) { /* hidden2-output layer */
        v=0.0;
        for (j=0;j<hidden_node2;j++)
            v+=w3[k*hidden_node2+j]*yh[j];
        v-=th3[k];
        yo[k]=sigmoid(v);
    } /* end of hidden2-output layer */

    } /* end of forcom */
/*****
/* open pca weight file */
void open_pca()

```

```

{
    int i;
    FILE *fw;

    if ( (fw=fopen("pcaw.dat","r")) == NULL ) {
        printf("Error opening pca weight file\n");
        exit(1); }

    for (i=0;i<(pcap*pcam);i++)
        fscanf(fw,"%lf",&w[i]);
    } /* end of open_pca */
/*****/
/* PCA algorithm */
void pca()
{
    int n,i,j,k;

    for (n=0;n<num_dat;n++)
        for (j=0;j<input_node;j++) {
            k=n*input_node+j;
            yy[k]=0.0;
            for (i=0;i<pcap;i++)
                yy[k]+=((float) w[j*pcap+i])*x[n*pcap+i];
        }
    norm_y_dat();

    } /* end of pca */
/*****/
/* This is an 3x3x3 median filter */
void medf3(t1,t3,t4)
    short int *t1,*t3,*t4;
{
    int i,j,k,l,tot,c;
    int ave,diff,min,emp;
    short *t;

    t=(short *) calloc(m_size*m_size,sizeof(short));
    for (i=0;i<(m_size*m_size);i++)
        t[i]=t1[i];

    for (i=1;i<127;i++)
        for (j=1;j<127;j++) {
            min=100000;
            tot=emp=diff=0;
            for (k=-1;k<2;k++)
                for (l=-1;l<2;l++) {
                    c=128*(i+k)+j+l;

```

```

                                tot=tot+t1[c]+t3[c]+t4[c];
                                }
ave=(int)(tot/27);
for (k=-1;k<2;k++)
    for (l=-1;l<2;l++) {
        c=128*(i+k)+j+l;
        diff=abs(ave-t1[c]);
        if (diff < min) {
            min=diff;
            emp=t1[c];
        }
        diff=abs(ave-t3[c]);
        if (diff < min) {
            min=diff;
            emp=t3[c];
        }
        diff=abs(ave-t4[c]);
        if (diff < min) {
            min=diff;
            emp=t4[c];
        }
    }
    t[128*i+j]=emp;
}
for (i=0;i<(m_size*m_size);i++)
    t1[i]=t[i];

free(t);

} /* end of medf3 */
/*****
/* This is an 3x3x2 median filter */
void medf2(t1,t3)
    short int *t1,*t3;
{
    int i,j,k,l,tot,c;
    int ave,diff,min,emp;
    short *t;

    t=(short *) calloc(m_size*m_size,sizeof(short));
    for (i=0;i<(m_size*m_size);i++)
        t[i]=t1[i];

    for (i=1;i<127;i++)
        for (j=1;j<127;j++) {
            min=100000;
            tot=emp=diff=0;
            for (k=-1;k<2;k++)

```

```

        for (l=-1;l<2;l++) {
            c=128*(i+k)+j+l;
            tot+=t1[c]+t3[c];
        }
    ave=(int)(tot/18);
    for (k=-1;k<2;k++)
        for (l=-1;l<2;l++) {
            c=128*(i+k)+j+l;
            diff=abs(ave-t1[c]);
            if (diff < min) {
                min=diff;
                emp=t1[c];
            }
            diff=abs(ave-t3[c]);
            if (diff < min) {
                min=diff;
                emp=t3[c];
            }
        }
    t[128*i+j]=emp;
}
for (i=0;i<(m_size*m_size);i++)
    t1[i]=t[i];

free(t);

} /* end of medf2 */
/*****
/* retrieve weight parameters from a file */
void open_weight() {
    int i;
    FILE *ft;

    /* open weight data file */
    if ( (ft=fopen("w.dat","r")) == NULL ) {
        printf("Error opening input file\n");
        exit(1); }

    for (i=0;i<(hidden_node1*input_node);i++)
        fscanf(ft,"%lf",&w1[i]);

    for (i=0;i<hidden_node1;i++)
        fscanf(ft,"%lf",&th1[i]);

    for (i=0;i<(hidden_node2*hidden_node1);i++)
        fscanf(ft,"%lf",&w2[i]);

    for (i=0;i<hidden_node2;i++)

```

```

        fscanf(ft,"%lf",&th2[i]);

for (i=0;i<(hidden_node2*output_node);i++)
    fscanf(ft,"%lf",&w3[i]);

for (i=0;i<output_node;i++)
    fscanf(ft,"%lf",&th3[i]);

fclose(ft);

    } /* end of open_weight */
/*****
/* forward projection */
fproj( image, image_size, scan, num_views, num_projs)
float *image;
int image_size;
float *scan;
int num_views, num_projs;
{
    double t0, t1, d, N, offset, offset2;
    double offset1, c, s;
    int i, j, x, y, i0, r, bin, p, views, fbin;
    double theta;

    offset = (double) (image_size/2.0);
    offset2 = (double) (num_projs/2.0);
    N = (num_projs) / (double) image_size;
    for (i=0; i<num_views; i++) {
        theta = (double) (M_PI * (i - 81) / num_views);
        s = sin(theta);
        c = cos(theta);
        fbin = (191 - i)*160;
        offset1 = offset * (s + c);
        for (y=3; y<126; y++)
            for (x=3; x<126; x++) {
                p = x*image_size+y;
                if (image[p] > 0) {
                    t0=(((double) x)*c+((double) y)*s-offset1)*N;
                    t1=fabs(t0);
                    i0=(int) (t1);
                    d = t1 - (double) i0;
                    if (t0 >= 0.0) {
                        r = (int) ((offset2) + i0);
                        bin = fbin+r;
                        scan[bin] += (float) (1.0-d)*image[p];
                        scan[bin+1] += (float) d*image[p];
                    }
                }
            }
        else {

```

```

        r = (int) ((offset2) - i0 - 1);
        bin = fbin+r;
        scan[bin+1] +=(float) (1.0-d)*image[p];
        scan[bin] +=(float) d*image[p];
    }
}

return 0;
}

/*****
/* computation of results */
void results()
{
    short *t2,*t3,pm;
    int n,i,j,k,l,p,m,ii;
    double pst;
    char str[80], *filename;
    static short *att_buf;
    static int nprojs, nviews, nplanes=31;
    int image_size=128, num_views=192, num_projs=160;
    float *scan, *image;

    FILE *fout,*fp1;

    att_buf = (short*) malloc(num_views*num_projs*sizeof(short));
    scan = (float*) malloc( num_views*num_projs*sizeof(float));

    printf("\n\t Image filename : ");
    filename = gets(str);
    if (filename == NULL)
        printf("\n\t Input File NOT Found\n");

    fp1=fopen(filename, "r");

    i = strlen(filename);
    filename[i-4] = '_';
    filename[i-3] = 's';
    filename[i-2] = 'a';
    filename[i-1] = 'c';
    filename[i] = '.';
    filename[i+1] = 'a';
    filename[i+2] = 't';
    filename[i+3] = 'n';
    filename[i+4] = '\0';

```

```

if ((fout=fopen(filename,"wb")) == NULL) {
    printf("Output file open error.. exiting\n");
    exit(1);
}

/* skip the main header block of image file */

fseek(fp1,1024,0);

t1=(short *) calloc(m_size*m_size,sizeof(short));
t2=(short *) calloc(m_size*m_size,sizeof(short));
t3=(short *) calloc(m_size*m_size,sizeof(short));
image=(float *) calloc(m_size*m_size,sizeof(float));

for (i=0;i<(128*128);i++)
    image[i]=0.0;

for (ii=1;ii<=31;ii++) {
    if (ii == 1) {
        fseek(fp1,512,1);
        fread(t1,2,m_size*m_size,fp1);
        swab(t1,t1,m_size*m_size*2);
        fseek(fp1,512,1);
        fread(t2,2,m_size*m_size,fp1);
        swab(t2,t2,m_size*m_size*2);
        medf2(t1,t2); }
    else if (ii == 31) {
        for (i=0;i<(128*128);i++)
            t2[i]=t1[i];
        fseek(fp1,512,1);
        fread(t1,2,m_size*m_size,fp1);
        swab(t1,t2,m_size*m_size*2);
        medf2(t1,t2); }
    else {
        for (i=0;i<(128*128);i++) {
            t3[i]=t1[i];
            t1[i]=t2[i];
        }
        fseek(fp1,512,1);
        fread(t2,2,m_size*m_size,fp1);
        swab(t2,t2,m_size*m_size*2);
        medf3(t1,t2,t3); }

    for (i=0;i<t_size;i++)
        for (m=0;m<t_size;m++) {
            n=49*(i*t_size+m);
            x[n]=(float) t1[i*m_size+m];
        }
}

```

```
x[n+1]=(float) t1[i*m_size+m+1];
x[n+2]=(float) t1[i*m_size+m+2];
x[n+3]=(float) t1[i*m_size+m+3];
x[n+4]=(float) t1[i*m_size+m+4];
x[n+5]=(float) t1[i*m_size+m+5];
x[n+6]=(float) t1[i*m_size+m+6];
x[n+7]=(float) t1[(i+1)*m_size+m];
x[n+8]=(float) t1[(i+1)*m_size+m+1];
x[n+9]=(float) t1[(i+1)*m_size+m+2];
x[n+10]=(float) t1[(i+1)*m_size+m+3];
x[n+11]=(float) t1[(i+1)*m_size+m+4];
x[n+12]=(float) t1[(i+1)*m_size+m+5];
x[n+13]=(float) t1[(i+1)*m_size+m+6];
x[n+14]=(float) t1[(i+2)*m_size+m];
x[n+15]=(float) t1[(i+2)*m_size+m+1];
x[n+16]=(float) t1[(i+2)*m_size+m+2];
x[n+17]=(float) t1[(i+2)*m_size+m+3];
x[n+18]=(float) t1[(i+2)*m_size+m+4];
x[n+19]=(float) t1[(i+2)*m_size+m+5];
x[n+20]=(float) t1[(i+2)*m_size+m+6];
x[n+21]=(float) t1[(i+3)*m_size+m];
x[n+22]=(float) t1[(i+3)*m_size+m+1];
x[n+23]=(float) t1[(i+3)*m_size+m+2];
x[n+24]=(float) t1[(i+3)*m_size+m+3];
x[n+25]=(float) t1[(i+3)*m_size+m+4];
x[n+26]=(float) t1[(i+3)*m_size+m+5];
x[n+27]=(float) t1[(i+3)*m_size+m+6];
x[n+28]=(float) t1[(i+4)*m_size+m];
x[n+29]=(float) t1[(i+4)*m_size+m+1];
x[n+30]=(float) t1[(i+4)*m_size+m+2];
x[n+31]=(float) t1[(i+4)*m_size+m+3];
x[n+32]=(float) t1[(i+4)*m_size+m+4];
x[n+33]=(float) t1[(i+4)*m_size+m+5];
x[n+34]=(float) t1[(i+4)*m_size+m+6];
x[n+35]=(float) t1[(i+5)*m_size+m];
x[n+36]=(float) t1[(i+5)*m_size+m+1];
x[n+37]=(float) t1[(i+5)*m_size+m+2];
x[n+38]=(float) t1[(i+5)*m_size+m+3];
x[n+39]=(float) t1[(i+5)*m_size+m+4];
x[n+40]=(float) t1[(i+5)*m_size+m+5];
x[n+41]=(float) t1[(i+5)*m_size+m+6];
x[n+42]=(float) t1[(i+6)*m_size+m];
x[n+43]=(float) t1[(i+6)*m_size+m+1];
x[n+44]=(float) t1[(i+6)*m_size+m+2];
x[n+45]=(float) t1[(i+6)*m_size+m+3];
x[n+46]=(float) t1[(i+6)*m_size+m+4];
x[n+47]=(float) t1[(i+6)*m_size+m+5];
x[n+48]=(float) t1[(i+6)*m_size+m+6];
```

```

    }
    norm_x_dat();
    pca();

    for (i=0;i<t_size;i++)
        for (m=0;m<t_size;m++) {
            n=i*t_size+m;
            forcom(n);
            p=(i+3)*m_size+m+3;
            if (yo[2] > 0.8) yo[2]=1.0;
            if (yo[1] > 0.8) yo[1]=1.0;
            if (yo[0] > 0.8) yo[0]=1.0;
            if (yo[2] < 0.2) yo[2]=0.0;
            if (yo[1] < 0.2) yo[1]=0.0;
            if (yo[0] < 0.2) yo[0]=0.0;
            if ((yo[2] < 0.8) && (yo[2] > 0.2))
                yo[2]=(yo[2]-0.2)/0.6;
            if ((yo[1] < 0.8) && (yo[1] > 0.2))
                yo[1]=(yo[1]-0.2)/0.6;
            if ((yo[0] < 0.8) && (yo[0] > 0.2))
                yo[0]=(yo[0]-0.2)/0.6;

            /* calibration for scatter corrected image */
            pst=4379.7*pow(yo[2],4.0)-3392.7*pow(yo[2],3.0)-123.8*pow(yo[2],2.0)+1105.6*yo[2]+1.4;
            if (pst < 0.0) pst=0.0;

            image[p]=pst*0.01;

        }

    printf(" plane: %d\n",ii);

    /* initialize the scan matrix elements to zero */
    for (i=0;i<(num_views*num_projs);i++)
        scan[i]=0.0;

    /* forward project image data to form sinogram and store in scan matrix */
    fproj( image,image_size,scan,num_views,num_projs);

    for (i=0;i<(num_views*num_projs);i++)
        att_buf[i]=(short) scan[i];

    fwrite(att_buf,sizeof(short),num_views*num_projs,fout);

}

free(t1);
free(t2);
free(t3);

```

```

    free(image);
    free(scan);
    free(att_buf);
    fclose(fout);
    fclose(fp1);

} /* end of computation of results */
/*****/
/* reserves memory space for variables */
void res_space()
{
    w1=(double *) calloc(input_node*hidden_node1,sizeof(double));
    w2=(double *) calloc(hidden_node1*hidden_node2,sizeof(double));
    w3=(double *) calloc(output_node*hidden_node2,sizeof(double));
    th1=(double *) calloc(hidden_node1,sizeof(double));
    th2=(double *) calloc(hidden_node2,sizeof(double));
    th3=(double *) calloc(output_node,sizeof(double));
    yi=(double *) calloc(hidden_node1,sizeof(double));124124
    yh=(double *) calloc(hidden_node2,sizeof(double));
    yo=(double *) calloc(output_node,sizeof(double));
    x=(float *) calloc(num_dat*pcap,sizeof(float));
    w=(double *) calloc(pcap*pcam,sizeof(double));
    yy=(float *) calloc(num_dat*input_node,sizeof(float));
} /* end of res_space */
/*****/
void free_space()
{
    free(w1);
    free(w2);
    free(w3);
    free(th1);
    free(th2);
    free(th3);
    free(yi);
    free(yh);
    free(yo);
    free(x);
    free(w);
    free(yy);
} /* end of free_space */
/*****/

void main()
{
    res_space();
    open_weight();
    results();

```

```
free_space();
```

```
}
```

Program: atnem.c

```

/*****
/*
/* Purpose :      This program is used to apply the segmented attenuation map to      */
/*               emission projection data.                                          */
/*
/* To use :      atnem <emission filename>                                         */
/*
/* Author :      Ben Yu                                                            */
/*
/* Date :        Dec, 1995                                                         */
/*
*****/

#include <stdio.h>
#include <math.h>
#include <malloc.h>
#include "matrix.h"

#define MAX(a,b)      ((a) > (b) ? (a) : (b))
#define MIN(a,b)((a) < (b) ? (a) : (b))

void exit(), errtxt();

main(argc, argv)
int argc;
char *argv[];
{
/*      Start of MAIN Routine      */

FILE *fp, *fin, *effin;
int ij,k;
char inname[80], varname[10];
FILE *fp1, *fp2, *mat_create();
char *pname, sino_filename[40], *filename, str[80];
static short *sino_buf, *att_buf;
static double *temp_buf, max_sino, min_sino;
static float *profile, scaler;
static Main_header mhead;
static struct MatDir entry, matrix_list[60];
static Scan_subheader sc_head;
static int mat_num, mat_frame=1, mat_plane=1, mat_gate=1, mat_data=0, mat_bed=0,
num_mat=0, num_matrices=0;
static int data_type=1, nprojs, nviews, nplanes=31, nframes=1;
double temp;

```

```

/* Check number of input variables */
if(argc != 2){
    printf("\n");
    printf("\t\tTo use :\n");
    printf("\t\tatnem <emission filename> \n\n");
    errtxt("\n\tInsufficient Number of Arguments\n");
}
else{
    if ((argc--)>0) pname=*(argv++);
    if ((argc--)>0) strcpy(sino_filename,*(argv++));
}

/* Open sinogram file */

if (sino_filename == NULL)
    errtxt("\n\tInput Sinogram File NOT Found\n");
fp1=mat_open(sino_filename, "r");

/* Read main header block of sinogram file */

mat_read_main_header(fp1, &mhead);
num_matrices=mat_list(fp1, matrix_list, 60);
if(!num_matrices)
    errtxt("\n\tNo matrices found in Sinogram File\n");
i = strlen(sino_filename);
sino_filename[i-4] = '_';
sino_filename[i-3] = 'a';
sino_filename[i-2] = 't';
sino_filename[i-1] = 'n';
sino_filename[i] = '.';
sino_filename[i+1] = 's';
sino_filename[i+2] = 'c';
sino_filename[i+3] = 'n';
sino_filename[i+4] = '\0';
fp2=mat_create(sino_filename, &mhead);

printf("\n\t attenuation filename : ");
filename = gets(str);
if ((fin=fopen(filename,"rb")) == NULL) {
    printf("attenuation file open error.. exiting\n");
    exit();
}

nplanes = mhead.num_planes;
nframes = mhead.num_frames;

```

```

sino_buf=(short*)calloc(160*192*sizeof(short),1);
temp_buf=(double*)calloc(160*192*sizeof(double),1);
att_buf=(short*)calloc(160*192*sizeof(short),1);

/* Applying attenuation correction to emission projection data */

printf("Correcting: %d frames, %d planes\n",nframes,nplanes);
for (mat_frame = 1; mat_frame <= nframes; mat_frame++) {
    for (mat_plane = 1; mat_plane <= nplanes; mat_plane++) {
        printf("\n frame : %d plane: %d ",mat_frame, mat_plane);

/* Get matrix number */

        mat_num=mat_numcod(mat_frame, mat_plane, mat_gate, mat_data, mat_bed);

/* Locate, read emission sinogram file header information */

        mat_lookup(fp1, mat_num, &entry);
        mat_read_scan_subheader(fp1, entry.strtblk, &sc_head);

/* Read emission sinogram data */

        fread(att_buf,sizeof(short),192*160,fin);
        read_matrix_data(fp1, entry.strtblk+1, entry.endblk-entry.strtblk, sino_buf, data_type);
        max_sino=0.0;
        min_sino=0.0;
        temp=0.011*0.3911650;

/* Attenuation correction */

        for (i=0; i<192; i++)
            for (j=0; j<160;j++) {
                k=i*160+j;
                temp_buf[k]=((double) sino_buf[k])*exp(((double) att_buf[k])*temp);
                if (temp_buf[k] > max_sino)
                    max_sino=temp_buf[k];
                if (temp_buf[k] < min_sino)
                    min_sino=temp_buf[k];
            }
        for (i=0; i<192; i++)
            for (j=0; j<160;j++) {
                k=i*160+j;
                temp_buf[k]= temp_buf[k]*30000.0/max_sino;
                sino_buf[k]=(short) temp_buf[k];
            }
        sc_head.scan_max = 30000;
        sc_head.scan_min = (int) (min_sino*30000.0/max_sino);
        sc_head.scale_factor *=(float)(max_sino/30000.0);

```

```

        swab(sino_buf,sino_buf,192*160*sizeof(short));
        mat_write_scan(fp2, mat_num, &sc_head, sino_buf, 192*160*sizeof(short));
    }
}

/* Deallocate memory */

free(sino_buf);
free(att_buf);
free(temp_buf);

/* Close open files */

mat_close(fp1);
mat_close(fp2);
fclose(fin);

}          /* End of MAIN Routine      */

read_matrix_data(fptr, strtblk, nblks, dptr, dtype)
FILE *fptr;
int strtblk, nblks, dtype;
char *dptr;
{
    int i;
    float get_vax_float();

    mat_rblk( fptr, strtblk, dptr, nblks);
    switch( dtype){
        case 1:      /* byte format...no translation necessary */
            break;
        case 2:      /* Vax I*2 */
            swab( dptr, dptr, MatBLKSIZE*nblks);
            break;
        case 3:      /* Vax I*4 */
            swab( dptr, dptr, MatBLKSIZE*nblks);
            swaw( dptr, dptr, (MatBLKSIZE/2)*nblks);
            break;
        case 4:      /* Vax R*4 */
            swab( dptr, dptr, MatBLKSIZE*nblks);
            for (i=0; i<nblks*(MatBLKSIZE/4); i++)
                ((float *)dptr)[i] = get_vax_float(dptr, 2*i);
            break;
        case 5:      /* IEEE R*4 */
            break;
        case 6:      /* 68K I*2 */
            break;
        case 7:      /* 68K I*4 */

```

```

        break;
    default: /* something else...treat as Vax I*2 */
        swab( dptr, dptr, MatBLKSIZE*nblks);
        break;
    }
    return;
}

void errtxt(error_text)
char error_text[];
{
    fprintf(stderr, "... Run time error ...\n");
    fprintf(stderr, "%s %s\n", " ", error_text);
    fprintf(stderr, "... Exiting to system ...\n");
    exit(1);
}

```

Interconnection weights stored in the file 'w.dat'.

```

0.737089 0.006127 0.054414 0.206543 0.542084 -0.682136 0.028294 -0.397931 -0.100141 -0.418678 -
0.632094 -0.210317 -0.303509 -0.186443 0.431323 -0.634822 -0.034957 -0.055506 0.104270 0.159065 -
0.417327 -0.648419 -0.107386 -0.344787 -0.256011 0.642872 0.107626 -0.026827 0.138214 0.279533
0.368413 0.355163 0.373454 0.184462 0.262692 -0.401862 -0.323421 -0.296588 -0.409669 0.225863
0.509305 0.215770 0.635444 -0.229733 -0.191314 0.478761 0.236452 -0.085692 0.266120 0.240855
0.702336 -0.644237 -0.283617 0.050044 -0.449288 -0.054564 -0.202054 0.184923 -0.064937 -0.522610 -
1.277935 1.177994 0.647235 0.192651 1.031200 -0.470381 -0.421148 0.282077 -0.402043 -0.056503 -
4.109977 4.536390 1.626521 1.915290 3.512060 1.847498 0.089686 0.656363 -0.830901 5.864946 -
0.468976 0.443808 0.451945 0.287340 0.428720 -0.513613 -0.388530 0.357695 -0.387793 -0.248260 -
0.009659 0.235242 0.071110 -0.561877 0.144893 0.417794 0.586094 -0.486278 0.416380 0.628154 -
0.560208 0.051703 0.114189 1.170410 0.692880 -0.438900 -0.760014 0.485639 -0.510490 -0.644990 -
1.318437 -13.473027 -0.391586 -0.252132 0.763198 0.423702 0.255517 3.083719 -0.815220 -1.688581 -
1.075780 0.470441 -2.730096 0.179011 1.565304 0.682813 -0.624747 -1.012129 0.824834 0.711201 -
3.123938 4.240994 0.484306

```

Interconnection weights stored in the file 'pcaw.dat'

0.139854 0.147908 0.146137 0.143020 0.150669 0.146654 0.141845 0.145994 0.142431 0.151092
0.152131 0.145173 0.145893 0.141755 0.150398 0.143320 0.149270 0.147161 0.148986 0.147719
0.146310 0.146958 0.144578 0.147157 0.146930 0.151780 0.142217 0.141610 0.140544 0.146392
0.150798 0.150064 0.149567 0.144317 0.143928 0.137783 0.140556 0.142694 0.146465 0.146712
0.140580 0.137680 0.142986 0.142947 0.142631 0.146779 0.142085 0.138097 0.140241 0.058534
0.063725 0.064643 0.058750 0.059758 0.058697 0.053785 0.063378 0.064625 0.059728 0.065145
0.056841 0.063062 0.054538 0.062151 0.057155 0.061603 0.056818 0.061660 0.055718 0.055636
0.061768 0.057070 0.059355 0.059132 0.065663 0.062279 0.054316 0.057409 0.063072 0.057801
0.061681 0.060997 0.058088 0.058974 0.056255 0.057561 0.062422 0.064351 0.057748 0.055924
0.056147 0.055170 0.060758 0.058212 0.060090 0.062568 0.058026 0.052570 0.035217 0.038898
0.040058 0.037642 0.040190 0.039356 0.035855 0.038303 0.040711 0.038150 0.040256 0.039442
0.034170 0.036082 0.038814 0.043736 0.039508 0.036000 0.039465 0.040817 0.040308 0.042272
0.035797 0.035768 0.042226 0.035200 0.038924 0.042323 0.035075 0.035251 0.039147 0.035080
0.039853 0.041830 0.032607 0.038082 0.037338 0.042001 0.035564 0.043037 0.032916 0.037547
0.034662 0.033235 0.031975 0.032460 0.040014 0.033203 0.033487 0.030690 0.029848 0.028857
0.025701 0.028465 0.031901 0.032160 0.025017 0.029684 0.026870 0.028170 0.030817 0.030789
0.027510 0.028662 0.028859 0.029862 0.027116 0.027189 0.028838 0.025073 0.025495 0.025315
0.027821 0.027549 0.033155 0.029989 0.033556 0.033475 0.032536 0.027760 0.028489 0.028370
0.025844 0.026769 0.024334 0.024419 0.031399 0.027139 0.031348 0.025277 0.027588 0.029573
0.029712 0.030522 0.031829 0.025610 0.024077 0.029292 0.017145 0.018502 0.019783 0.023026
0.021146 0.020445 0.014899 0.017530 0.022131 0.023018 0.020538 0.022020 0.015269 0.016472
0.014874 0.015588 0.019012 0.016630 0.023615 0.015708 0.016661 0.019509 0.016708 0.019224
0.022360 0.017852 0.020214 0.018124 0.015506 0.021144 0.023679 0.023911 0.024600 0.021423
0.022825 0.016787 0.021480 0.019228 0.022195 0.019643 0.021793 0.014836 0.022469 0.019758
0.024077 0.017430 0.016931 0.014477 0.014362 0.020895 0.021177 0.024520 0.024721 0.017212
0.016432 0.022895 0.017039 0.023763 0.018333 0.020561 0.017707 0.024756 0.015926 0.022692
0.021359 0.022332 0.023939 0.020972 0.025384 0.019371 0.016428 0.018517 0.022337 0.022954
0.024909 0.023487 0.021645 0.020277 0.024732 0.021904 0.018224 0.018010 0.020980 0.021018
0.016028 0.018077 0.017424 0.025011 0.017896 0.021338 0.018141 0.021808 0.020897 0.024252
0.022399 0.023810 0.016593 0.022573 0.014246 0.021674 0.015687 0.019909 0.020422 0.017927
0.019349 0.021808 0.022019 0.021934 0.021780 0.020627 0.019698 0.018316 0.021253 0.016352
0.018604 0.022010 0.020576 0.021304 0.019822 0.022109 0.018627 0.023139 0.023613 0.016746
0.021164 0.013740 0.015929 0.022750 0.021352 0.018951 0.013700 0.019782 0.017478 0.019148
0.012255 0.020476 0.017839 0.018317 0.021575 0.013794 0.018114 0.011367 0.015494 0.022090
0.014150 0.011670 0.012725